Organic field effect transistor fabrication by a novel patterning technique and the study of organic semiconductor crystallization

Shuo Zhao

Doctor of Philosophy

University of York

Electronics

August 2016

Abstract

This thesis is concerned with micro/nano fabrication of polymer materials for organic thin film transistor (OTFT) application and crystallization of solution-processable small molecule and conjugated polymer thin film. A method has been developed to form self-assembled arrays of nano/micro wires by controlling solvent evaporation of a solution film that is trapped in between a substrate and a structured template. Various solution-processable materials were successfully patterned by the developed method, with particular focus on conjugated polymers materials, such as p-type & n-type semiconductor polymers, and conductive polymers. The potential applications of such fine patterned materials were demonstrated on both field effect transistors (FET) and electrochemical transistors (ECT). The polymer FET measurement results demonstrated that the device range of on/off ratio was from 10^3 to 10^5 and the range of charge carrier mobility was from 10^{-4} $\mathrm{cm^2/Vs}$ to 10^{-2} $\mathrm{cm^2/Vs}$. For the electrochemical transistor, the device can work under a small applied gate and drain bias (less than 0.5 volts). Pattern formation with complicated geometries, pattern transfer processes, and pattern formation dynamics have been investigated. Further, the recrystallization mechanism of amorphous small molecule thin film spin-coated on different substrate was investigated. It was found that a small molecule film crystallized from different substrates can have different preferential orientations caused by a different scenario of materials-substrate interaction, and this can dramatically influence the conductivity of the crystalline film. The dynamics of recrystallization was studied in detail through examination of both growth and nucleation of crystals from their amorphous matrix. The results showed that both the activation energy the small molecule obtained and the crystal growth preferential orientation on different substrates were different during the crystallization process. The study of both the temperature and annealing time influences on the conjugated polymer crystalline film property were also studied experimentally.

Table of contents

List of figures

Chapter 1

Chapter 2

Chapter 3

Chapter 4

Chapter 5

Chapter 6

List of tables

List of publications

- S.P. Li, Y.T. Chun, **S. Zhao**, Y.B. Xu, D.P. Chu, high-resolution patterning of solution-processable materials via externally engineering pinning of capillary bridges, *Nature Nanotechnology* (submitted)

- S.P. Li, **S. Zhao**, D.P. Chu, Crystallization of solution processable amorphous tetrabenzoporphyrin films, *Thin Solid Films* 590 (2015):49-53

Acknowledgement

This thesis concentrates on my four years' research work in the University of York. I very appreciate that Prof. Yongbing Xu offered me an opportunity of Ph.D. study in his group. Without his support and continued encouragement, my research work could not have been finished smoothly.

I would also like to thank Prof. Daping Chu for offering me the opportunity to let me access his laboratory located in the University of Cambridge. I am also most grateful to Dr. Shunpu Li, for his support throughout my entire Ph.D. study, not only on my research work but also in my life in general. Under his guidance, all difficulties that I encountered in my experiments were solved. My practical experience was also sharpened because of his guidance. It is my honor having the opportunity to cooperate with him to finish my project.

Next I must pay gratitude to the technician group members, Dr. Iain Will, Mr. Jonathan Creamer and Mr. Charan Panesar are their support and instruction about operating the equipment operation in the cleanroom.

I would like to thank my colleagues and all of my friends in York. They are Dr. Xuefeng Hu, Dr. Cong Lu, Dr. Wenqing Liu, Dr. An Ding, Dr. Ming Zhao, Ms. JiaZhuo Cheng, Mr. XianYang Lu, Mr. Yu Yan and Mr. LingYu Yan. We experienced so many things on the road of pursuing the Ph.D. degree; happy and unhappy times were mixed together, which will be the best memories in my life. Some of you have already succeeded, some of you are still on the way. I make the best wishes for all of you: Good luck, my friends!!

The last, but the deepest, gratitude belongs to my dear parents and my girlfriend Miss Bingying Yu. The four years Ph.D. study were done under your love, patience, tolerance and understanding. This support I received from them cannot be described in words; no matter how much I say, I cannot express my gratitude.

Declaration

I declare that this thesis is a presentation of original work and I am the sole author. This work has not previously been presented for an award at this, or any other, University. All sources are acknowledged as References.

Chapter 1

Introduction

1.1 History of transistor

1.1.1 Point-contact and bipolar junction transistors

At the beginning of the 20th century, most of the world's best scientists were focused on the development of radar, with few paying any attention to semiconductor materials. During that time, semiconductor materials were not in a good place because of the limitations of techniques connected to their purification. It was very difficult to acquire material of both high purity and quality; often, the same material fabricated under the same procedure would produce totally different performances. Since all manner of impurities are mixed together within semiconductors, properties of the materials were decided by the variety and quantity of their contamination rather than their own behaviour. This was the general situation until February 1939, when an electrochemist, Russell Ohl [1], accidentally found a p-n junction in an experiment, a phenomenon he clarified through additional research. In the years that followed, Ohl found that super-purified germanium might be the focal point for semiconductor devices. In 1942, physicist Seymour Benzer [2] found a single crystal of germanium gives an excellent performance on a rectifier compared to other semiconductor materials. It was those discoveries which made semiconductor devices possible.

After the Second World War ended in 1945, a solid-state research group was set up in Bell Laboratories in the United States. The first mission of this group was to develop a new electronic device which could alter a vacuum triode. The triode was widely used in telecommunications at that time because not only could the human voice which be moderately amplified through it, but the transmission distance was unlimited. However, its drawbacks, including big energy consumption and thermal production, meant that it was unrealizable. One of the leaders of this group, physicist William Shockley, asked researchers to focus on germanium whilst also proposing an idea for a new device, where the application of a strong field induces and controls the current flow on the surface of semiconductor. This idea looked like water flowing in a rubber hose, where people could control its pressure and modify the flow size. In December 1947, John Bardeen and his colleague Walter Brattain demonstrated the prototype of this device, the point-contact transistor [3] as shown in Figure 1.1 and Figure 1.2 below.

Figure 1.1. Photograph of the prototype of the point-contact transistor that was invented by Bardeen and Barttain in December 1947. A strip of gold foil, slit along one edge is pressed down into the surface of a germanium slab by a polystyrene wedge, forming two closely spaced contacts to this surface [3].

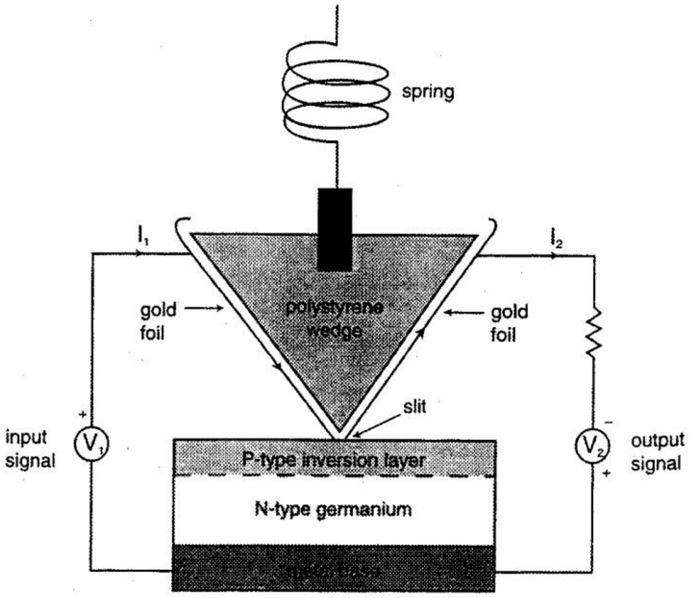

Figure 1.2. The schematic diagram of a point-contact transistor （acquired from Ref [3]）

They called this new device a “*transistor*”, the portmanteau of the terms “transfer” and “resistor”. The inventors explained it as follows: a transistor is a special resistor of an electrical signal, which is amplified when transferring through this device. From Figure 1.1 and Figure 1.2, it can clearly be seen that n-type germanium was deposited on a metal slab, and a layer of p-type was formed on it. A polystyrene wedge covered by gold foil with a narrow crack of about 50 μm was carefully slit along that edge, and using a spring to press it into the germanium surface, two closely space gold contacts fully touch the material at the contact point. Although this transistor prototype was clumsy and unstable, it was undoubtedly a magnificent breakthrough for semiconductor electronic devices.

As other people focused on trying to enhance the performance of germanium-based transistors, another idea started to foment in Shockley’s mind. He was thinking that if two types of semiconductor were put together, constituting a sandwich structure such as p-n-p or n-p-n, the semiconductor in the middle could yield a depletion layer because of a lack of electrons, while both of the sides would have sufficient electrons. By modulating the middle layer, the number of electrons in the device could be controlled.

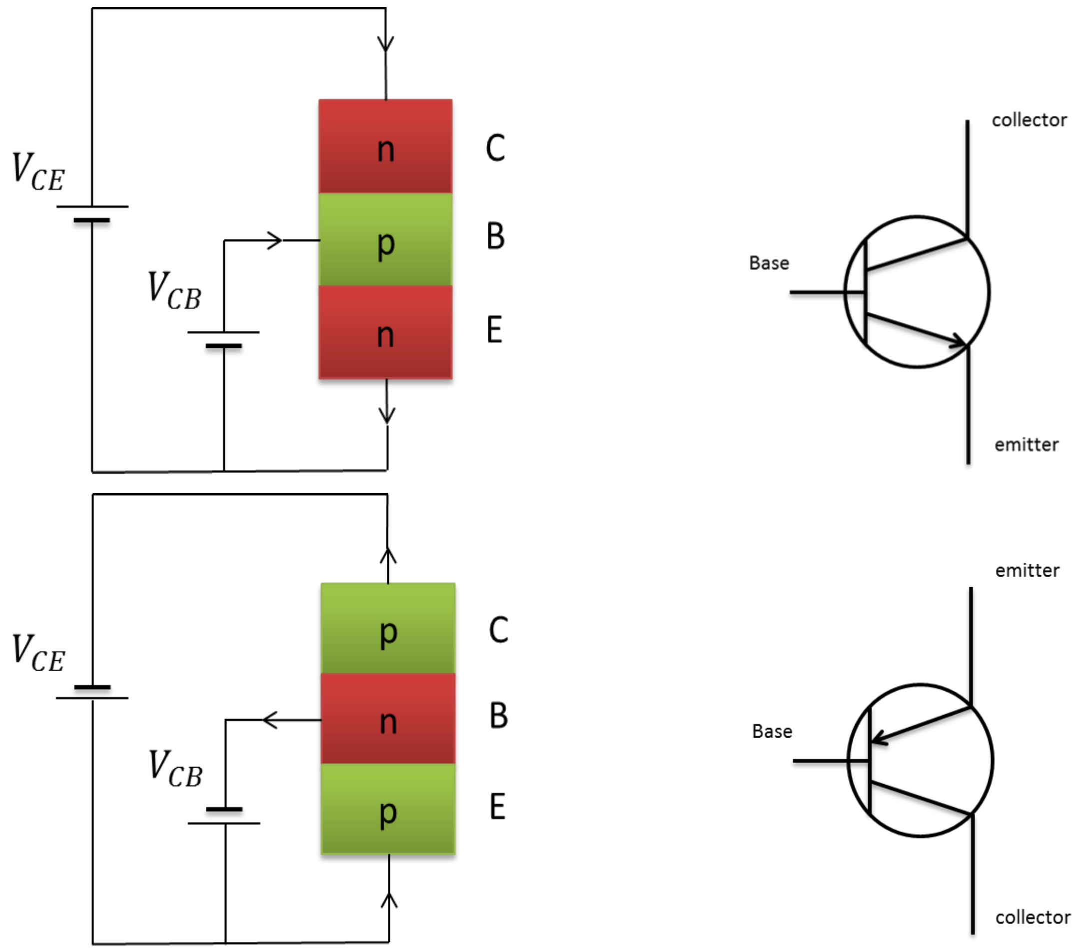

Figure 1.3. The two types of p-n junction transistors.

The difference to the point-contact transistor was that in this device the current flowed through the inside of the semiconductor, not on the surface. On the 18th February 1948, under Shockley's guidance, his group physicist John Shive performed an experiment. Following his report, Shockley realized that his hypothesis was correct. At the same time, throughout this experiment John Shive noticed that the middle layer of semiconductor must have high purity and be thin enough. Gordon Teal, the best crystal expert at Bell Labs, tried to convince Shockley to use single crystal instead of polycrystalline materials to fabricate the device, since this would avoid current being diffracted by grain boundaries. This suggestion was rejected.

It was therefore lucky that Teal's advice reached Jack Morton, also an engineer at Bell Labs, who at the time was leading a group trying to make point-contact transistors a commercial reality. He accepted Gordon suggestion. In April 1950, he successfully fabricated this junction type transistor using signal crystal germanium with his colleague Morgan Sparks [4]. In addition, they were able to prove it had a signal amplification function. Based on the contribution of these pioneers, Sparks improved the performance of this junction transistor by reducing the thickness of the middle layer of the semiconductor. The bipolar transistor compared favourably to the point-contact transistor.

Up until this point, every idea and device had been based on germanium despite the fact that a key problem was that germanium-based transistors could not work for many consecutive hours and there were still thermal issues. People generally thought that silicon-based transistor implementation was still a long way away. Indeed, it was 1954 before Teal demonstrated three silicon-based transistor prototypes at a wireless engineering conference. Following this, nearly all semiconductor companies and laboratories realized that replacing germanium with silicon was feasible, and therefore began to focus on silicon. As this area of research flourished and developed, scientists and engineers began to consider the miniaturization of the size of the transistor, since the transistor had to be connected to other electronic elements by wires. Four years later, Jack Kilby, a junior engineer working for California Instruments, suddenly had an idea: the reason we have to connect all kinds of electronic devices together by wires to achieve functionality is that they were fabricated using different materials – only the transistor was made of silicon. He thought that were all the raw materials to be made of silicon, more transistors could be produced on a silicon wafer. In this way, the concept of the integrated circuit (IC) was born.

1.1.2 Field effect transistor and metal-oxide transistor

In 1959, the Bell Laboratory scientist Martin Atlla, an Egyptian, found that a fine and uniform film of silicon dioxide (SiO_2) could be formed through thermal oxidation in a vacuum system [5]. Shockley had put forward the field effect concept back in 1945, but this idea had never been realized. Bipolar transistor use was widespread in electronic devices at that time, but the idea of the bipolar transistor originated from triodes. The conceptual difference between a bipolar transistor and a field effect transistor is that the former depends on transmission through minority charge carriers, while the latter relies on majority charge carriers. A year later, Atlla and his colleague, the Korean scientist Dawon Kahng, invented a real field effect transistor on Si/SiO_2, known as an insulated-gate field-effect transistor (FET). [6]. Quickly, major semiconductor product manufactures transferred their attention to this new device. Based on this, the Paul K. Weimer research group in the Radio Corporation of America set up a concept of thin film transistor (TFT) in 1961 [7]. They discovered that transistors could be fabricated through an evaporated semiconductor on the insulator layer. This method provided the means by which thousands of transistors could be connected in an efficient way which was also able to realize different electronic functions on a silicon wafer the size of a stamp. In 1962, two young engineers - Steven R. Hofstein and Frederic P. Heiman - found that a conduction band, high resistance channel and oxide insulating layer could be built up through thermal diffusion and oxidation methods on a silicon wafer. Thus, a breakthrough electronic device came into being: a metal-oxide-semiconductor field effect transistor (MOSFET). Its structure schematic is presented in the Figure 1.4 below.

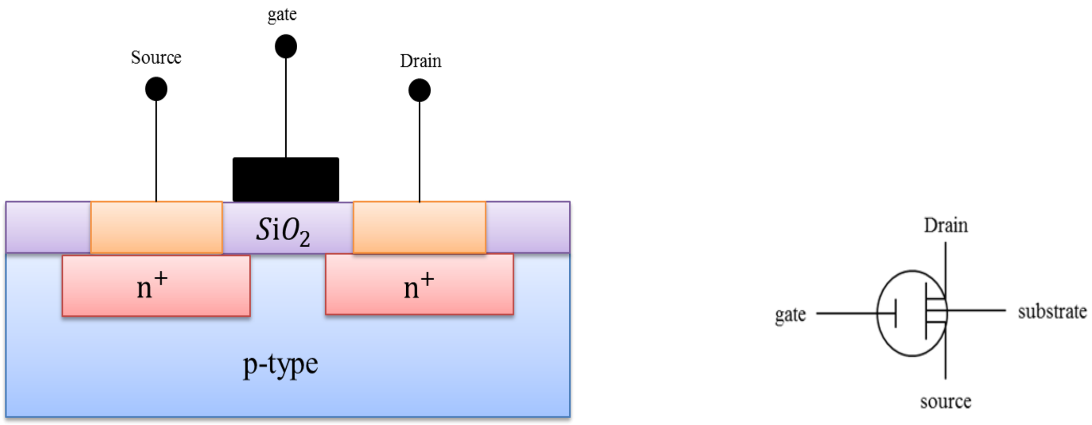

Figure 1.4. The structure of metal-oxide-semiconductor field effect transistor (MOSFET)

This schematic demonstrates a n-type MOS transistor. When a positive voltage between source and drain has been applied, electrons in this channel will be attracted to the surface between the silicon and insulator, while a positive charge will be repulsed in the opposite direction. When these charge carriers are sufficient, the current produced will flow from source to drain. The gate controls the intensity of the current. There is also a P-type MOS transistors, but because of the speed of the hole transmission is quite slow compared with the electron, this kind of transistor is rarely used. There is no doubt that the success of the bipolar junction transistor and the MOS transistor was a huge breakthrough in the electronics industry. Many well-known semiconductor and computer chip manufacture companies have emerged out of the discovery of these transistors, including Shockley Semiconductor Laboratory, Fairchild Semiconductor, California Instrument, IBM, Intel and AMD. They are now, all, large and important industries across the world. Even today, Intel is still pursuing transistor miniaturization in order to integrate as many transistors on a chip as possible in order to enhance the speed of operation.

1.2 Moore's law and challenge

After the MOS transistor was commercialized, the integrated circuit began to develop rapidly. In 1965, about 50 transistors were integrated on each chip. In the same year, Gordon Moore, a cofounder of Intel and Farichild Semiconductor, predicted that the invention of integrated circuits would result in the density of components in the circuit increasing exponentially - or more exactly, they would double - every year. Indeed, minimum component costs have increased at a rate of roughly a factor of two per year [8]. While, the first commercial microprocesser was realized after six years by the Intel corporation. Using 2300 transistor on single wafer, the number of transistors are 46 times compared with in 1965. It can be calculated that the number of transistors has indeed nearly doubled every year. In 1975, Moore modified his prediction, saying that a period of one year was not accurate, and that is should be two. According though to accurate statistics, it seems that a period of 18 months is about right, as seen in the Figure 1.5 below.

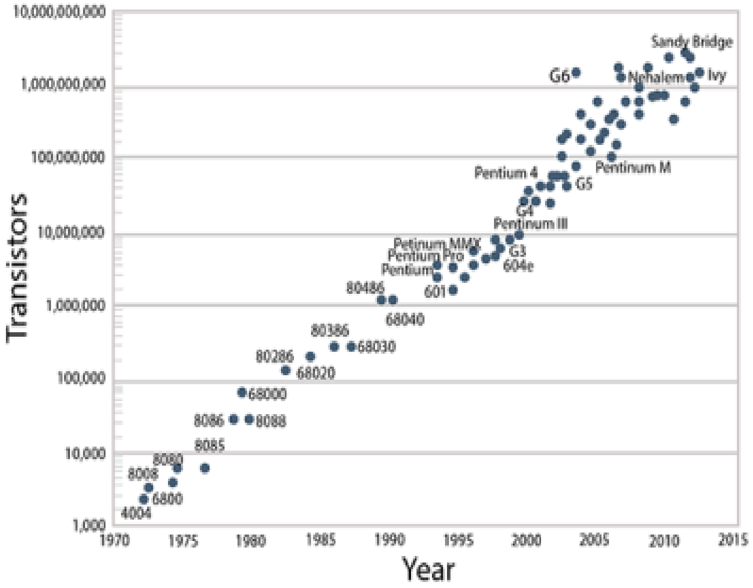

Figure1.5. The number of transistors on silicon chip from (1970 to 2015) (acquired from http://www.overclock.net/t/1542835/pc-world-intel-moores-law-will-continue-through-7nm-chips/30)

Intel's commercial large-scale industrial production technique has seen them reach 14 nm (in 2015). As transistor miniaturization on silicon wafer, if the transistor gate length reaches 5 nanometer scale, an electron would be able to tunnel from source to drain, meaning that the gate was redundant. In 1999 some scientists speculated that Moore's Law would face greater challenges in the future [9]. The discovery of carbon-tubes seemingly provided a new direction. This new material was discovered by the Japanese scientist Iijima Sumio in 1991 [10]. Its properties and nano scale size attracted researchers who tried to build up a transistor by using this material. After seven years, the Dutch scientist Cees Dekker created the first nano transistor on a single carbon-tube, although the result was unsatisfactory. Meanwhile, other scientists and research groups began to consider a single-atom transistor [11] and a graphene transistor[12]. Transistor research is continuing, and perhaps one day Moore's Law will no longer be applicable in electronics, or people will find a way of making transistors more effective.

1.3 Aim of the PhD work

Recently in electronics industry development, the orgaince field effect transistor (OTFT) has attracted great interest due to its potential capability for integration into products ranging from non-volatile memory, radio frequency indetification tag (RFID) to switching devices for active matrix display. As a fundamental component, its performance to a certain extent determines the device quality. Among all the organic semiconductor based electronics devices, taking the organic ferroelectric field effect transistor (FTFT) for an example, it has drawn great attention because it has non-destructive read-out property and is capable of integration with other organic device to build a circuit, etc. Although it has so many advantages, there still are some drawbacks that hinder it in real applications, such as high fabrication cost and high power consumption that occurs during the read operation when the channel of the transistor is in the ‘on’ state. Thus, the most important work in my PhD study is looking for a method to achieve a material, for both p- and n-type, “all self-alignment process” without mask alignment, thereby reducing the cost in the fabrication process and at the same time obtaining large-area high resolution with well-ordered material structure. Finally, the successful fabricating of both p- and n-type organic field effect transistor and combining them to make up an organic complementary circuit (CMOS) if possible.

Another important goal is to study the texture influences on small molecule organic semiconductor material crystal orentation. The crystalline film growth on the both chemical treatment and bare substrate illustrate the different structures that have been observed and captured by optical micorscope.

Last, but not the least, in my PhD work, is the experimental study of polymer materials crystallization process on identical substrates with variable anealing time under fixed temperature. As we know, the quality of polymer crystalline film is a very important factor that can affect performance of devices in real applications. Therefore, making sure we understand the material properties and finding an appropriate annealing temperature and time are quite useful in device fabrication, even for material performance enhancement. The spectrum absorption equipment has been implemented in this study by another student at Nanjing University to reveal the relationship between temperature and polymer film crystallization degree.

1.4 Overview of the Thesis

Chapter 2 reviews several aspects of organic semiconductor materials from its conductivity mechanism, material type, to the realm of industrial applications. This chapter also contains a kind of natural phenomenon, which had been analyzed by researchers, and can be utilized in device fabrication. In Chapter 3, all of the essential faclities for fabrication and the measurement instruments have been described. The details of traditional manipulation techniques in manufacturing such as optical lithergraphy, thermal evaporation are included. From the Chapter 4, the topic has been moved to the specifics about studying the patterning soluble organic semiconductor materials technique on well cleaned substrates. It contains all the infromation of materials that have been utilized in the following series of experiments, such as material chemical structure and properties; Moreover, several patterning techniques with related results have also been demonstrated in this chapter. In Chapter 5, following the results from Chapter 4, the organic field effect transistor (OFET) and electro-chemical transistor (OECT) fabrication by various methods, including patterning transfer and lift-off processing, have been described in detail. At the same time, the device performance measurement and quality evaluation have been given as well. Chapter 6 is the last chapter of the experimental part which contains the study of substrate surface texture influences on small molecule organic semiconductor material crystal orentation. The crystalline film growth on the both chemical treatment and bare substrate illustrate the different structures that have been observed and captured by optical micorscope. Another experimental part in this chapter is about the polymer material crystallization degree with different annealing time under a fixed temperature. The spectrum absorption measurement has been carried out to evaluate the properties of the material. Chapter 7, the last one in this thesis, is the summary and conclusions of the whole work in my PhD study with an outline of the work that needs to be done in future.

Reference

1 Riordan, M. & Hoddeson, L. The origins of the pn junction. *IEEE spectrum* **34**, 46-51, (1997).

2 Greenspan, R. J. Seymour Benzer (1921–2007). *Current Biology* **18**, R106-R110, (2008).

3 Riordan, M., Hoddeson, L. & Herring, C. The invention of the transistor. *Reviews of Modern Physics* **71**, S336, (1999).

4 Sparks, M. (Google Patents, 1953).

5 Atalla, M. M., Tannenbaum, E. & Scheibner, E. Stabilization of silicon surfaces by thermally grown oxides. *Bell System Technical Journal* **38**, 749-783, (1959).

6 Kahng, D. A historical perspective on the development of MOS transistors and related devices. *IEEE Transactions on Electron Devices* **23**, 655-657, (1976).

7 Weimer, P. K. The TFT a new thin-film transistor. *Proceedings of the IRE* **50**, 1462-1469, (1962).

8 Schaller, R. R. Moore's law: past, present and future. *IEEE spectrum* **34**, 52-59, (1997).

9 Packan, P. A. Pushing the limits. *Science* **285**, 2079-2081, (1999).

10 Iijima, S. Helical microtubules of graphitic carbon. *nature* **354**, 56-58, (1991).

11 Fuechsle, M. *et al.* A single-atom transistor. *Nature Nanotechnology* **7**, 242-246, (2012).

12 Das, A. *et al.* Monitoring dopants by Raman scattering in an electrochemically top-gated graphene transistor. *Nature nanotechnology* **3**, 210-215, (2008).

Chapter 2

Literature Review

2.1 Introduction

The Nobel Prize in Chemistry for 2000 was awarded jointly to Alan J. Heeger, Alan G. MacDiarmid and Hideki Shirakawa for “the discovery and development of conductive polymers”. In 1977, this group found that the electrical conductivity of polyacetylene dramatically increased, systematically and continually, by about eleven orders of magnitude when doped with iodine vapour, its conductivity reaching $10^5\ \mathrm{S/m}$[1]. This ground-breaking discovery resulted in the overthrow of the traditional view that only ordinary polymer materials could be insulators. At the same time, the dominant position of silicon in the manufacture of electronic devices was affected as well, raising the possibility of raw material replacement in the semiconductor industry. In the decades that followed, a considerable number of scientists and academic institutions across the world focussed on organic material development. Compared with the traditional inorganic SC materials, organic polymer SC materials have many advantages, such as being light and low-cost, and that they can be processed at room temperature. They are also soluble and have an easy deposition on the substrate, making them competitive with silicon and gallium arsenide in certain respects. Organic materials have been widely used in electronic devices, such as organic light-emitting diodes (OLED) [2] sensors and organic field effect transistors (OFET) [3]. OFETs are one of the most attractive areas for research, and they are an area where there is a huge amount of research taking place.

2.2 Organic Materials Conductivity Mechanism

As is commonly known, materials can be classified into conductors, insulators, and semiconductors according to their conductive ability. Their material band structure can be made clear by the status of each band regarding occupation by electrons; energy bands which are fully occupied or unoccupied are non-conductive because the electrons cannot move freely if the energy band is fully occupied, and there are no electrons in an empty band. For conductors, some of the electrons are in the conductive band ($\mathrm{E_C}$), whereas for semiconductors and insulators, most electrons are in the valence band ($\mathrm{E_v}$). The difference between insulators and semiconductors is the band gap ($\mathrm{E_g}$). This gap in semiconductors is quite narrow, approximately 3eV, compared with insulators, where it is usually above 5eV. Therefore, under certain conditions, the electrons in their located valence band can become excited and move to the conductive band, making the material conductive.

The nature of bonding in organic semiconductors is fundamentally different to their inorganic counterpart. As mentioned before, polyacetylene was the first polymer which was reported as having a conductivity property in plastic material. In fact, all conductive polymers contain two main properties. The first is the presence of conjugated double bonds along the backbone of the polymer. In conjugation, the polymers are constructed of single and double bonds which alternate between carbon atoms. The classic representation of this alternating structure is shown in Figure 2.1 below. The second property is that the polymer must be “doped” through an oxidation agent in order to remove electrons, or through a reduction agent, so that extra electrons may be inserted into the material. Those holes and extra electrons can make the molecule produce electrical conductivity [4].

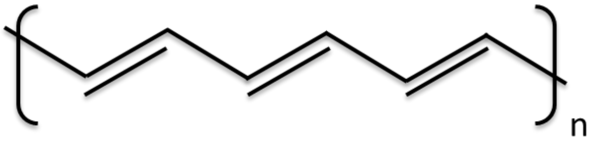

Figure2.1. The chemical structure of polyacetylene

In the single and double bond alternating structure, the single bond is known as a sigma (σ) bond, while the double bonds consist of a sigma (σ) bond and a pi (π) bond, which is formed when one of the electrons located on a 2s-orbital is excited into P_z-orbitals, leading to the occurrence of sp^2-hybridization in the carbon atom within the molecule. A σ-bond is the strongest type of covalent bond, requiring both atoms to contribute to an electron from the s-orbital. Taking H_2 as an example of this, which can be seen in Figure 2.2 below:

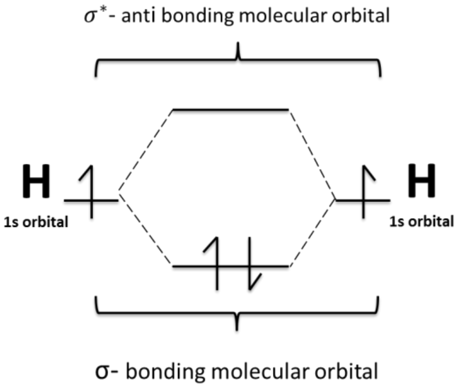

Figure 2.2. The theory of σ-bonding and σ^*-antibonding formation

The π-bonds directly share a pair of electrons between the $\mathrm{P_z}$-orbitals of the carbon atoms. Compared to the σ-bonds which form the backbone of the molecules, the π-bond is much weaker since their orbitals are further away from the positive nucleus.

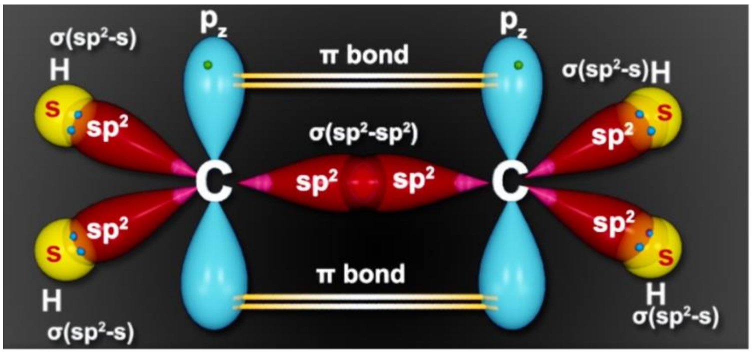

Figure 2.3. The sp^2 $hybridization$ (acquired from https://i.ytimg.com/vi/ES5T12WdRpU/maxresdefault.jpg)

Thus, electrons are localized when π-bonds are formed in the molecule. However, in conductive materials, the π-orbital can overlap with neighbouring double bonds due to conjugation. The result is that electrons can move to another bond or to another molecule. In so doing, the electron becomes "delocalized". Polymer and oligomer conduction is the result of the delocalization of these charge carriers along the polymer chain.

As the result, the repeating structure of alternate single and double bonds in a conjugated backbone causes bonding and anti-bonding states, and a forbidden energy gap forms between spatially delocalized electronic band structures. See Figure 2.4 below.

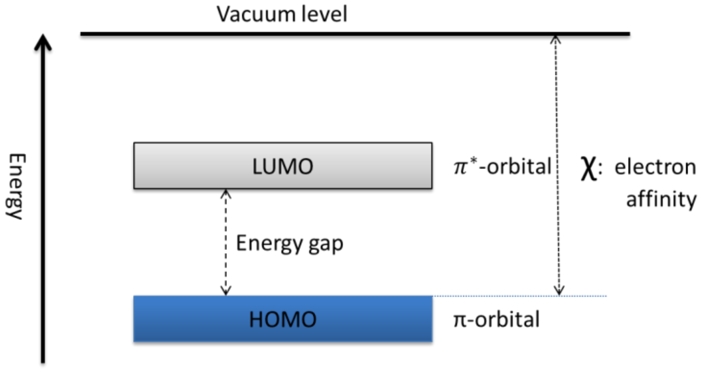

Figure 2.4. The schematic diagram of HOMO and LUMO structure

2.2.1 Energy level

The molecular energy level is a crucial and not negligible part in the polymer synthesis process. Proper orbital energy level adjustment can make a polymer material well matched with the metal electrodes work function, providing efficient charge carrier (holes or electrons) injection and transport. The highest occupied molecular orbital (HOMO) is composed of π-orbitals with filled electrons in a bonding state, similar to the valence band in inorganic semiconductors. Correspondingly, the lowest occupied molecular orbital (LUMO) is made up of π^*-orbitals with rare electrons in an anti-bonding state, equivalent to the conduction band in silicon. For p-type and n-type semiconductors, the usual HOMO level is around 5 eV and the LUMO level should be between 3 eV and 4 eV respectively. The difference between these two orbitals comprises the band gap (E_g). See Figure 2.4 above. The value of E_g can be manipulated by the number of repeat units in the chemical structure; generally speaking, it decreases with the number of repeat units in the chain [5]. As the number of the same unit increases, sometimes, the chemical stabilization may decrease (e.g. benzene). As noted above, the doping process in enhancing the conductivity of materials is very important. This essential procedure determines the semiconductor properties, either p- or n-type. Generally, an oxidative agent is chosen for polymer doping in order to create p-type materials. Electron affinity (or ionization potential) is another important parameter which decides the stabilization of material in ambient.

2.2.2 Charge transport in organic materials

As we known, the crystal lattice vibration can produce phonons. In a traditional semiconductor material, the electronic interaction is much stronger than electron-phonon interaction. Besides, the electron-phonon coupling is generally considered as a hindrance in the behaviour of electron transport in the inorganic semiconductor material. Different with this, in the organic semiconductor molecular crystal, the electron-phonon interactions are comparable to, or even larger than the electronic interaction. In such cases, electron-phonon coupling is no longer to be considered as a perturbation [6]. In contrast, the phonon provides energy to the electron, assisting it in transiting to an adjacent molecule. The electron-phonon coupling can form a kind of quasi-particle, called a polaron, in which the electronic charge is dressed with phonon clouds [6]. In the conducting polymer, the interaction between molecules is by the Van der Waals force. A charge carrier is easy to transport along conjugated chains because of π-orbital overlap, but it is relatively difficult to transport between molecules because firstly, substitution chains of the molecules are disordered in crystallization phase. These disordered segments often prevent charge transport. The second reason is the charge carrier mean free path is even shorter than the distance between two molecules. Therefore, charge carriers need to acquire an extra energy to overcome the limitation to arrive at the next molecule; This process is commonly described as “hopping”. The polaron transport in organic semiconductors is constituted of two distinct parts: inter- and intra-molecular vibrations, which corresponding to “nonlocal coupling” and “local coupling”, respectively. Both of them can affect the charge transport mechanism. A mathematical model, which combines these two parts, has been comprehensively described in the Holstein-Peierls system [7]. In this model, two parameters play an important role: transfer integral (*t*) and charge reorganization energy (λ). Among them, the “nonlocal coupling” depends on the value of the transfer integral. The electron-coupling constant (g) can be obtained from Holstein’s one-dimensional model. The value of this constant can result in different charge carrier mobility temperature dependent relationship which has been fully described in [6].

2.3 Organic Semiconductor and Insulator Materials

In general, organic semiconductors can be broadly classified into two categories: conjugated polymers and oligomers (small molecules). Both are now widely used in

OFET and related device fabrication. The advantages and disadvantages of their material characteristics lead to a major disparity in device performance. Therefore, certain impact factors in both these kinds of materials will be discussed in this section, as will some of the typical materials used.

2.3.1 Conjugated Polymers

Given their important role in OFET, the characteristics of conjugated polymer materials, molecular packing mode, and intermolecular interaction can decide the charge carrier transport in the device. In order to perform well, a good understanding of these issues is useful, so as to improve the efficiency of the charge carrier injection and movement in a transistor.

2.3.1.1 P-type conjugated polymer

Positive type conjugated polymer is one of the common organic semiconductors. According to the monomer, the corresponding polymer material can be classified into several species.

2.3.1.1.1 Polythiophene-based class

Polythiophene is one of the classic p-type conjugated polymer materials. The function of the first field effect transistor was as an active layer, fabricated by Tsumura and Ando in 1987 [9]. Due to the very low film quality and molecular weight ($M_n < 3000$), the charge mobility was only10^{-5} $\mathrm{cm}^2/\mathrm{Vs}$. It was also virtually insoluble. Thus, in the decades which followed, there were many attempts to improve solubility and film quality, and looking for a proper method to synthesise good solubility with high regioregularity and molecular weight polythiophene semiconductor material became a central issue in the field. Poly (n-alkylthiophene) (P3AT) was a material which appeared to be attractive due it is propensity to solubility. Depending on the different substitution position of the thiophene ring, this material has three different structures: a high degree of head-to-tail (HT) couplings and a low amount of head-to-head (HH) couplings or tail-to-tail (TT) couplings as shown in Figure 2.5 below.

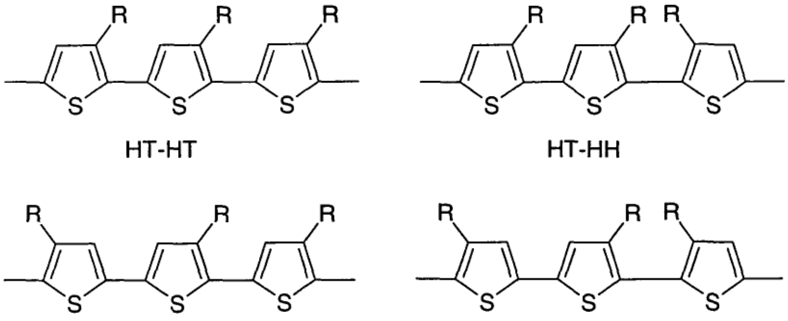

Figure 2.5 Three different structures of P3AT (acquired from Ref [10])

Initially, these three structures tended to exist within the same bulk material, resulting in a film from solution which had no regioregularity area and was poorly conjugated, and where mobility was still very low, only $10^{-7}\mathrm{cm}^2/\mathrm{Vs}$. As the derivative from P3AT, Poly(3-hexylthiophene) (P3HT) possesses relatively more advantages in terms of regioregularity characteristics. The Henning group [11] demonstrated two different orientations of the microcrystalline P3HT domains, with respect to the FET substrate, in 1999. This paper demonstrated that high regioregular (>91%) and low molecular weight was the preferential orientation of ordered domains. It also argued that thiophene rings normal to the substrate and a π-π stacking layer in plane to the substrate, an "edge-on" stacking mode, was beneficial to charge transport along the conjugated backbone; with a π-π stacking orientation, the highest mobility reached was $0.05-0.1\ \mathrm{cm}^2/\mathrm{Vs}$. In contrast, with a low regioregular (81%) and high molecular weight, the orientation was thiophene rings in-plane to substrate and π-π stacking out-plane to substrate, and the charge mobility was only $2\times10^{-4}\ \mathrm{cm}^2/\mathrm{Vs}$. These structures are shown in Figure 2.6 below.

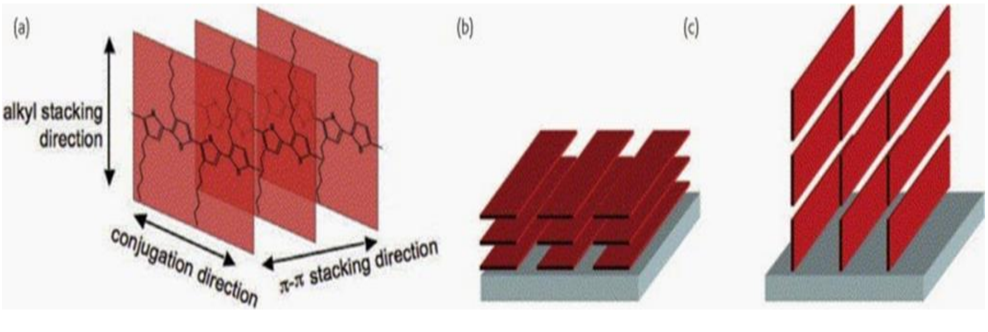

Figure 2.6. The two growth orientation of P3HT molecules piles up on the substrate. (acquired from Ref [12])
(a) Schematic illustration of the charge transport model in lamellae stacking conjugated polymer. (b) Face-on texture of polymeric crystallites; (c) Edge-on stacking texture, the π-stacking and the chain to chain packing of polymers

This experiment demonstrated the relationship in molecular packing using the thin film deposition method. The casting was better than the spin-coating method for P3HT, and in addition, the charge mobility varied with different fabrication methods. Therefore, it is crucial to use the appropriate packing mode in order to make it as regular as using thin film. This must be considered in device fabrication.

Although P3HT appears to be heading in the right direction, its fundamental structural deficiency means that it has limited applicable performance. An ionization potential (IP) of only around 4.8 eV makes it sensitive, and the extra free carrier increases if it is exposed to air for a while [13]. The HOMO energy level is determined by the length of the π-orbital conjugation extension by reducing the conjugation length to decrease the HOMO energy; as such, increasing the material's air-stable ability has been a common approach in polymer chemistry. Based on this notion, Professor Beng [13] and his colleagues designed and synthesized a novel thiophene-based semiconductor, poly (3, 3"-dialky-quaterthiophene) (PQT-12) in 2003. The chemical structure of this material is shown in Figure 2.7 below.

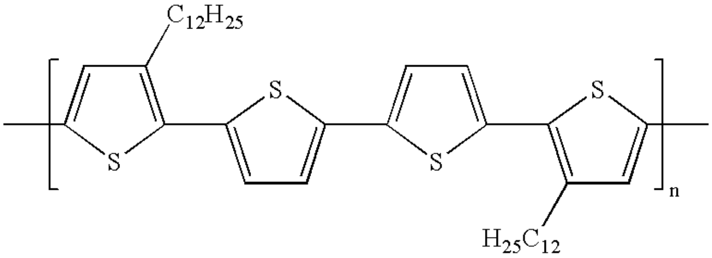

Figure 2.7. The chemical structure of poly (3, 3"-dialky-quaterthiophene) (PQT-12) (acquired from Ref [14])

They introduced appropriately long alkyl side-chains and positioned them strategically on the polythiophene rings. Under this method, the length of π-conjugation was effectively shortened because co-planarity deviation in thienylene moieties results from the substitution of side-chains. This proper control of the length of the extended π-conjugation achieves a delicate balance between transistor functionality and oxidative doping stability [13]. By utilizing it as an active layer in OFET, the on/off ratio was 10^7 and the average mobility $0.07 - 0.12\ \mathrm{cm^2/Vs}$ after annealing under 140 °C in ambient condition. The mobility only slightly decreases after being stored under ambient conditions in the dark for one month, thereby showing an excellent anti-oxidative ability. The reason for this is that its ionization potential was increased by 0.1 eV compared to P3HT, leading to more stabilization in the atmosphere. Another characteristic of PQT-12 is its very strong self-assembly ability under appropriate treatment conditions since more free volume was created between adjacent alkyl chains. This regular geometry contributes to the charge transport in the device.

However, side-chain substitution is not the only technique which can adjust the length of π-conjugation: fused-ring substitution in a thiophene backbone is another common mothed. One of the most typical materials is the poly(2,5-bis(3-alkylthiophen-2-yl)thieno[3,2-b]thiophene) (PBTTT) polymer, which was designed and synthesized by Iain McChulloch and colleagues in 2006 [15]. Its chemical structure is illustrated in Figure 2.8.

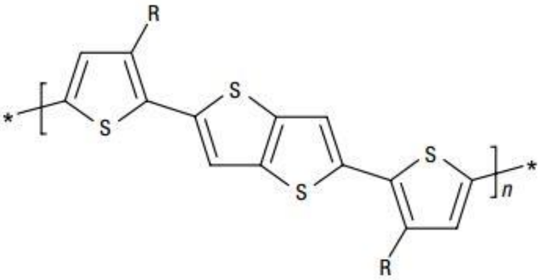

Figure 2.8. The chemical structure of poly(2,5-bis(3-alkylthiophen-2-yl)thieno[3,2-b]thiophene) (PBTTT) (acquired from Ref[16])

From this figure, the main difference between PBTTT and PQT-12 can be seen, namely that it is a linear conjugated comonomer, which was incorporated to form a fused-ring aromatic structure - a thieno[3,2-b]thiophene unit. This unit structure has the ability to limit the movement of delocalized electrons into a thiophene backbone due to the larger resonance stabilization energy of the fused ring as opposed to the single one [15]. Meanwhile, its advanced rotational invariance structure facilitates coplanar conjugation in adjacent molecules, which is beneficial for achieving high ordered conformation stacking so as to acquire high performance. In addition, the IP was increased by 0.3 eV, and it achieved greater air stabilization compared to P3HT. Depending on the different lengths of the R side-chain, PBTTT has three structures, the PBTTT-C10, C12, and C14. Of these, C14 side-chain PBTTT achieved the highest mobility, which was $0.72\ \mathrm{cm^2/Vs}$ with a 5 μm channel length following annealing in a nitrogen atmosphere. The on/off ratio was above 10^6, as can be seen in [15]. In comparison with the C-14 side-chain replacement, the mobility of the C-10 side-chain PBTTT was only $0.3\ \mathrm{cm^2/Vs}$. It is clear that nuance in polymer structure will significantly affect the performance of the material.

In brief, this section looked at three examples of p-type materials, all of which were thiophene-based conjugated polymers.

2.3.1.1.2 Polyfluorene-based class

Fluorene-based conjugated polymers are another significant organic semiconductor material, wherein poly(9,9-dioctylfuorene-co-dithiophene) (F8T2) is the most common and best-known examples. Their chemical structures can be seen in Figure 2.9 below.

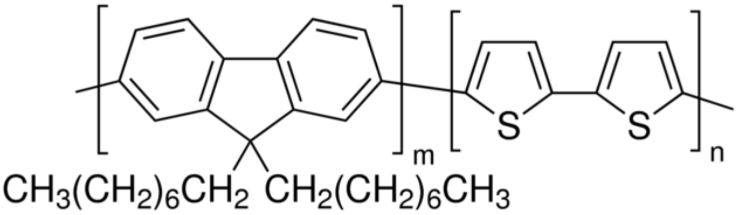

Figure 2.9. The chemical structure of poly(9,9-dioctylfuorene-co-dithiophene) (F8T2) (acquired from http://www.sigmaaldrich.com/catalog/product/aldrich/685070?lang=en&region=GB)

It is based on the simplest unit 9,9-dioctylfuorene (PFO), and its synthetic methods have been described in reference [17]. Indeed, most interest has been expressed in their electroluminescence characteristic. M. Grell et al. [18] comprehensively investigated the characteristics of this materials, specifically the relationship between temperature and crystallization, and their alignment properties and optical properties. They found that the main characteristic of this kind of material is that they can form a highly-ordered nematic liquid crystalline phase through annealing, while the quenching process can suppress material crystallization. Furthermore, Henning Sirringhaus et al. [19] found that although the quenching step could affect crystallization formation, polymer chains are preserved during this phase. Using this aspect, they fabricated a field effect transistor by spin coating F8T2 solution on a starched polyimide substrate and then annealing at 275℃ - 285℃ for 3-15 minutes within an inert nitrogen environment, before finally quenching it. The direction of the backbone and polyimide is consistent. The lowest mobility achieved was $0.002\ \mathrm{cm}^2/\mathrm{Vs}$ and the highest $0.02\ \mathrm{cm}^2/\mathrm{Vs}$, where the current flow was, respectively, perpendicular and parallel to the alignment direction.

Finally, the high ionization potential, 5.5 eV, means that it has a greater capability against chemical doping by atmospheric oxygen, thus having more value in terms of its practical application.

Based on an understanding of fused-ring substitution in PQT-12, Lim et al. [20], replaced thienylene moieties with a thieno[3,2-b]thiophene monomer in the F8T2 backbone as well. An innovative material with a higher crystallinity and a more ordered morphology material, Poly(9,9’-n-dioctylfluorene-alt-thieno[3,2-b]thiophene) (F8TT), was developed. The details of synthesis have been introduced in [21] and its chemical structure can be seen in Figure 2.10 below.

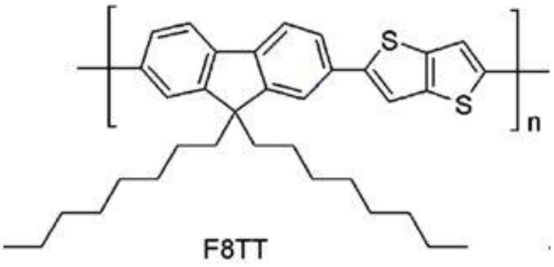

F8TT

Figure 2.10. The chemical structure of Poly(9,9’-n-dioctylfluorene-alt-thieno[3,2-b]thiophene) (F8TT) **(**acquired from Ref [20]**)**

This sort of organic semiconductor combines two advantages found in the earlier materials, that is higher ionization potential, namely 5.38 eV, and reasonable charge mobility, 1.1×10^{-3} $\mathrm{cm}^2/\mathrm{Vs}$, in the field effect transistor. The performance of F8TT really depends on temperature treatment, especially in the annealing and cooling steps. In summary, several p-type conjugated polymer materials in different classes have here been demonstrated, each of which has their own characteristics. A well-organized structure which has high charge mobility and atmospheric stabilization has consistently been the target of organic polymer synthesis.

2.3.1.2 N-type conjugated polymers

Depending on the doping material, conjugated polymers can also be designed and doped as n-types. Poly(benaimidazolebenzophenanthroline) (BBL) was one of the earliest reported n-type conjugated polymer semiconductors. The chemical structure is demonstrated in Figure 2.11.

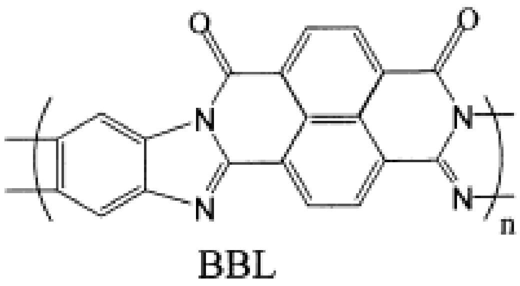

Figure 2.11. The chemical structure of Poly(benaimidazolebenzophenanthroline) (BBL) (acquired from ref [22])

Their air-stable ability attracted researchers, many of whom concentrated on it for some time. The related results concerning BBL and its characteristics have been published by Zhenan Bao et al [23] and Amit Babel with Samson A. Jenekhe [22]. In their report, BBL has low electron mobility and is insoluble in conventional organic solvents, resulting in their narrow application. Another attractive n-type polymer, Poly[N,N'-bis(2-decyl-tetradecyl)-3,4,9,10-perylene diimide-1,7-diyl]-alt-(dithieno[3,2-b:2',3'-d]thiophene-2,6-diyl)P(PDI2OD-DD), was synthesized by Xiaowei Zhan et al. [24] in 2007. This black, solution-processable material exhibits high electron mobility, excellent thermal stability, and relatively high electron affinity. Figure 2.12 shows this kind of polymer chemical structure.

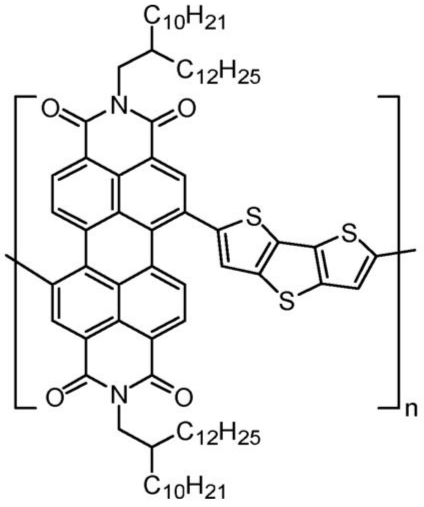

Figure 2.12. The chemical structure of Poly[N,N'-bis(2-decyl-tetradecyl)-3,4,9,10-perylene diimide-1,7-diyl]-alt-(dithieno[3,2-b:2',3'-d]thiophene-2,6-diyl)}P(PDI2OD-DD) (acquired from supporting information of Ref [24])

Under an inert nitrogen environment, the electron mobility is as high as 1.3×10^{-2} $\mathrm{cm^2/Vs}$. Even though the electron affinity is stronger compared with other n-type counterparts, it is still unable to work in a normal environment. For the purpose of air stabilization enhancement, Zhihua Chen and co-workers [25] synthesized an excellent polymer, the poly{[N,N′-bis(2-octyldodecyl)-1,4,5,8-naphthalenedicarboximide-2,6-diyl]-alt-5,5′-(2,2′-bithiophene) (P(NDI2OD-T2) in 2008. Figure 2.13 shows this kind of polymer chemical structure.

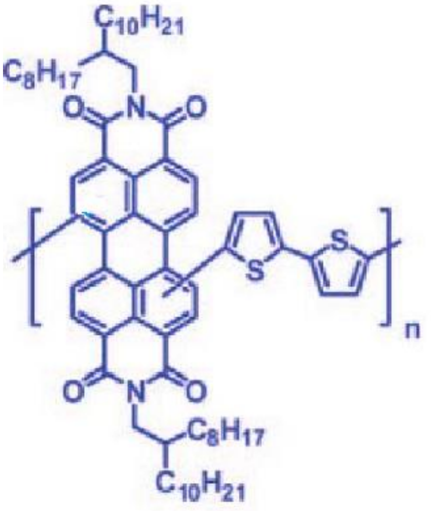

Figure 2.13. The chemical structure of poly{[N,N′-bis(2-octyldodecyl)-1,4,5,8-naphthalenedicarboximide-2,6-diyl]-alt-5,5′-(2,2′-bithiophene)(P(NDI2OD-T2) (acquired from Ref [25])

In contrast, P(NDI2OD-T2) exhibits higher material stabilization due to the fact that the electron affinity of the NDIR co-monomer core is much higher than the PDIR system, wherein P(PDI2OD-DD) results in a firmer chemical structure.

Additionally, in comparison with p-type conjugated polymers, the performance of n-type conjugated polymers is further behind because n-type materials are more sensitive to oxygen, and poor stabilization characteristics seriously affect device performance. In addition, in terms of source and drain electrodes in the transistor, it is necessary that the material, which has a low work function, can match the LUMO energy level in order to inject electrons and reduce contact resistance. Due to these harsh limitations, turning n-type organic semiconductors into real practical applications is still a challenge. It is interesting that replacing a bithiophenen unit with the fused-ring thiophene unit in the synthesis process leads to the acquisition of a highly ordered stacking of planes. It seems that substitution depends on the geometry of the backbone. By ameliorating the experiment conditions, the mobility of electrons in the OFET had reached maximum 0.85 cm^2/Vs with good atmospheric stabilization [26]. At present, the application of n-type material is a long way away. However, it remains an important element (p-n junction) for constructing logic complementary circuits.

2.3.2 Small Molecules (oligomers)

Small molecules are another important class of organic semiconductor. As with conjugated polymers, it can appear in two different forms, according to whether the doping material is p-type or n-type. The difference is that sometimes a small molecule semiconductor is insoluble in an organic solvent, usually through vacuum deposition on the substrate. However, in general, oligomer mobility is higher than that of conjugated polymers. The following section will introduce typical materials of this type.

2.3.2.1 P-type small molecule material

2.3.2.1.1 Fused ring aromatic hydrocarbons

A fused ring aromatic hydrocarbon is composed of multiple aromatic benzenes which share a pair of carbon atoms closely tied together. This class of compound contains only hydrogen and carbon. Depending on the number of benzene rings, the name and chemical characteristics changes. Taking pentacene as an example, all the benzene rings are planar and single, and the double bonds alternate regularly, thereby forming conjugated double bonds. Its chemical structure can be seen in Figure 2.14.

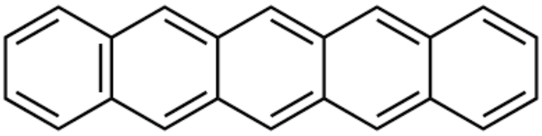

Figure 2.14. The chemical structure of pentacene (acquired from http://www.sigmaaldrich.com)

Thus, a P_z-electron can delocalize in the entire molecule. In fact, its semiconductor-like property was discovered in 1960. It was not until 2003 that the first OFET, with pentacene thin film as its active layer, was finally successfully created by the Kelley group [27]. The mobility of the holes in the device was above $5\ \mathrm{cm^2/Vs}$.

After this, it became clear that small molecule material had enormous potential in organic transistor devices. In 2007, the Palstra group [28] constructed a pentacene single-crystal OFET, where the highest mobility was $40\ \mathrm{cm^2/Vs}$. From Figure 2.15, it can be seen that pentacene is composed of five parallel benzene rings which are closely tied together. Compounds composed of two, three and four benzene rings also exist, namely naphthalene, anthracene, and tetracene. Their structural diagrams can be seen in Figure 2.15.

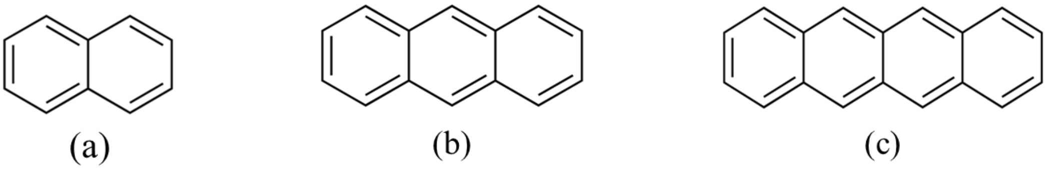
(a) (b) (c)

Figure 2.15. The chemical compounds of p-type fused aromatic hydrocarbons (a) naphthalene (b) anthracene (c) tetracene
(acquired from www.sigmaaldrich.com)

The mobility of all of these compounds is lower than pentacene. The charge carrier mobility of anthracene signal crystal is only $0.02\ \mathrm{cm^2/Vs}$ under low-temperature environment [29], and hole mobility of the thin film and single crystal of tetracene are reached at $0.10\ \mathrm{cm^2/Vs}$ [30] and $1.3\ \mathrm{cm^2/Vs}$, [31] respectively. The reason is as the number of benzene rings increases, the compound stabilization decreases. Therefore, pentacene is the best for parallel fused ring aromatic hydrocarbon organic semiconductors. Although pentacene has high hole mobility, its low solubility, and poor air stabilization seriously limits its application. In particular, pentacene in position 6 and 13 react easily with oxygen to form quinone, this kind of impurity results in a π-orbital overlap in the active layer and lowering the performance of the device [32]. By using this characteristic, the Anthony group considered functional group modification of these two positions so as to enhance its soluble ability and hole mobility [33]. In an experiment, five different functional groups were added to the pentacene molecule. In these pentacene derivatives, TIPS-pentacene demonstrated the best performance, with its field effect mobility improving to $0.4\ \mathrm{cm^2/Vs}$ [34].

2.3.2.1.2 Porphyrin and phthalocyanine macrocyclic molecules

Porphyrin and phthalocyanine macrocyclic molecules are very special organic compounds. Their central empty position provides the opportunity for combination with various metallic elements in order to create new materials. Both of their chemical structures are shown in Figure 2.16 below.

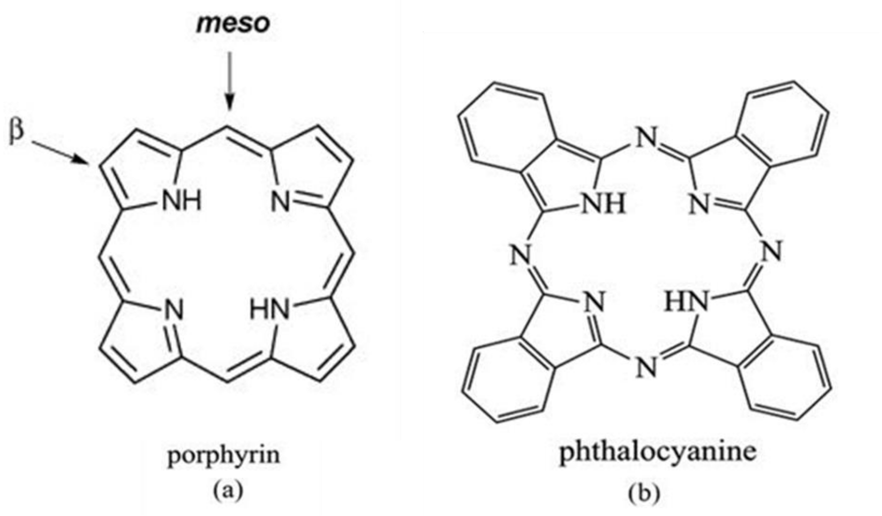

Figure 2.16. The chemical structure of porphyrin and phthalocyanine macrocyclic molecules. (a) porphyrin (b) phthalocyanine (acquired from Ref [35])

Copper phthalocyanine (CuPc) is one such excellent compound. As suggested by the name, phthalocyanine’s central position is occupied by a copper atom. The compound structure is illustrated in Figure 2.17.

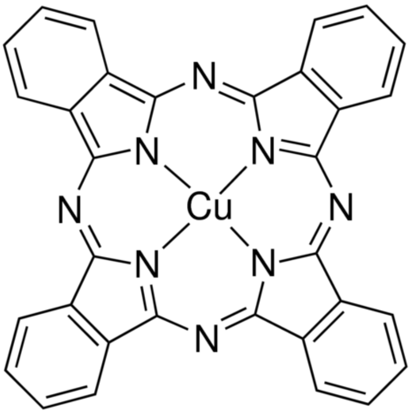

Figure 2.17. The chemical structure of Copper phthalocyanine (CuPc) (acquired from http://www.sigmaaldrich.com/catalog/product/aldrich/546682?lang=en&region=GB)

In 1996, Bao et al. investigated its field effect mobility dependency on temperature [36]. Through the use of vacuum deposition film on various temperature substrates, they found that mobility was increased when the substrate temperature was elevated in a vacuum, with the highest mobility achieved being $0.02\ \mathrm{cm^2/Vs}$, where the substrate temperature was 150℃. This series of experiments also proved that temperature could affect the degree of film crystallization, resulting in changes in orientation and mobility. In 2005, Zeis et al. [37] conducted a signal crystal OFET experiment, where the mobility achieved was $1\ \mathrm{cm^2/Vs}$ in darkness and air environment.

Another macrocyclic, porphyrin, also with a central unfilled structure, can also combine with metals to form metalloporphyrin. In addition, under different conditions, benzene substitution can occur at the porphyrin four *meso*-positions, or form porphyrins bearing benzene rings fused at the four *β*-pyrrolic positions. The former is known as 5,10,15,20-tetraphenylporphyrin (H_2TPP) [38, 39] and the latter tetrabenzoporphyrins (TBPs), the synthesis process of which is complicated and can be found in [40]. The molecular structures can be seen in Figure 2.18.

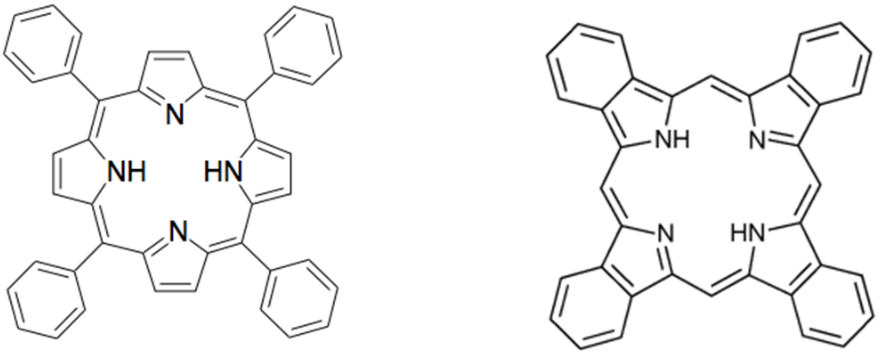

H_2TPP (a)

TBPs (b)

Figure 2.18. The chemical structure of both of macrocyclic compounds (a) 5,10,15,20-tetraphenylporphyrin (H_2TPP) (b) tetrabenzoporphyrins (TBPs) ((a) acquires from http://www.nanoniele.jp/cgi-bin/nanoniele.cgi?inputsite=abbsearch&keyword=H2TPP and (b) acquires from Ref [40])

G. Conte's group [41] conducted an experiment. Firstly, the H_2TPP was dissolved in chloroform, and it was then deposited by the spray method on the substrate to build the OFET. The measurement undertaken in a vacuum at room temperature revealed that the mobility was $0.012\ \mathrm{cm^2/Vs}$. Another macrocyclic, tetrabenzoporphyrins (TBPs), which precursor synthesis process can be found in [42]. In my experiment, the TBPs precursor centre is occupied by nickel (NTBs). Its molecular structure can be seen in Figure 2.19 below, and the related details will be provided in Chapter 6.

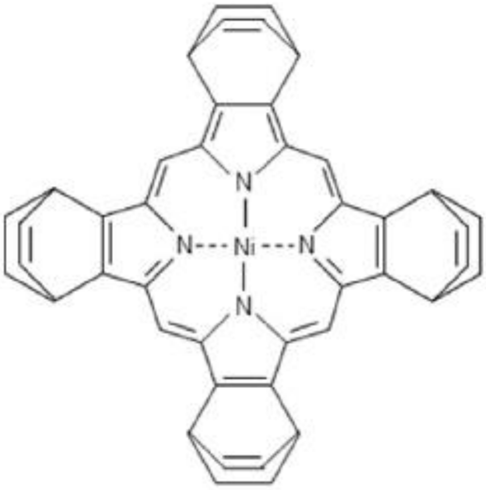

Figure 2.19. The chemical structure of nickel- tetrabenzoporphyrins (NTBs) precursor (acquired from Ref [43])

2.3.2.2 N-type small molecule materials

In n-type small molecule semiconductor design, one crucial point is material air stabilization. Therefore, finding a method to reduce LUMO energy level to eliminate air sensitivity, as well as Schottky barrier, thereby making it match with an inert metal work function is a possible future direction.

Bao et al.[44], based on a previous experiment, introduced different metal elements, such as copper, zinc, and cobalt in phthalocyanine in order to synthesize different metallophthalocyanines, before all hydrogen elements were substituted by halogen elements, such as fluorine and chlorine. The result was the formation of n-types, such as F_{16}CuPc perhalogenated metallophthalocyanines organic semiconductor. The chemical structure has been illustrated in Figure 2.20 below.

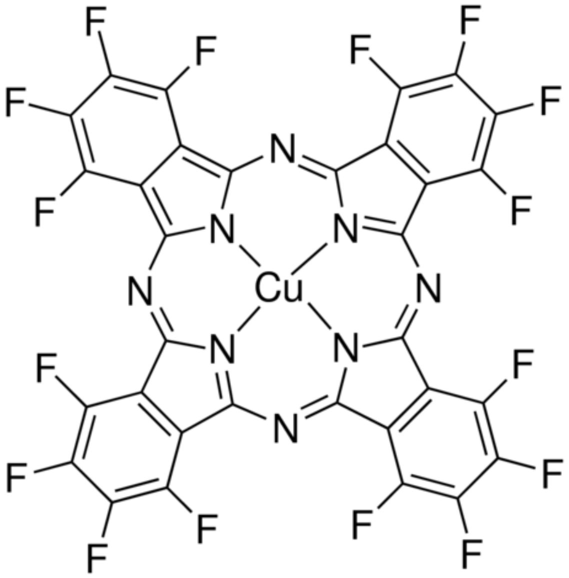

Figure 2.20. The chemical structure of F_{16}CuPc. (acquired from http://www.sigmaaldrich.com/catalog/product/aldrich/446653?lang=en&region=GB)

An OFET constructed by vacuum deposition contains small molecules on the same type of substrate at different temperatures. These results prove that electron-withdrawing groups (fluorine) are able to lower the LUMO energy levels of molecules, elevating the air stabilization of n-type materials; at the same time, the field-effect mobility is strongly dependent on metal coordination, and the substrate temperature for deposition was again verified [44].

In 1998, the Suzuki group [45] synthesised perfluoropentacene ($C_{22}F_{14}$) compound, the structure of which can be seen in Figure 2.21 below.

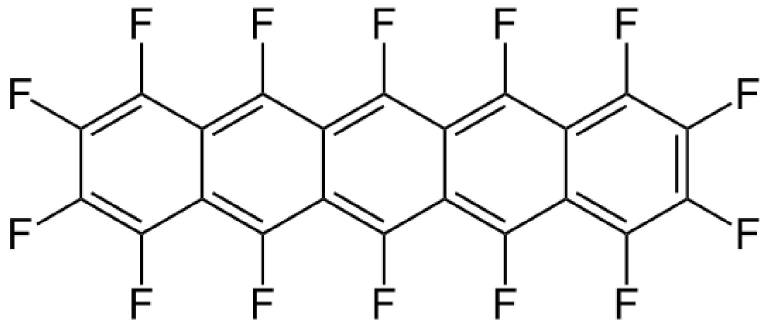

Figure 2.21. The chemical structure of perfluoropentacene (acquired from https://commons.wikimedia.org/wiki/File:Perfluoropentacene.svg)

The thin film active layer was a high vacuum deposition on an OTS-treated substrate at various temperatures in OFET transistor fabrication, and the mobility measurements were taken at room temperature in a vacuum chamber. A highest mobility of $0.11\ \mathrm{cm^2/Vs}$ was observed at a substrate temperature at 50°C. This group also built bipolar OFETs by using perfluoropentacene and pentacene together. The field-effect mobility for the operations of holes and electrons are, respectively, 0.52 and $0.022\ \mathrm{cm^2/Vs}$ [45].

In order to well align the small molecule semiconductor LUMO band with metal electrodes energy level to get efficient electron injection, the Hu group [46] designed an OFET by using asymmetrical electrodes (Au/Ag) with a single crystal instead of thin film F_{16}CuPc. The result was a much superior device performance, where the electron mobility was $0.2\ \mathrm{cm^2/Vs}$ with an on/off ratio of over 6×10^4.

2.4 Organic Polymer Field Effect Transistors

So far, we have reviewed the conductivity mechanism of an organic semiconductor and understood the material can be divided into two classes according to their chemical properties. In this section, we will continue recalling, but the focus switch to the organic material application in electronics device: organic field effect transistor (OFET).

2.4.1 Device Structures and Theory

2.4.1.1 Field effect transistor structures

Depending on the location of the gate deposition, transistor structures can be divided into two types: top-gate and bottom-gate. Each contains two types because the source and drain electrodes have a different semiconductor layer combination. Therefore, in total, there are four structures, all of which are illustrated in Figure 2.22 below.

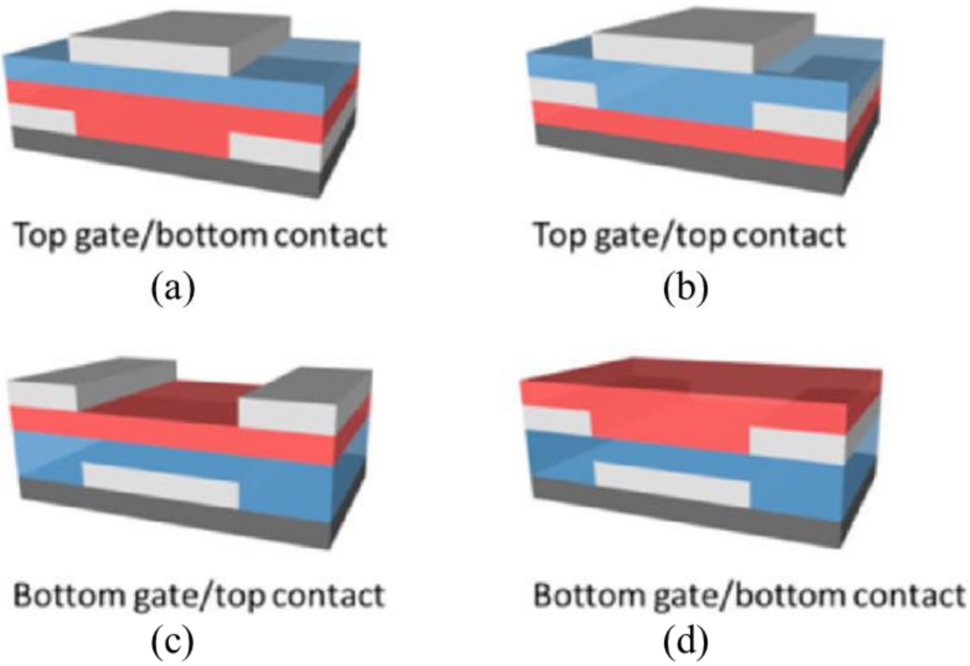

Figure 2.22. Schematic diagrams of the four common transistor architectures with the electrodes in pale gray, dielectric in blue, semiconductor in red, and substrate in dark gray.

(a) Top-gate bottom-contact (TGBC) (b) Top-gate top-contact (TGTC)
(c) Bottom-gate top-contact (BGTC) (d) Bottom-gate bottom-contact (BGBC)
(acquired from Ref [47])

From the device structures presented above, it can be seen that a transistor is manipulated by three electrodes: source, drain, and gate. Herein, the semiconductor layer always is always in contact with the source and drain, separated from the gate by a dielectric layer. At present, the most popular structures are (b) and (c). In both cases, the organic semiconductor can be deposited on the insulator layer before the deposition of metallic electrodes. This method can effectively improve the quality of the interface between the semiconductor and insulator layer. The interface quality is a very important factor in device fabrication. Since the organic material grown on different substrates will occasionally exhibit different properties, thereby deciding the device performance.

In this way, the interface between these two layers is very uniform, reducing the probability of the charge carrier trap. In contrast, for the other two structures, the molecular crystals have to grow on two kinds of materials (metal and dielectric material) at the same time, which will almost certainly result in the structure and properties being completely different on these two surfaces, thereby increasing the probability of obstructing the charge carrier injection. This would decrease the device performance, potentially even resulting in no response at all.

2.4.1.1 Device working theory

The transistor charge carrier injection mechanism is clarified in Figure 2.23 [48]. The LUMO and HOMO bands of the organic semiconductor correspond to two metallic electrodes at the Fermi level. To take the n-type as an example, in the case of gate bias, it is zero, and even when applying a voltage between the source and drain electrodes, there is no current flow because there is no charge carrier movement in the semiconductor layer. As the gate bias increases, a large electric field is produced at the interface between the semiconductor and dielectric layers. This field causes LUMO lever band bending which aligns it with respect to the Fermi level of the metal contact, if the gate voltage is large enough, thereby making the LUMO and Fermi level resonation (flat band). In addition, negative charges begin to accumulate in the LUMO band before applying a small positive voltage, meaning that current can flow from source to drain contacts.

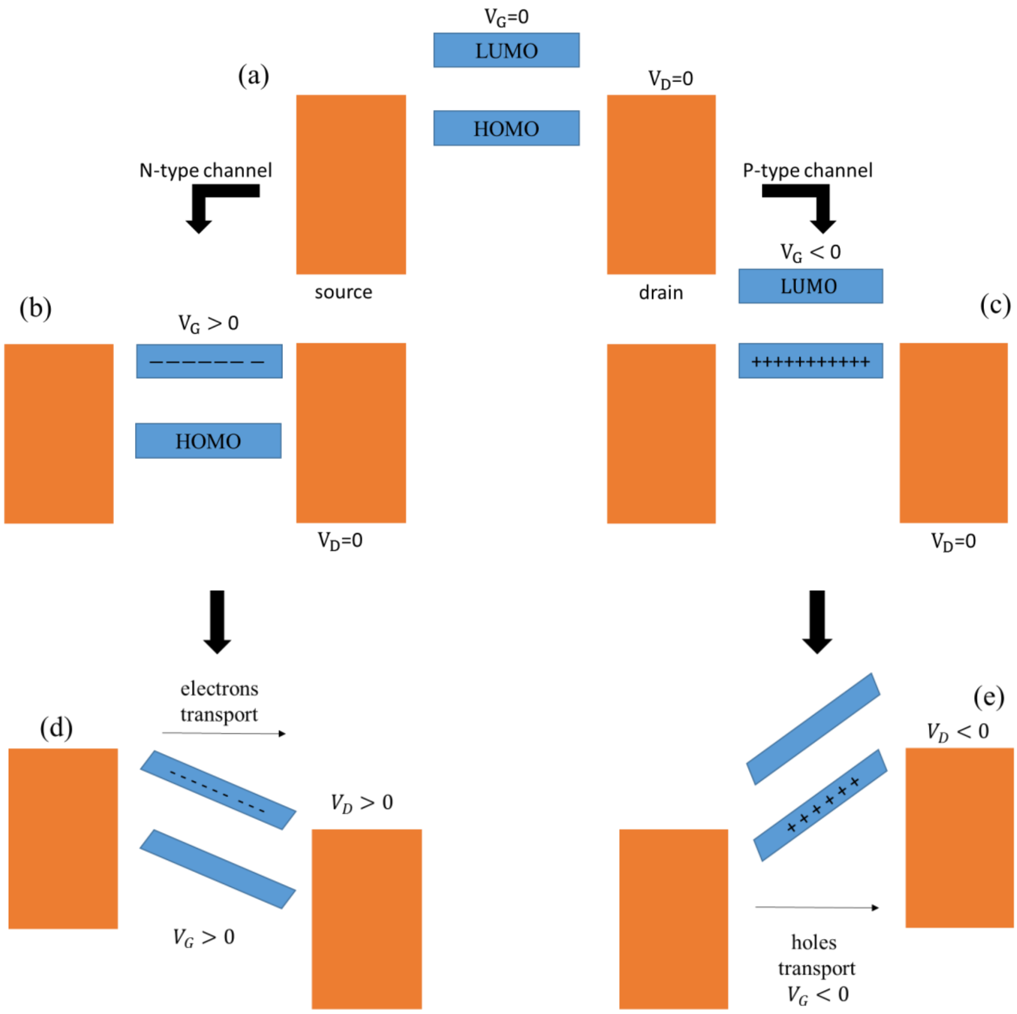

Figure 2.23. The Charge carrier injection
(acquired from Ref [48])

For the p-type, once there is a negative bias on the gate, the HOMO band will align and resonate with electrodes at the Fermi level when the negative gate voltage is sufficient, resulting in holes slowly gathering in the HOMO. A small voltage between the source and drain leads to current flow in the semiconductor layer.

2.4.2 Fundamental parameters

Every device has its own standard, which is also true for transistors. Some key parameters used to evaluate device performance will be examined in this section, specifically charge mobility (μ), on/off ratio, threshold voltage (V_T) and subthreshold (S). The majority of the time, these parameters can be captured by a transfer curve ($I_D - V_G$) and output curve ($I_{SD} - V_D$). An example of both these types of curves can be seen in Figure 2.24.

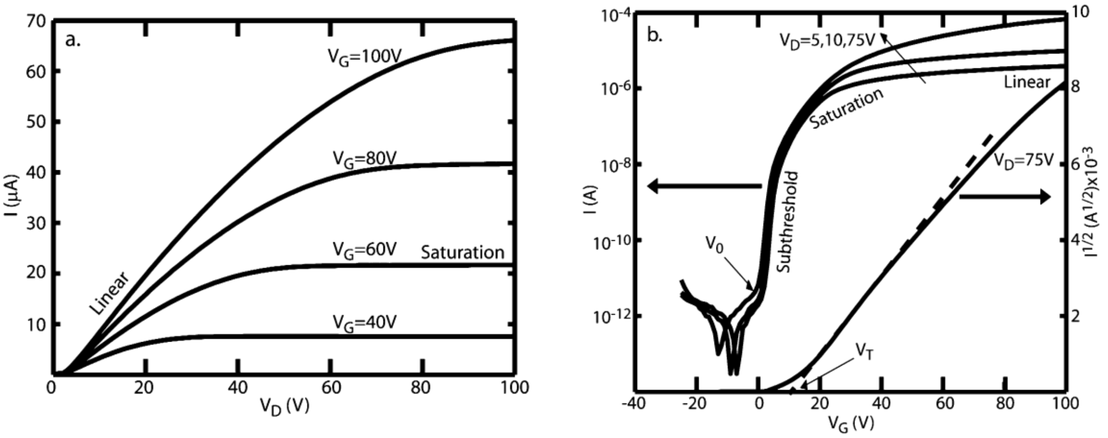

Figure 2.24. The information of working parameters
(a) Output curve (b) Transfer curve
(acquired from Ref [48])

2.4.2.1 Threshold and Sub-threshold

The threshold voltage is the minimum gate voltage required for accumulating the charge carriers at the OSC/insulator interface forming a conducting path between the source and the drain [49]. In general, it is hoped that the threshold voltage is as low as possible so that even a small voltage can drive and make a transistor work. The concept of threshold has been investigated by Gilles Horowitz's group [8]. In his concept, the threshold voltage can usually be determined from a transfer curve. Its value can be acquired by drawing a tangent line from the linear region of $\mathrm{I_d}^{1/2}$ to the $\mathrm{V_G}$ value on the abscissa. The intercept point is the value. In Figure 2.25 (b), in this n-type transistor transfer curve, the threshold value is about 10 V. 'Subthreshold' is another important parameter, which can weigh the speed of current change when the transistor switches from on to off. The equation for this is [50]:

$$\mathrm{S} = \mathrm{d}V_g/d\,(\log \mathrm{I_d}) \qquad (1)$$

The unit of S is mV/dec; a smaller value of S indicates a smaller voltage change requirement and the device switches more quickly from "on" to "off".

2.4.2.2 The on/off ratio

The on/off ratio actually is the transistor $\mathrm{I_{sd}}$ ratio between the "on" and "off" condition. It is also a significant parameter which can reflect the device switching performance under a given gate bias and can usually be calculated using an exponential transfer curve. In Figure 2.25 (b), at the point of $\mathrm{V_0}$, the transistor is switched on and switched off at the linear region. Therefore, the on/off ratio is about 10^5. In device performance evaluation, it is hoped that the ratio is as high as possible. A low ratio indicates that the value of an on and off current is so close that the transistor cannot be turned off. Figure 2.25 (b) also illustrates that if the gate bias increases, the ratio's magnitude is affected to some degree, although the effect is limited.

2.4.2.3 Charge carrier mobility

The key factor that characterizes charge transport is the carrier mobility [8]. This parameter reflects hole and electron mobility in organic semiconductor within different electric fields. Figure 2.24 (a) is a classic transistor output curve, I_{sd} which increases with an increase in gate bias. The output contains two parts: the linear regime and saturation regime. As such, mobility in these two regions differs. In a review by Horowitz [8], the *I-V* (current-voltage) expression derived for inorganic-based transistor in the linear and saturation regimes was shown to be readily applicable to organic transistors. The expression in the linear regime is:

$$I_{sd} = \frac{W}{L}\mu C(V_G - V_T) \tag{2}$$

In the saturation regime, the formula is:

$$I_{sd} = \frac{W}{2L}\mu C(V_G - V_T)^2 \tag{3}$$

where, I_{sd} is the current between source and drain electrodes. W and L are the length and width of the channel, respectively; μ is the charge carrier mobility, C is capacitance, V_G is the gate voltage and V_T is the threshold voltage.

2.5 The Organic Electro-Chemical Transistor (OECT)

The application of conjugated polymeric materials is not limited to the semiconductor level. Depending on the results of synthesis, different doping levels and methods, its conductivity can exhibit different ranges, sometimes even rivalling conductors.

2.5.1 Materials and properties

During the second half of the 1980s, scientists at the Bayer AG research laboratories in Germany developed a new polythiophene derivative, poly(3,4-ethylenedioxythiophene), abbreviated as PEDOT or PEDT [51]. The chemical structure of material is shown in Figure 2.25 below.

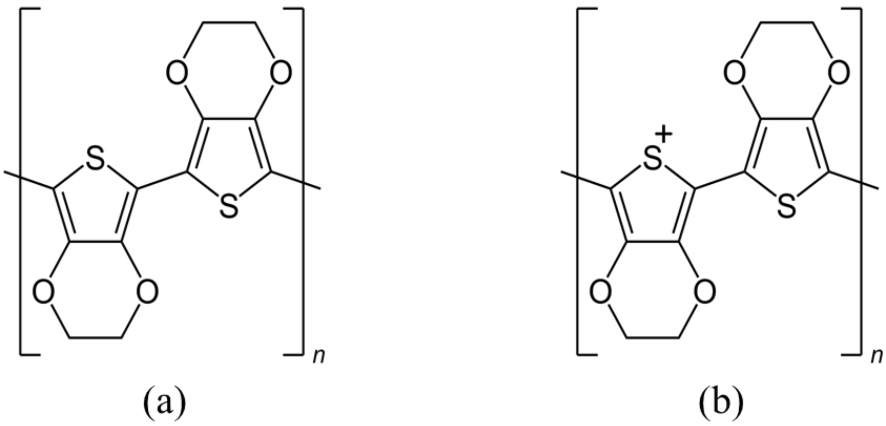

Figure 2.25. (a) The chemical structure of poly(3,4-ethylenedioxythiophene) (PEDOT) (b) The oxidation status of PEDOT (acquired from https://en.wikipedia.org/wiki/Poly(3,4-ethylenedioxythiophene))

In the early synthesis stage, PEDOT was a kind of black, insoluble, polymerized from EDT monomer, with a high conductivity (300 S/cm) [51]. It is characterized by a thin transparent film and the ability to have a strongly oxidized state in the air [52, 53, 54]; as such, it quickly attracted the attention of both industry and academia. However, in terms of its application, its insolubility was still a major drawback. This solubility defect was overcome by blending it with a kind of water-soluble charge-balancing dopant polyelectrolyte, poly(styrene sulfonate acid) (PSS), where the chemical structure has been illustrated in Figure 2.26 below.

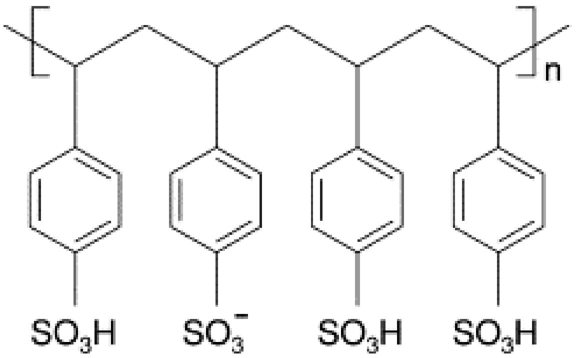

Figure 2.26. The chemical structure of poly(styrene sulfonate acid) (PSS) (adapted from Ref [55])

So they could combine to yield a polymeric material, PEDOT/PSS [51, 30].

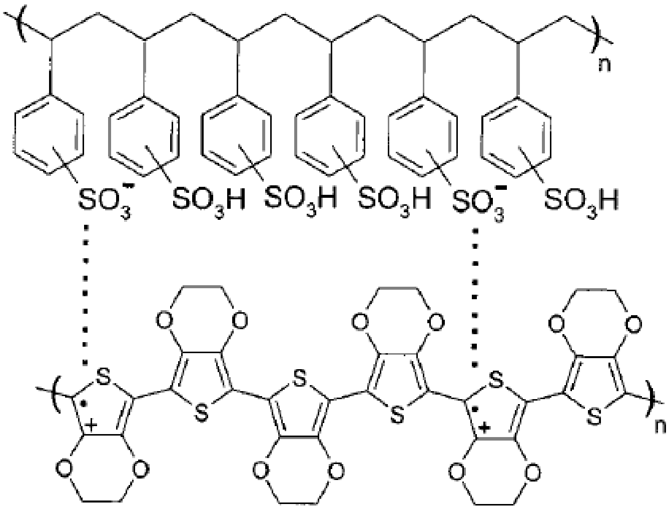

Figure 2.27. The chemical structure of blending PEDOT and PSS acid (acquired from Ref [51])

This kind of polymerization method for EDT is called BAYTRON P and was developed at Bayer AG [51 (ref 11,12)]. This polyelectrolyte can be dissolved well in water with high conductivity (10 S/cm) and has visible light transmissivity, good film-forming ability and excellent ambient stability properties [51]. The interesting aspect is, after drying, the film becomes insoluble in any common solvent [51]. This polymeric material has been employed in several different areas, such as chemical sensors [56] and light emitting diodes [57].

There are several techniques for EDOT-based monomer polymerization. Using PSS as an oxidative agent is one of the most common and practical methods. Through complexing with different oxidative solutions, the result is that polymeric materials exhibit different properties. For instance, replacing the PSS with iron(III) tris-p-toluenesulfonate ($Fe^{III}(OTs)_3$) to form PEDOT-OTs is another option that was invented by De Leeuw et al [58] and developed by Bayer AG [59]. Through this development, the maximum conductivity exceeds 1000 S/cm. In addition, in recent years, conducting polymers have exhibited attractive thermoelectric, even semi-metallic properties. Olga et al. have comprehensively studied the relationship between the thermoelectric and oxidation level of the material [60] and the semi-metallic features [61]. The PEDOT/PSS conductivity could be enhanced by organic solvent treatment. Ouyang group [62] found that the PEDOT:PSS film which is soluble in water becomes insoluble after treatment with ethylene glycol (EG), and EG treatment can lower the energy barrier for charge hopping among the PEDOT chains, lowering the polaron concentration in the PEDOT:PSS film by about 50%, and increasing the electrochemical activity of the PEDOT:PSS film in NaCl aqueous solution by about 100%. According to the type of dopant, neutral PEDOT can also be doped to an n-type material using a reducer. Ahonen et al. doped n-type PEDOT and confirmed that it is unstable, even in an extremely dry-oxygen-free environment [63], thus making n-type PEDOT/PSS hard to use.

2.5.2 The Field Effect Transistors

Based on these excellent behaviours, PEDOT/PSS can be implemented in several applications, in particular, large area flexible logic circuitry design. The Nilsson group [56] created a humidity sensor based on an organic electro-chemical PEDOT/PSS transistor, where because of its water soluble characteristic, the substrate of the device was plastic foil and ordinary paper rather than conventional silicon substrates. Touwslager et al. [64] designed and successfully fabricated complex, all-polymer integrated circuits by patterning PEDOT/PSS as electrodes on a wafer. This experiment broke through the ink-jet printing limitation, providing a good direction on using organic materials as electrodes to realize large-area flexible electronics device fabrication. In the medical profession, the Biscarini group [65] employed PEDOT/PSS, poly(L-lactide-co-glycolide) (PLGA) and electrolyte gate, fabricating an organic electrochemical transistor as a prototype in order to build an electrocardiographic (ECG) recording device. In the case of an organic electro-chemical transistor (OECT) based ECG sensor, the recording occurs by attaching the transistor's exposed PEDOT:PSS channel directly on the skin, which replaced the role of the gate, to measure the cardiac rhythm. This state of the art result highlights the feasibility of realizing simple organic bioelectric interfaces on implantable bio-scaffolds which would allow the recording of signals from muscular or nervous tissue to monitor health state.

All of these examples clearly show that PEDOT/PSS can be widely used in practical applications due to its superior behaviour.

2.6 The “Coffee-stain” Effect

2.6.1 The “Coffee-stain” effect phenomenon

The “coffee-stain” effect is a very common phenomenon in our life. Coffee left overnight can form a ring-shaped stain caused by the underside of the cup. This is true not only for coffee droplets but also all droplets containing non-volatile solutes drying on a solid surface, all of which can leave a high density, ring-like deposition. This interesting phenomenon was first analyzed in the pioneering work by Deegan [66]. One of the main proposals in his paper was that this form of deposition could be predicted and controlled, no matter what the nature of the liquid, solute, and substrate. All that would need to be satisfied are the following conditions: that the solution on the substrate has a contact angle, that the contact line is pinned on the substrate, and that the solvent can evaporate. In the coffee-ring set up process, the contact angle plays a significant role. The angle can be determined by the interfacial tensions between the liquid, solid and the ambient medium which is usually air [67], as can be seen in Figure 2.28. Depending upon the degree of the contact angle when the droplet spreads on the substrate and reaches an equilibrium state, its nature will change. If the angle is less than 90 degrees ($\theta < 90°$), the substrate surface for the droplet will be hydrophilic; in contrast, if the value is greater than 90 degrees (θ > 90°), it will be hydrophobic.

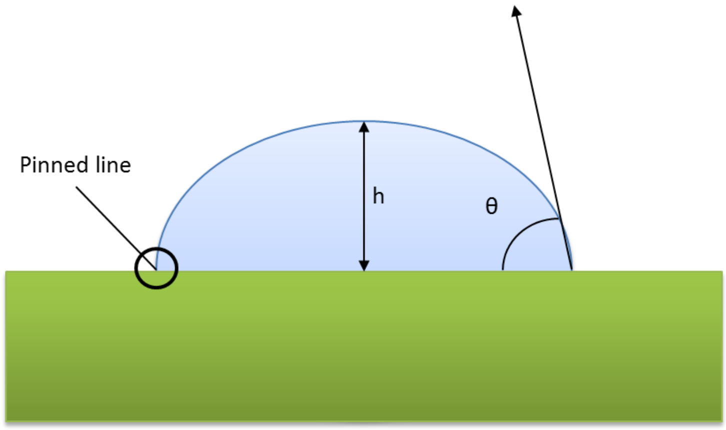

Figure 2.28. A droplet on a hydrophilic substrate surface

When it is hydrophilic, the contact line can easily be pinned onto the edge of a droplet which has a flat surface. In such a case, the droplet radius and shape are fixed and reach equilibrium status. A process of sessile droplet evaporation, with three distinct phases, has been clearly described by Mampallil [67]. In the first stage, due to the rapid liquid molecular motion, the vapour on the surface of a droplet quickly reach saturation and diffuses into the air leading to the contact angle (θ) magnitude beginning to decrease. At the same time, the droplet height also decreases. When the contact angle decreases to a certain level, the contact line begins to slip over the surface. In the second stage, the contact angle remains fixed while the droplet size shrinks. The contact line moves in a stumbling way. In the final stage, both the droplet radius and the contact angle decrease sharply. However, on a highly hydrophilic surface, the second and third stages do not, in fact, exist because the contact line was already pinned onto the textured surface, and when the liquid contains non-volatile solute particles, it is much stronger.

“Coffee-ring” geometry is formed by the aggregation of colloidal particles on the edge of a drop when the liquid dries out. According to Deegan, the capillary force was the reason that particles finally were pushed and deposited on the vicinity of the contact line. The Nagayama group [68] studied the mechanics of this force between colloidal particles in detail.

The capillary force consists of two parts, namely ‘floating force’ and ‘immersion force’, where the former is related to particle weight and the latter is determined by the liquid thickness of the particle diameter. Snoeijer et al [69], through observation of the geometry of the edge of the ring, found that colloidal particle arrangement in the “coffee-stain” is not homogeneous, but rather an ‘order-to-disorder’ process. The specific sequence of this is square packing, hexagonal packing and then disordered packing. Figure 2.30 clearly demonstrates these three phases. It shows that at the initial stage, the velocity of the molecules’ thermal motion is slow, meaning that particles have sufficient time to arrange themselves through Brownian motion and form an ordered structure, while at the final phase, there is insufficient time for molecules to rearrange their position and form a disordered structure.

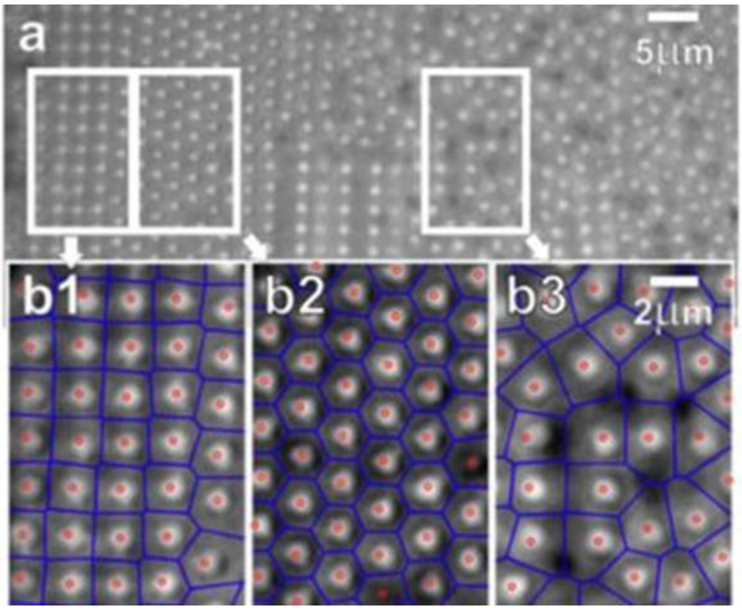

Figure 2.29. The order-to-disorder partials arrangement during stain formation (acquired from Ref [69])

Another interesting phenomenon during the evaporation process is that the droplet surface engenders a temperature gradient. Its lowest point is located on the highest vertical place from the isothermal solid surface to the droplet curved surface because this is the farthest distance between them. This gradient causes a difference in droplet surface tension. In addition, the droplet inside forms a concentration gradient because of the different evaporation rate on the droplet surface. Combining these two factors, a Marangoni flow [70] is generated in the sessile droplet [67]. This flow can provide a small compensation for the liquid evaporation from the edge, which provides the dispersed particles with an assisted flow outward to that point combination. Capillary flow, meanwhile, forms the “coffee-ring” at the end of evaporation [67], which can be seen in Figure 2.31 below.

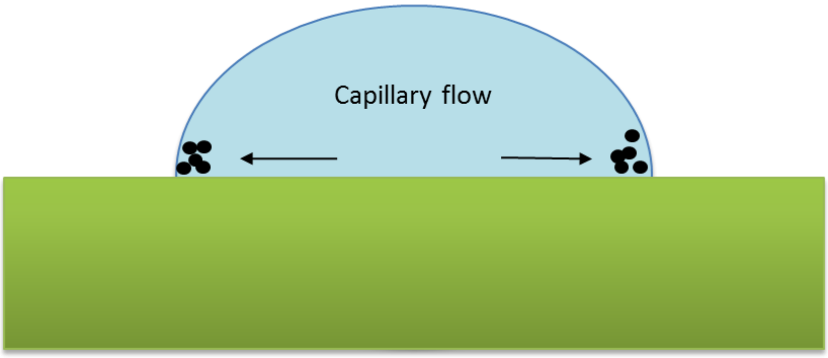

Figure 2.30. The particles move forward to the edge of the pinned contact line by capillary flow at the end of evaporation and finally form the "coffee-ring" geometry.

2.6.2 The "Coffee stain" effect in applications

Transparent conducting electrodes are essential components in some organic device fabrication processes, such as organic solar cell (OSC) [71], touch screen [72] and organic light emitting diodes (OLEDs) [73]. The conventional electrodes are fabricated via photolithography, or e-beam lithography, however, each of them has inherent limitations, such as requiring an expensive vacuum system, which is very difficult in the commercialization of low-cost large area electrode deposition. As mentioned above, non-volatile or colloidal particles flux can be pushed toward the substrate-liquid-air contact line and finally self-assemble due to convective flow during the solvent evaporation process. Some scientists take advantage of this mechanism to develop several inexpensive routes toward obtaining well-ordered material structure on large areas.

2.6.2.1 Patterning nanoparticle wires, grids by flow coating

The flow coating technique, used in conjunction with functionalized nanoparticles, is ideal for self-assembly and generation of functional objects [74]. The flow coating equipment consists of a knife blade which is positioned above a translation stage at a certain distance and angle, as shown in Figure 2.31.

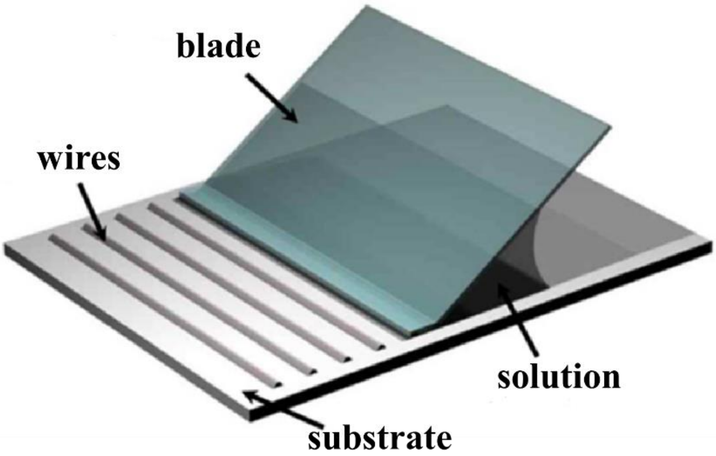

Figure 2.31. The flow coating apparatus components (acquired from Ref [75])

It depends on the "coffee-ring" effect mechanism, at the stage of horizontal translating, the solution can be loaded and trapped between these two plates by capillary force. As the solvent evaporates, these non-volatile solutes migrate and are carried to the pinned contact line by convective flow. By controlling the intermittent stage stopping time and shift distance under a certain velocity, see Figure 2.32 below, this cost-effective technique could lead to well-aligned material geometry.

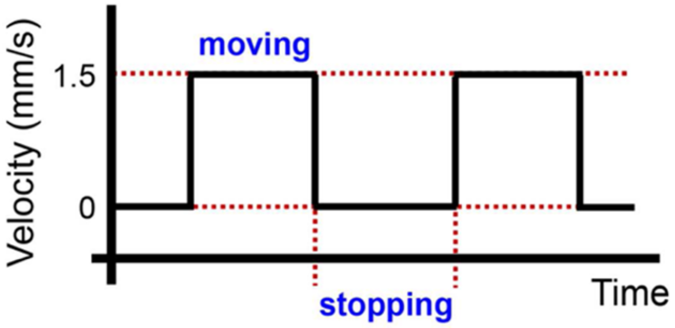

Figure 2.32. The stage intermittent moving and stopping at a fixed velocity. (acquired from Ref [75])

In 2010, Crosby *et al*. [74] reported the spontaneous, controlled formation of striped patterns of CdSe-based nanoparticles on underlying substrate by the flow coating method. In his work, one kind of material wires was well patterned on the substrate at first. Then, the part of nanoparticle (NP) ligands in stripes were cross-linked by UV-irradiation to enhance the degree of stripes robust, otherwise, these wires are completely dissolved on the second wire patterning process. Another sort of CdSe-based nanoparticle with different ligands was the second material which was patterned successfully either perpendicular or parallel to the first pattern, without any overlying or deformation at the junction point on the grid structure. Therefore, he concluded that the grid structure cannot be achieved by micro-contact printing (μCP) due to the deformation of PDMS during the second time patterning [76]. In addition, he also mentioned that this fabrication method was applicable to some other materials, such as Au nanoparticles, PMMA, and even polydimethylsiloxane (PDMS) to form well-ordered stripes geometry with different space size. In the same year, Ressier's group [77] published the capabilities of convective self-assembly (CSA) to fabricate well-ordered centimetre-long conductive nanoparticles wire arrays from aqueous suspension of 18 nm gold colloids on flat, non-patterned $\mathrm{SiO_2/Si}$ substrates. The remarkable result of their experiment was that the orientation of wire array growth can be switched 90° automatically during the drying, changing from parallel to perpendicular to the moving meniscus, just by controlling the substrate temperature. Such wire array orientation changes due to the temperature decrease were first observed and obtained and that phenomenon also revealed that the solution convective flow really depends on the substrate temperature. With the lower temperature, these particles cannot acquire adequate energy and move slowly to the meniscus because the convective flow inside the droplet is slow as well. As a consequence, they cannot protrude the liquid-air interface and are not pinned to the substrate, resulting in nanoparticle accumulation at the meniscus. When the density reached the critical point, the nanoparticle could pin on the substrate, and the tip of the wire protrudes perpendicularly to the meniscus, thus, forming a new orientation of the wire array. Such a discovery of a tuneable orientation wire array fabrication method provides a new opportunity for nano-device application. The flow coating technique seems to provide an effective way for low-cost large area electrodes deposition; in addition, the space between electrodes can be flexibly controlled compared to the implementation of a lithographic mask. This advantage is able to benefit those electrical devices, such as organic solar cell and touch screens, which need transparent conducting electrodes component. Five years later, Jeong Ho Cho *et al* [75] introduced and successfully fabricated flexible and transparent metallic grid electrodes via flow-coating by directly patterning silver nanoparticles (AgNPs). During the patterning with different solution concentration (1-10 mg/ml), the width of lines obviously increases with higher concentration solution. In the electrode characterization measurement, the wires are patterned from concentrations below 5 mg/ml have no conductive due to wire discontinuing. While the wire resistivity decreased as the concentration of AgNPs in solution increased until exceeding 7 mg/ml, some of the unwanted clusters are formed in patterning procedure. Therefore, from their experiment, we could conclude that the solution concentration is another critical point that has to be considered in patterning procedure.

2.6.2.2 The limitations of the "coffee stain" effect in application

Actually, the "coffee-stain" effect is a ubiquitous presence in our life. This phenomenon can often be a nuisance, or indeed a bottleneck in many industrial applications such as microelectronics [78], ink-jet printing [79] and bioassays [80]. The reason for this is that once a "coffee-stain" geometry is formed, all materials become a circle, creating a heterogeneous pattern. This material ring distribution is very difficult in applications, in particular when using ink-jet printing for integrated circuits. This technique can print materials, such as organic polymer semiconductors, dielectric materials, and even electrodes, thereby dramatically lowering the cost of fabricating electronic devices [81]. In recent years, ink-jet printing has been widely used in organic polymer transistors. However, the "coffee stain" effect seriously affects the printed material morphology. In addition, for organic light emitting diodes (OLEDs) using this technique, to deposit a smooth and uniform film is paramount for achieving uniform emission. In the fields of bioassay and chemistry, this effect is also a significant, high-impact factor. It can be seen that the act of concentrating samples by evaporation will result in material distribution. This would cause huge problems for biologists and chemists since the majority of the concentration area could not be confirmed and analyzed.

For all of these reasons, it is stressed that “coffee-stain” should be suppressed and avoided. Based on this consideration, several methods have been created. Pasquali and colleagues [82] added ethanol into droplets to induce a strong recirculation in the droplet to prevent particles moving forward to the contact line, finally depositing uniformly on the substrate. Soltman and Subramanian [83] demonstrated how the coffee ring effect can be eliminated by temperature control. Mugele et al. [84] applied an AC voltage between an electro-wetting droplet and the ITO substrate, by adjusting the AC frequency magnitude to keep the contact line continuously moving, and not pinned on the substrate. All of these methods demonstrate that the coffee-stain can be eliminated by drying the sessile droplet. The problem of adding chemicals in the liquid may potentially affect the properties of the materials and result in bioassay inaccuracy. Electrowetting is a simple, common and direct way for the droplet to be placed on the hydrophobic dielectric layer [84], meaning that an additional layer has to be added if electrodes have hydrophilic behaviour. Whether the device performance is affected by it or not is a question. The Yodh group [85] proved that changing the shape of the suspended particles inside the droplet can be used to clear the “coffee stain” effect. It shows a way by which using the particle’s very nature, clearing this effect is possible.

In short, there are many who are trying to find a suitable technique for achieving the best possible result. However, if we reverse think about this phenomenon, it can potentially be manipulated to do something useful, an idea which will be explored in Chapter 4.

Reference

1 Heeger, A. J., MacDiarmid, A. G. & Shirakawa, H. The Nobel Prize in Chemistry. *The Royal Swedish Academy of Sciences*, (2000).

2 Dodabalapur, A. Organic light emitting diodes. *Solid State Communications* **102**, 259-267, (1997).

3 Horowitz, G. Organic field-effect transistors. *Advanced Materials* **10**, 365-377, (1998).

4 Lüssem, B., Riede, M. & Leo, K. Doping of organic semiconductors. *physica status solidi (a)* **210**, 9-43, (2013).

5 Dong, H., Fu, X., Liu, J., Wang, Z. & Hu, W. 25th Anniversary Article: Key Points for High-Mobility Organic Field-Effect Transistors. *Advanced Materials* **25**, 6158-6183, (2013).

6 Coropceanu, V. *et al.* Charge transport in organic semiconductors. *Chemical reviews* **107**, 926-952, (2007).

7 Mozafari, E. & Stafström, S. Polaron dynamics in a two-dimensional Holstein-Peierls system. *The Journal of chemical physics* **138**, 184104, (2013).

8 Horowitz, G., Hajlaoui, R., Bouchriha, H., Bourguiga, R. & Hajlaoui, M. The concept of "threshold voltage" in organic field-effect transistors. *Advanced Materials* **10**, 923-+, (1998).

9 Tsumura, A., Koezuka, H. & Ando, T. Macromolecular electronic device: Field-effect transistor with a polythiophene thin film. *Applied Physics Letters* **49**, 1210, (1986).

10 Heeney, M., Zhang, W., Duffy, W., Mcculloch, I. & Koller, G. (Google Patents, 2008).

11 Sirringhaus, H. *et al.* Two-dimensional charge transport in self-organized, high-mobility conjugated polymers. *Nature* **401**, 685-688, (1999).

12 Salleo, A. Charge transport in polymeric transistors. *Materials Today* **10**, 38-45, (2007).

13 Ong, B. S., Wu, Y., Liu, P. & Gardner, S. High-performance semiconducting polythiophenes for organic thin-film transistors. *J Am Chem Soc* **126**, 3378-3379, (2004).

14 Wu, Y., Ong, B. S. & Liu, P. (Google Patents, 2009).

15 McCulloch, I. *et al.* Liquid-crystalline semiconducting polymers with high charge-carrier mobility. *Nat Mater* **5**, 328-333, (2006).

16 Klauk, H. Organic thin-film transistors. *Chemical Society Reviews* **39**, 2643-2666, (2010).

17 Peterson, J. J., Werre, M., Simon, Y. C., Coughlin, E. B. & Carter, K. R. Carborane-containing polyfluorene: o-carborane in the main chain. *Macromolecules* **42**, 8594-8598, (2009).

18 Grell, M. *et al.* Monodomain alignment of thermotropic fluorene copolymers. *Liquid Crystals* **26**, 1403-1407, (1999).

19 Sirringhaus, H. *et al.* Mobility enhancement in conjugated polymer field-effect transistors through chain alignment in a liquid-crystalline phase. *Applied Physics Letters* **77**, 406, (2000).

20 Lim, E. *et al.* Thin-film morphologies and solution-processable field-effect transistor behavior of a fluorene-thieno[3,2-b]thiophene-based conjugated copolymer. *Macromolecules* **38**, 4531-4535, (2005).

21 Lim, E., Jung, B. J. & Shim, H. K. Synthesis and characterization of a new light-emitting fluorene-thieno[3,2-b]thiophene-based conjugated copolymer. *Macromolecules* **36**, 4288-4293, (2003).

22 Babel, A. & Jenekhe, S. A. Electron transport in thin-film transistors from an n-type conjugated polymer. *Advanced Materials* **14**, 371-374, (2002).

23 Chen, X. L. *et al.* Ion-modulated ambipolar electrical conduction in thin-film transistors based on amorphous conjugated polymers. *Applied Physics Letters* **78**, 228, (2001).

24 Zhan, X. W. *et al.* A high-mobility electron-transport polymer with broad absorption and its use in field-effect transistors and all-polymer solar cells. *Journal of the American Chemical Society* **129**, 7246-+, (2007).

25 Chen, Z., Zheng, Y., Yan, H. & Facchetti, A. Naphthalenedicarboximide- vs perylenedicarboximide-based copolymers. Synthesis and semiconducting properties in bottom-gate N-channel organic transistors. *J Am Chem Soc* **131**, 8-9, (2009).

26 Yan, H. *et al.* A high-mobility electron-transporting polymer for printed transistors. *Nature* **457**, 679-686, (2009).

27 Kelley, T. W., Muyres, D. V., Baude, P. F., Smith, T. P. & Jones, T. D. in *MRS Proceedings.* L6. 5 (Cambridge Univ Press).

28 Jurchescu, O. D., Popinciuc, M., van Wees, B. J. & Palstra, T. T. M. Interface-Controlled, High-Mobility Organic Transistors. *Advanced Materials* **19**, 688-692, (2007).

29 Aleshin, A. N., Lee, J. Y., Chu, S. W., Kim, J. S. & Park, Y. W. Mobility studies of field-effect transistor structures based on anthracene single crystals. *Applied Physics Letters* **84**, 5383, (2004).

30 Gundlach, D. J., Nichols, J. A., Zhou, L. & Jackson, T. N. Thin-film transistors based on well-ordered thermally evaporated naphthacene films. *Applied Physics Letters* **80**, 2925, (2002).

31 Goldmann, C. *et al.* Hole mobility in organic single crystals measured by a “flip-crystal” field-effect technique. *Journal of Applied Physics* **96**, 2080, (2004).

32 Jurchescu, O. D., Baas, J. & Palstra, T. T. M. Effect of impurities on the mobility of single crystal pentacene. *Applied Physics Letters* **84**, 3061, (2004).

33 Anthony, J. E., Eaton, D. L. & Parkin, S. R. A road map to stable, soluble, easily crystallized pentacene derivatives. *Org Lett* **4**, 15-18, (2002).

34 Sheraw, C. D., Jackson, T. N., Eaton, D. L. & Anthony, J. E. Functionalized pentacene active layer organic thin-film transistors. *Advanced Materials* **15**, 2009-2011, (2003).

35 Lu, G. *et al.* A new class of rare earth tetrapyrrole sandwich complexes containing corrole and phthalocyanine macrocycles: synthesis, physicochemical characterization and X-ray analysis. *Chem Commun (Camb)* **51**, 2411-2413, (2015).

36 Bao, Z., Lovinger, A. J. & Dodabalapur, A. Organic field-effect transistors with high mobility based on copper phthalocyanine. *Applied Physics Letters* **69**, 3066, (1996).

37 Zeis, R., Siegrist, T. & Kloc, C. Single-crystal field-effect transistors based on copper phthalocyanine. *Applied Physics Letters* **86**, 022103, (2005).

38 Paolesse, R., Nardis, S., Sagone, F. & Khoury, R. G. Synthesis and functionalization of meso-aryl-substituted corroles. *J Org Chem* **66**, 550-556, (2001).

39 Shanmugathasan, S., Edwards, C. & Boyle, R. W. Advances in modern synthetic porphyrin chemistry. *Tetrahedron* **56**, 1025-1046, (2000).

40 Carvalho, C. M., Brocksom, T. J. & de Oliveira, K. T. Tetrabenzoporphyrins: synthetic developments and applications. *Chem Soc Rev* **42**, 3302-3317, (2013).

41 Checcoli, P. *et al.* Tetra-phenyl porphyrin based thin film transistors. *Synthetic Metals* **138**, 261-266, (2003).

42 Jeong, S. D. *et al.* Method for synthesis of tetrabenzoporphyrin precursor for use in organic electronic devices. *J Org Chem* **77**, 8329-8331, (2012).

43 Li, S., Zhao, S. & Chu, D. Crystallization of solution processable amorphous tetrabenzoporphyrin films. *Thin Solid Films* **590**, 49-53, (2015).

44 Bao, Z. A., Lovinger, A. J. & Brown, J. New air-stable n-channel organic thin film transistors. *Journal of the American Chemical Society* **120**, 207-208, (1998).

45 Sakamoto, Y. *et al.* Perfluoropentacene: high-performance p-n junctions and complementary circuits with pentacene. *J Am Chem Soc* **126**, 8138-8140, (2004).

46 Tang, Q., Li, H., Liu, Y. & Hu, W. High-performance air-stable n-type transistors with an asymmetrical device configuration based on organic single-crystalline submicrometer/nanometer ribbons. *J Am Chem Soc* **128**, 14634-14639, (2006).

47 Holliday, S., Donaghey, J. E. & McCulloch, I. Advances in Charge Carrier Mobilities of Semiconducting Polymers Used in Organic Transistors. *Chemistry of Materials* **26**, 647-663, (2014).

48 Newman, C. R. *et al.* Introduction to organic thin film transistors and design of n-channel organic semiconductors. *Chemistry of Materials* **16**, 4436-4451, (2004).

49 Kumar, B., Kaushik, B. K. & Negi, Y. S. Organic Thin Film Transistors: Structures, Models, Materials, Fabrication, and Applications: A Review. *Polymer Reviews* **54**, 33-111, (2014).

50 Cosseddu, P. & Bonfiglio, A. A comparison between bottom contact and top contact all organic field effect transistors assembled by soft lithography. *Thin Solid Films* **515**, 7551-7555, (2007).

51 Groenendaal, B. L., Jonas, F., Freitag, D., Pielartzik, H. & Reynolds, J. R. Poly(3,4-ethylenedioxythiophene) and its derivatives: Past, present, and future. *Advanced Materials* **12**, 481-494, (2000).

52 Jonas, F. & Schrader, L. Conductive Modifications of Polymers with Polypyrroles and Polythiophenes. *Synthetic Metals* **41**, 831-836, (1991).

53 Heywang, G. & Jonas, F. Poly(Alkylenedioxythiophene)S - New, Very Stable Conducting Polymers. *Advanced Materials* **4**, 116-118, (1992).

54 Winter, I., Reese, C., Hormes, J., Heywang, G. & Jonas, F. The Thermal Aging of Poly(3,4-Ethylenedioxythiophene) - an Investigation by X-Ray-

Absorption and X-Ray Photoelectron-Spectroscopy. *Chem Phys* **194**, 207-213, (1995).

55 Greczynski, G. *et al.* Photoelectron spectroscopy of thin films of PEDOT-PSS conjugated polymer blend: a mini-review and some new results. *J Electron Spectrosc* **121**, 1-17, (2001).

56 Nilsson, D., Kugler, T., Svensson, P. O. & Berggren, M. An all-organic sensor-transistor based on a novel electrochemical transducer concept printed electrochemical sensors on paper. *Sensor Actuat B-Chem* **86**, 193-197, (2002).

57 de Jong, M. P., van Ijzendoorn, L. J. & de Voigt, M. J. A. Stability of the interface between indium-tin-oxide and poly(3,4-ethylenedioxythiophene)/poly(styrenesulfonate) in polymer light-emitting diodes. *Applied Physics Letters* **77**, 2255, (2000).

58 Deleeuw, D. M., Kraakman, P. A., Bongaerts, P. E. G., Mutsaers, C. M. J. & Klaassen, D. B. M. Electroplating of Conductive Polymers for the Metallization of Insulators. *Synthetic Metals* **66**, 263-273, (1994).

59 Groenendaal, L., Jonas, F., Freitag, D., Pielartzik, H. & Reynolds, J. R. Poly (3, 4-ethylenedioxythiophene) and its derivatives: past, present, and future. *Advanced Materials* **12**, 481-494, (2000).

60 Bubnova, O. *et al.* Optimization of the thermoelectric Figure of merit in the conducting polymer poly(3,4-ethylenedioxythiophene). *Nat Mater* **10**, 429-433, (2011).

61 Bubnova, O. *et al.* Semi-metallic polymers. *Nat Mater* **13**, 190-194, (2014).

62 Ouyang, J. *et al.* On the mechanism of conductivity enhancement in poly(3,4-ethylenedioxythiophene):poly(styrene sulfonate) film through solvent treatment. *Polymer* **45**, 8443-8450, (2004).

63 Ahonen, H. J., Lukkari, J. & Kankare, J. n- and p-doped poly(3,4-ethylenedioxythiophene): Two electronically conducting states of the polymer. *Macromolecules* **33**, 6787-6793, (2000).

64 Touwslager, F. J., Willard, N. P. & de Leeuw, D. M. I-Line lithography of poly-(3,4-ethylenedioxythiophene) electrodes and application in all-polymer integrated circuits. *Applied Physics Letters* **81**, 4556, (2002).

65 Campana, A., Cramer, T., Simon, D. T., Berggren, M. & Biscarini, F. Electrocardiographic recording with conformable organic electrochemical transistor fabricated on resorbable bioscaffold. *Adv Mater* **26**, 3874-3878, (2014).

66 Deegan, R. D. *et al.* Capillary flow as the cause of ring stains from dried liquid drops. *Nature* **389**, 827-829, (1997).

67 Mampallil, D. Some physics inside drying droplets. *Resonance* **19**, 123-134, (2014).

68 Kralchevsky, P. A. & Nagayama, K. Capillary Forces between Colloidal Particles. *Langmuir* **10**, 23-36, (1994).

69 Marin, A. G., Gelderblom, H., Lohse, D. & Snoeijer, J. H. Order-to-disorder transition in ring-shaped colloidal stains. *Phys Rev Lett* **107**, 085502, (2011).

70 Hu, H. & Larson, R. G. Marangoni effect reverses coffee-ring depositions. *J Phys Chem B* **110**, 7090-7094, (2006).

71 Kim, Y. H. *et al.* Highly conductive PEDOT: PSS electrode with optimized solvent and thermal post-treatment for ITO-free organic solar cells. *Advanced Functional Materials* **21**, 1076-1081, (2011).

72 Tseng, S.-F., Hsiao, W.-T., Huang, K.-C. & Chiang, D. Electrode patterning on PEDOT: PSS thin films by pulsed ultraviolet laser for touch panel screens. *Applied Physics A* **112**, 41-47, (2013).

73 De Jong, M., Van Ijzendoorn, L. & De Voigt, M. Stability of the interface between indium-tin-oxide and poly (3, 4-ethylenedioxythiophene)/poly (styrenesulfonate) in polymer light-emitting diodes. *Applied Physics Letters* **77**, 2255-2257, (2000).

74 Kim, H. S., Lee, C. H., Sudeep, P., Emrick, T. & Crosby, A. J. Nanoparticle stripes, grids, and ribbons produced by flow coating. *Advanced Materials* **22**, 4600-4604, (2010).

75 Park, J. H. *et al.* Metallic Grid Electrode Fabricated via Flow Coating for High-Performance Flexible Piezoelectric Nanogenerators. *The Journal of Physical Chemistry C* **119**, 7802-7808, (2015).

76 Perl, A., Reinhoudt, D. N. & Huskens, J. Microcontact Printing: Limitations and Achievements. *Advanced Materials* **21**, 2257-2268, (2009).

77 Farcau, C., Moreira, H., Viallet, B. t., Grisolia, J. & Ressier, L. Tunable conductive nanoparticle wire arrays fabricated by convective self-assembly on nonpatterned substrates. *ACS nano* **4**, 7275-7282, (2010).

78 Shen, X., Ho, C.-M. & Wong, T.-S. Minimal size of coffee ring structure. *The Journal of Physical Chemistry B* **114**, 5269-5274, (2010).

79 Soltman, D. & Subramanian, V. Inkjet-printed line morphologies and temperature control of the coffee ring effect. *Langmuir* **24**, 2224-2231, (2008).

80 Eral, H. B., van den Ende, D. & Mugele, F. Say goodbye to coffee stains. *Physics world* **25**, 33, (2012).

81 Sirringhaus, H. *et al.* High-resolution inkjet printing of all-polymer transistor circuits. *Science* **290**, 2123-2126, (2000).

82 Majumder, M. *et al.* Overcoming the "coffee-stain" effect by compositional Marangoni-flow-assisted drop-drying. *J Phys Chem B* **116**, 6536-6542, (2012).

83 Soltman, D. & Subramanian, V. Inkjet-printed line morphologies and temperature control of the coffee ring effect. *Langmuir* **24**, 2224-2231, (2008).

84 Eral, H. B., Augustine, D. M., Duits, M. H. G. & Mugele, F. Suppressing the coffee stain effect: how to control colloidal self-assembly in evaporating drops using electrowetting. *Soft Matter* **7**, 4954, (2011).

85 Yunker, P. J., Still, T., Lohr, M. A. & Yodh, A. G. Suppression of the coffee-ring effect by shape-dependent capillary interactions. *Nature* **476**, 308-311, (2011).

Chapter 3

The experimental instruments and techniques

3.1 Introduction

Due to the development of equipment fabrication and technologies in modern manufacturing industries, the size of electronic components is much smaller than compared to 50 years ago. As of 2016, the most advanced chip manufacturer in the world, Intel, has placed around 7.2 billion transistors on a $456\mathrm{mm}^2$ chip [1]. This astonishing achievement has necessitated a series of mature fabrication techniques, some of which will be examined in this chapter.

3.2 Cleanroom fabrication facilities

All electronic component fabrication must be done in a cleanroom in order to avoid any contamination, for example dust dropping, which might occur during the production process. Depending on the requirements, a cleanroom can have different levels of cleanliness and equipment. The cleanroom at the University of York is level 100.

3.2.1 The optical lithography

Optical lithography or photolithography is the central method found in the modern semiconductor industry. Engineers are continuously trying to pattern as many transistors as possible on a small chip so as to enhance CPU processing and computing speed. Therefore, a higher resolution in the exposure process is always required. In fact, this technology has gradually improved over the past three decades; indeed, in just the last year exposure size went from sub-100nm to 14nm. Two key parameters determine the quality of photolithography, namely the light wavelength (λ) and numerical aperture (NA). In most cases the common light source is ultraviolet (UV). The relationship between the resolution and these two parameters can be expressed by

$$\mathrm{CD} = \mathrm{k}_1 \frac{\lambda}{\mathrm{NA}} \tag{4}$$

where CD is the critical dimension, namely the minimum feature size, and k_1 is a coefficient. As such, the resolution is proportional to the λ/NA ratio. There are two ways to enhance the resolution, which are to decrease the wavelength or increase the numerical aperture. Thus, extreme ultraviolet (EUV) can also be another option for illumination.

There are three different types of optical: contact, proximity and projection. This can be seen in Figure 3.1 below.

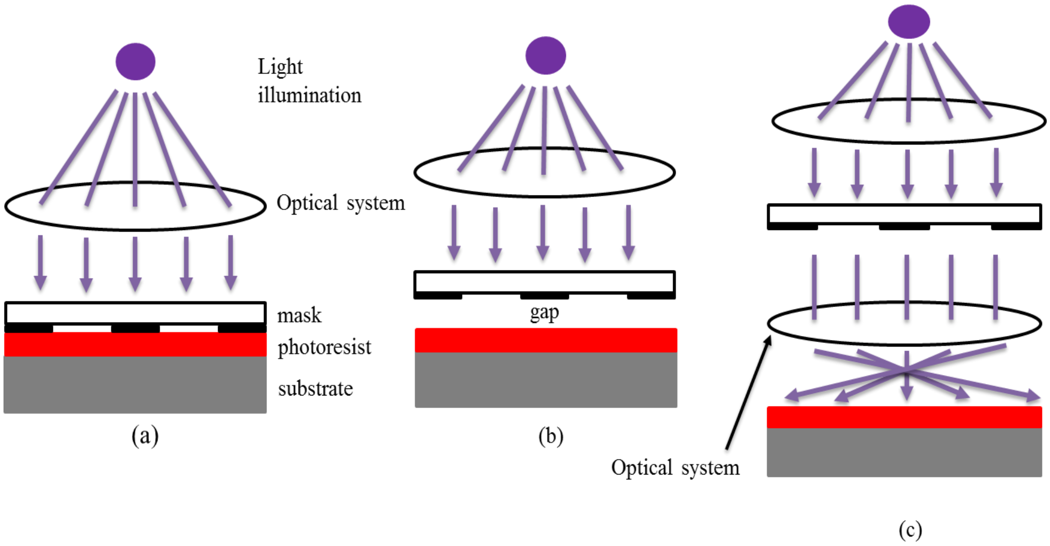

Figure 3.1 Three optical lithography modes: (a) contact mode (b) proximity mode (c) projection mode. (acquired from Ref [2])

The contact mode is liable to scrub the photoresist on the wafer, leading to an unexpected pattern defect. The proximity mode does not have this problem, but its printing resolution is lower than the contact mode because there is a vertical distance between the mask and photoresist layer. Both of these two modes have a common problem, that is, exposure area limitation. In real manufacturing industry, to realize a very-large-scale-integration (VLSI) circuit, one-time optical lithography is more than enough. The projection mode has been widely employed in the field of industry because it can cover the whole wafer, meaning that the process can be finished step by step, a process which is known as “stepper”.

Research institutions tend to choose the contact or proximity mode. This economic and efficient type is suitable for sample fabrication. The entire optical lithography process has several steps: wafer substrate preparation, photoresist coating, baking, exposure, development, dry etching (if necessary), hard baking, material deposition and lift-off. All of these steps have been comprehensively described in [3]. According to the sample geometry requirement, there are two types of photoresist, positive and negative, which lead to diametrically opposite results.

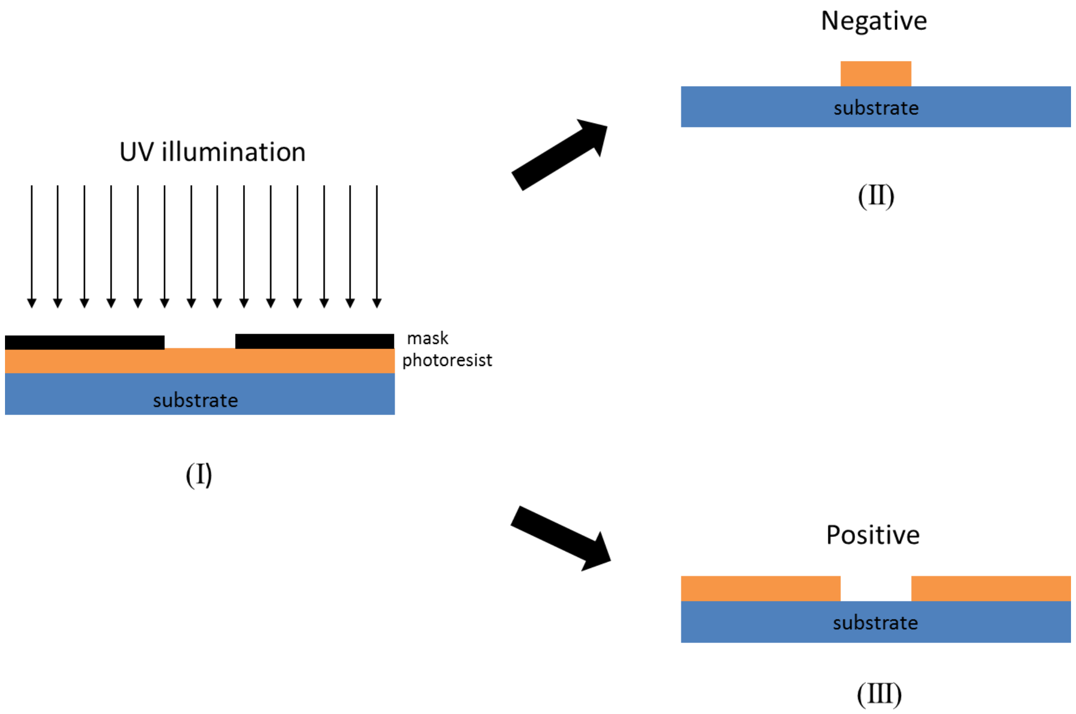

Figure 3.2 The optical lithography results are demonstrated here. (I) The substrate is fully covered by a photoresist with a mask on it. (II) After exposure to UV light, the mask covered area is made to vanish by the developer through negative photoresists (III) the mask uncovered area is made to vanish by the developer in a positive resist.

In my experiment, it was most convenient to use the positive photoresist to form a transistor channel structure. The commercial positive resist S-1813G2 developer MF-319 was used. The result is shown in Figure 3.3 below.

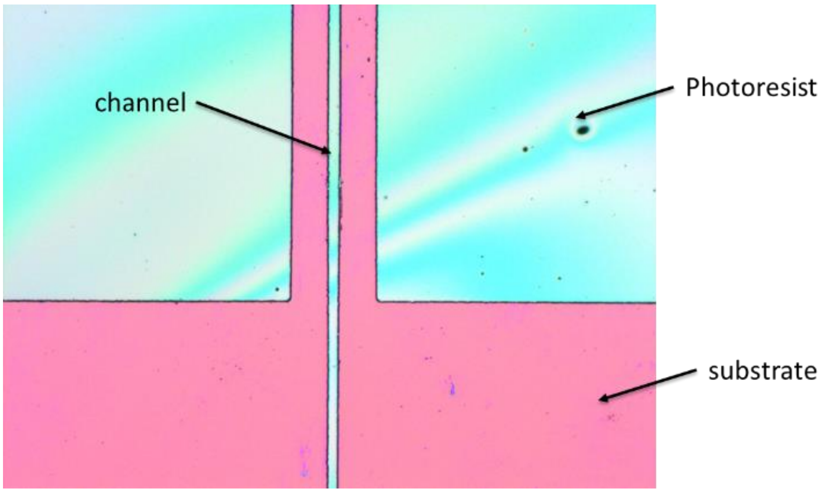

Figure 3.3 Optical lithography by using a positive photoresist to form a transistor structure.

3.2.2 Thermal evaporation

Thermal evaporation is one of the key fabrication techniques. Through this typical method, metal materials can be vaporized by heating a filament or crucible, which eventually condense on the substrate to form a thin film in a vacuum environment. The quality of the thin film depends upon the condition of a vacuum and the purity of the source material. Compared to molecular beam epitaxy (MBE) growth, the vacuum level in the thermal evaporator chamber is relatively low, a maximum of 10^{-6} torr after the oil pump has evacuated for one hour. The thickness of the thin film can be monitored using a quartz crystal with a material intrinsic parameter, such as density and z-factor, entered into the computer. There are two factors that influence the growth of the thin film. One is the material holder, where it is very difficult to deposit thick films on the substrate if a filament used for evaporation. One reason why the filament is usually a wire is that the shape limits the amount of material holding; the other reason is that once the current has been applied for a long time, it is probably blown out. However, such problems will not happen if use an evaporation boat and crucible as the materials holder. Another factor is the intrinsic property of the materials. Refractory materials require a relatively high temperature melting point and it is very difficult to acquire evaporation growth because, as the temperature increases, the vacuum level will become unstable and even decrease, leading to film deposition which is non-uniform and non-continuous. The deposition rate can be controlled by applying a current on the material holder. In order to get a high-quality thin film, the rate also has to be considered.

3.2.3 Plasma etching

Plasma etching is a kind of dry etching methodology which is quite useful in eliminating impurities and contaminations on a substrate surface. This effective technique can ensure that the substrate is completely clean in the metal electrodes deposition process. This theory has been fully described in [3]. In general, the plasma is created by using high frequency voltages (typically between kHz and MHz) to ionize a low pressure gas to create mixed chemical species, including atoms, radicals and ions [3]. In a plasma environment, the atoms in the gas are excited from their normal state to a high state in which photon emission of light occurs. This process is normally called "glow". Depending on the purpose, a single gas or even mixed gases are used in the plasma and their colours differ, with the colour of oxygen plasma, for example, being blue. As mentioned in Section 3.2.1, after the completion of the development step, some photoresist dots still stick to the exposed area, and the continuation of development will damage the structure. Thus, dry etching using oxygen plasma is an effective way of removing such organic contamination. Otherwise, as in the lift-off step, the metal electrodes will probably be peeled off by acetone. Figure 3.4 illustrates this condition.

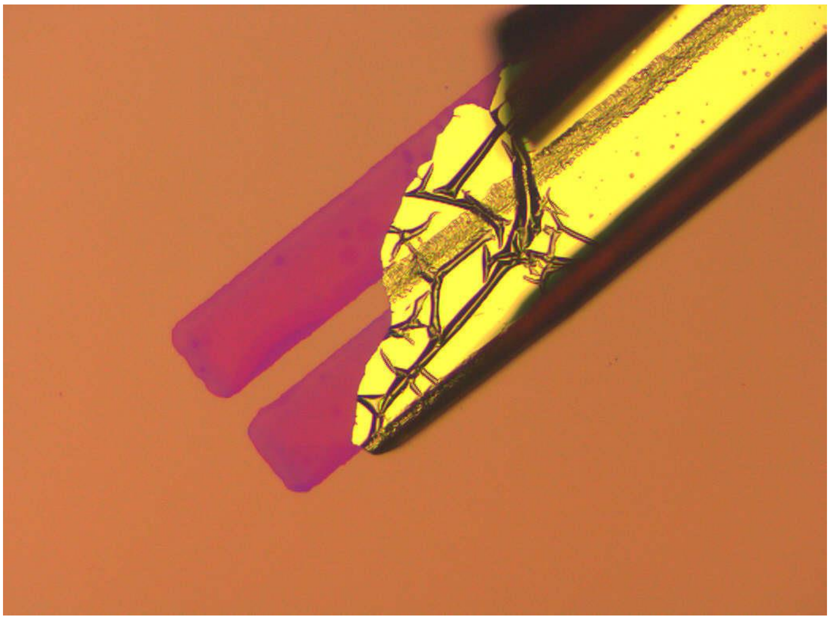

Figure 3.4 Gold electrodes peeled off in the lift-off step

Plasma etching is not only efficient in terms of substrate cleaning, but it is also central to many manufacturing processes which use silicon and other thin film devices for electronics, display or related applications [4]. In the etching process, the key point is must ensure the material which is etched area can react with plasma and form a kind of volatile compound, only in this way can avoid new compound redeposits on the material surface. Table 1 displays some commonly used elements, and the volatility of their materials and corresponding compounds.

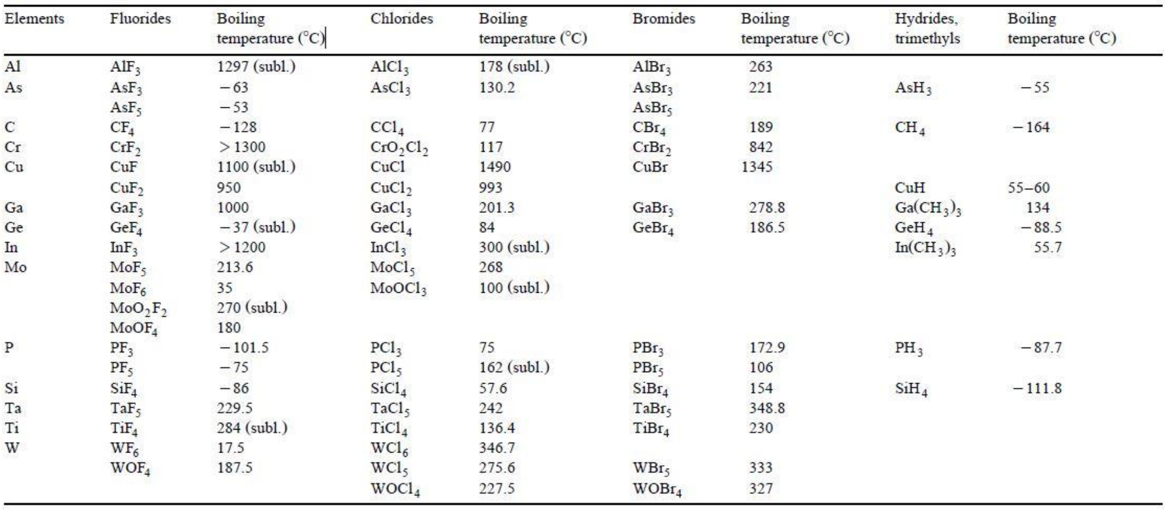

Elements	Fluorides	Boiling temperature (°C)	Chlorides	Boiling temperature (°C)	Bromides	Boiling temperature (°C)	Hydrides, trimethyls	Boiling temperature (°C)
Al	AlF_3	1297 (subl.)	$AlCl_3$	178 (subl.)	$AlBr_3$	263		
As	AsF_3	−63	$AsCl_3$	130.2	$AsBr_3$	221	AsH_3	−55
	AsF_5	−53			$AsBr_5$			
C	CF_4	−128	CCl_4	77	CBr_4	189	CH_4	−164
Cr	CrF_2	> 1300	CrO_2Cl_2	117	$CrBr_2$	842		
Cu	CuF	1100 (subl.)	CuCl	1490	CuBr	1345		
	CuF_2	950	$CuCl_2$	993			CuH	55–60
Ga	GaF_3	1000	$GaCl_3$	201.3	$GaBr_3$	278.8	$Ga(CH_3)_3$	134
Ge	GeF_4	−37 (subl.)	$GeCl_4$	84	$GeBr_4$	186.5	GeH_4	−88.5
In	InF_3	> 1200	$InCl_3$	300 (subl.)			$In(CH_3)_3$	55.7
Mo	MoF_5	213.6	$MoCl_5$	268				
	MoF_6	35	$MoOCl_3$	100 (subl.)				
	MoO_2F_2	270 (subl.)						
	$MoOF_4$	180						
P	PF_3	−101.5	PCl_3	75	PBr_3	172.9	PH_3	−87.7
	PF_5	−75	PCl_5	162 (subl.)	PBr_5	106		
Si	SiF_4	−86	$SiCl_4$	57.6	$SiBr_4$	154	SiH_4	−111.8
Ta	TaF_5	229.5	$TaCl_5$	242	$TaBr_5$	348.8		
Ti	TiF_4	284 (subl.)	$TiCl_4$	136.4	$TiBr_4$	230		
W	WF_6	17.5	WCl_6	346.7				
	WOF_4	187.5	WCl_5	275.6	WBr_5	333		
			$WOCl_4$	227.5	$WOBr_4$	327		

Table 1. Common elements and materials with halogen-, hydride-, and methyl-compound volatility. (acquired from Ref [2]).

Therefore, choosing the right gas to achieve the purpose of the etching is important. Once a non-volatile product is produced in the etching process, it can form a layer of thin film on the material surface. This unwanted compound will significantly affect the etching result.

Figure 3.5 The plasma equipment

3.2.4 Glove boxes

A glove box is a sealed container with a fully-filled inert gas (N_2) and a low moisture level constant (< 0.1ppm), providing the best environment for organic electronic sample fabrication, especially for n-type semiconductor materials. In this non-oxygen and water vapour environment, organic polymer solution preparation and deposition are carried out smoothly. Film baking is also carried out in order to avoid material oxidation when the crystallization occurs.

Figure 3.6 The glove box

3.3 Conventional transistor fabrication

In traditional OS transistor fabrication, all of the equipment previously described has to be employed. Prior to this, one important step which has to be carefully done is substrate preparation. After a SiO_2/Si wafer is cut into pieces (15mm×15mm), some particles, oil stains, and fibers always stuck on the surface. In the essential cleaning step, some chemicals can help to resolve and remove these contaminations. Usually, these substrates are initially cleaned ultrasonically in surfactant (RBS) liquid, before being cleaned by acetone and isopropanol (IPA), with deionized (DI) water being used to rinse between each step. Finally, drying using nitrogen blow and soft baking on the hotplate ensure that all water is evaporated from the substrate surface.

The following step is that of optical lithography, which produces the transistor geometry on the SiO_2/Si substrate. Spin-coating at the appropriate setting time (usually

30 seconds) and speed (3000 revolutions per minute) forms a photoresist of about 1 μm thickness. At this stage, the proximity mode is chosen. In the exposure and developing stages, time control is very important in order to avoid damaging the transistor structure. The specific parameters have been detailed in the Appendix and the optical lithography and developing steps are demonstrated in Figure 3.7. Following this, O_2 plasma is used to slightly dry clean the substrate so that we can guarantee that the metal materials can be properly deposited in order to form a channel and the electrodes.

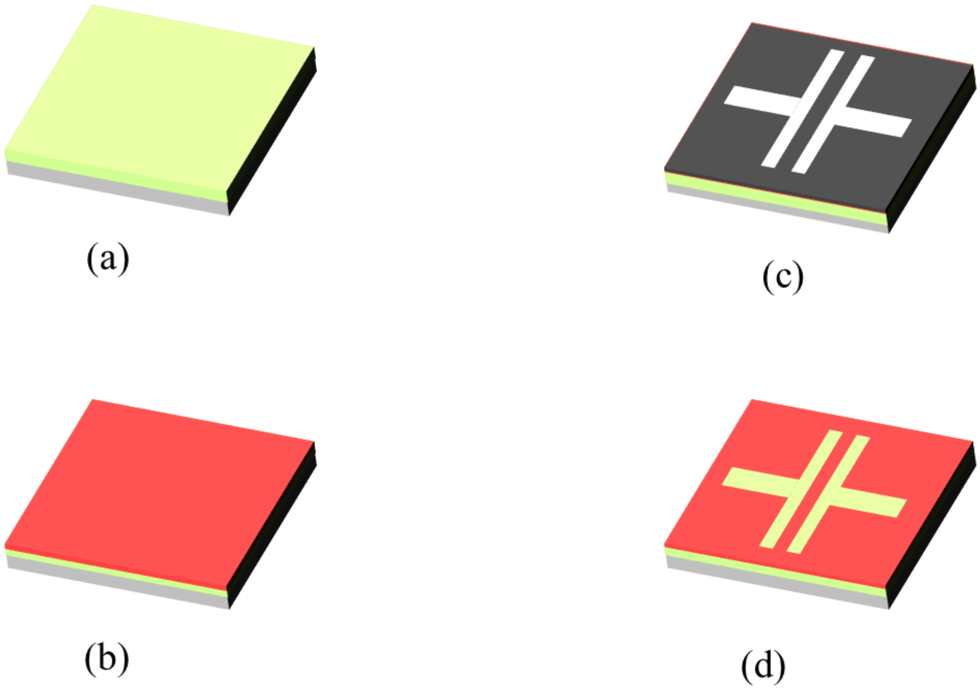

Figure 3.7 Optical lithography and developing steps: (a) SiO_2/Si substrate. (b) spin-coating photoresist (red) on substrate. (c) Mask covered on photoresist. (d) Result after exposure and development.

Generally speaking, to achieve metal evaporated deposition as a transistor's electrode, the best choice is a good work function and an air stable metal, such as gold. While, gold cannot adhere firmly to the silicon dioxide layer, chromium (Cr) or Titanium (Ti) can. Therefore, the solution is to initially deposit a very thin film (about 10 nm thickness) of Cr or Ti as a seed layer, on the substrate, as shown in Figure 3.8.

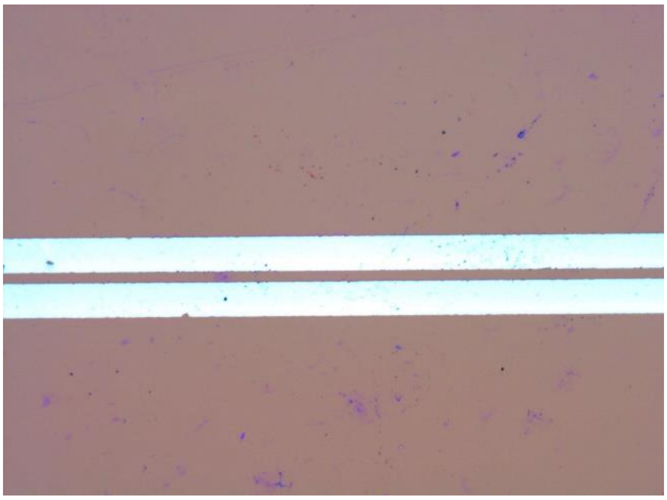

Figure 3.8. 10 nm Ti deposition on a substrate

Slowly, a uniform gold layer of about 30 nm is grown. Doing it in this way means that the gold film is firmly stuck to the electrodes, as shown in Figure 3.9.

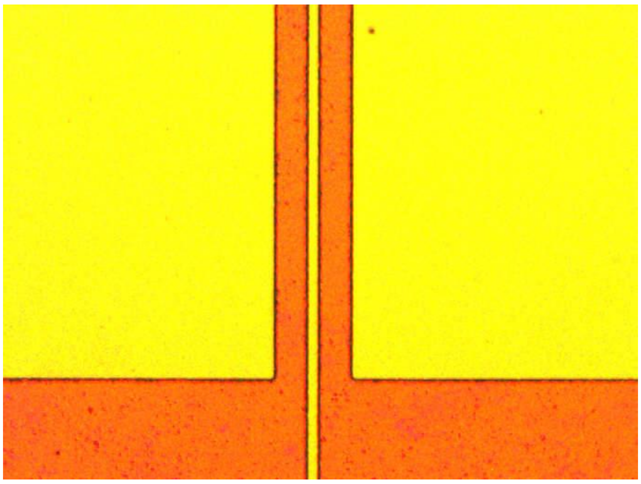

Figure 3.9. Gold electrode deposition

In order to form the transistor channel, lift-off is a crucial step after the metal evaporation. This involves putting the sample into acetone for some time, until the photoresist is totally dissolved, and then using ultrasound to gently peel off the unwanted portions. After this we then finally achieve the transistor structure.

The polymer semiconductor is prepared in a glove box, with spin-coating and baking also carried out inside it. Depending on the different materials, the baking temperature and baking time differ. When these steps are finished, a dielectric material is spin-coated onto the active layer. The final step is gate deposition on top of the dielectric layer, again in the evaporator, by using a shadow mask. The gate material is generally Aluminum (Al), because it has a low melting point and is very cheap.

All of the techniques concerning the organic semiconductor field effect transistor have now been introduced. The order in which they are done can be flexible according to the different structures.

3.4 Characterization Techniques

3.4.1 Atomic force microscopy

3.4.1.1 Working principle

Atomic force microscopy (AFM) is a surface scanning technique that can acquire a high-resolution surface nanostructure image. This image can be obtained by measuring the force on a sharp tip (whether insulating or not) which is created by the proximity to the surface of the sample. This force is kept small and at a constant level through a feedback mechanism [6]. This advanced tool has been employed in a wide range of areas, such as semiconductor science and technology, polymer chemistry and physics. Figure 3.10 shows a simplified diagram which details each component and imaging principle of AFM. During the surface characterization processing, the sample is fixed on the sample stage by a carbon sticker. Through tuning a laser beam focused onto the AFM cantilever, the light beam reflects on the photodetector. As the tip sweeps the sample surface, the height variation between them results in the deflection of the cantilever. This interaction results in the reflection of the laser spot position on the four quadrant photodetector continuously changing. Finally, the difference between these positions is captured by the photodiodes on the detector and is converted into electrical signals. The signal intensity is determined by the deflection displacement of the cantilever.

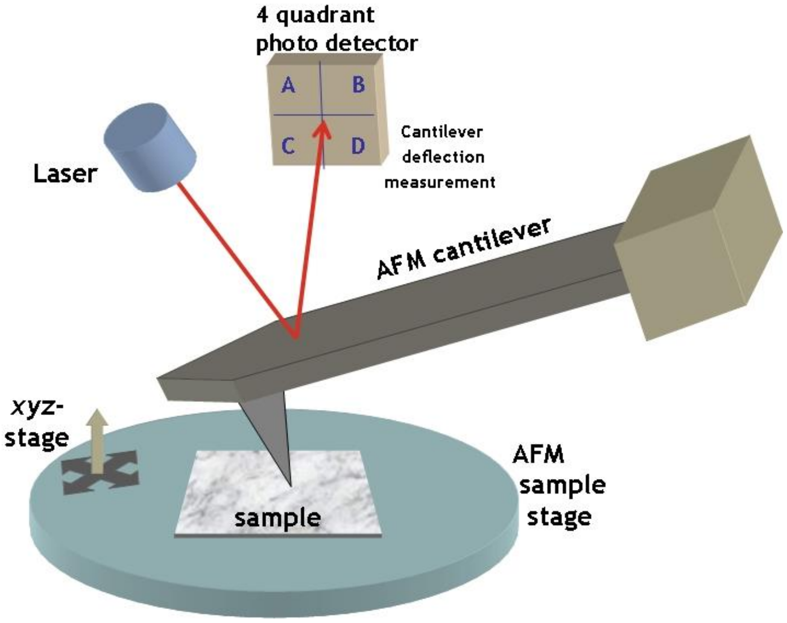

Figure 3.10. Schematic diagram of AFM
(acquired from https://commons.wikimedia.org/wiki/File%3AAFMsetup.jpg)

3.4.1.2 Working modes

According to the variation of the force of interaction between atoms (see figure 3.11), the AFM can work according to three modes: contact, intermittent contact and non-contact.

Contact mode is when the sharp tip touches the sample surface so as to obtain the profile of the structure by using the laser beam reflection displacement on the photodetector, caused by the cantilever deflection. Since the tip and specimen surface are physically in contact during the scanning motion, the interaction between them is that of a repulsive force. The the signal measurement is proportional to noise and drift, meaning that it is common to use a relatively high flexibility cantilever to increase tip sensitivity; this minimizes the effect of those factors and thus increases the signal intensity. The advantage of this mode is high image resolution due to the tip being in contact with the surface, although the downside is that it is relatively easy to cause damage to the sample and tip.

Non-contact mode is when there is tip separation from the sample surface, but the specimen surface and tip are kept in the attractive force region. In this mode, a stiffness cantilever oscillates at a given frequency, which is normally near its resonant frequency (100Hz ~ 400Hz) and where it has a small amplitude (i.e. a few nanometers). When the tip approaches the sample within a distance of between 1 nm and 10 nm, the strong Van der Waals force attracts the tip to a position that will change the cantilever oscillation frequency or amplitude, meaning that the tip-surface separation distance is also changed. The feedback control system tracks the variation, and keeps the cantilever oscillation frequency and amplitude constant by adjusting the height. Therefore, the displacement on the photodetector is not caused by cantilever deflection, but rather is based on the resonant frequency or oscillation amplitude of the cantilever.

Intermittent contact mode, also sometimes known as ***tapping mode***, is quite a popular mode because it combines the advantages of both the previously mentioned modes. Similar to the non-contact mode, the cantilever oscillates or vibrates at a given frequency but has a large amplitude (from several nanometers to 200 nm) and keeps the space between the tip and the sample surface constant so long as there is no interaction with the specimen surface. Since the tip-surface separation distance is located in the middle of the whole system, the force of interaction between the tip and surface atoms or molecules is alternately, attractive and repulsive. As the tip comes closer to the sample, the cantilever oscillation amplitude is truncated as it starts "knocking" the surface. Eventually, the feedback control system will adjust the tip and surface distance to keep the amplitude constant. The tapping mode can acquire a high lateral resolution image from a fairly rough samples, while the scanning speed is slower than in the contact mode.

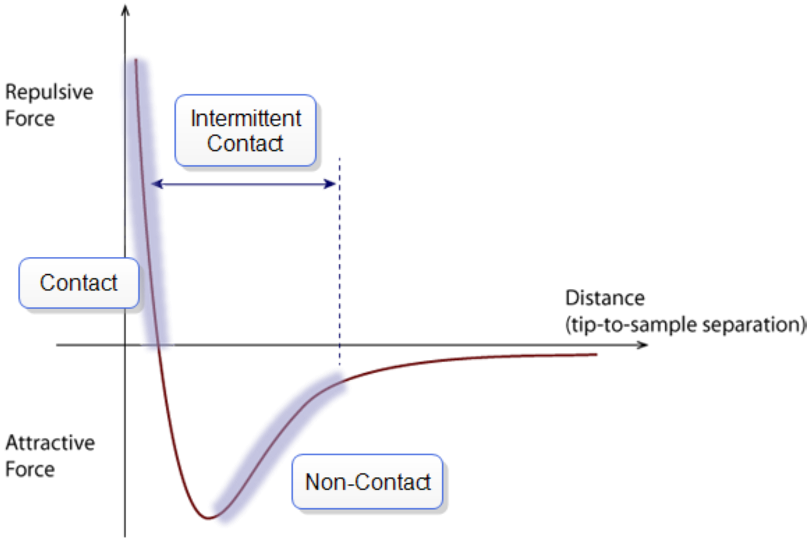

Figure 3.11. The interaction force between the tip of an AFM and the sample surface as a function of distance (acquired from http://www.nanophys.kth.se/nanophys/facilities/nfl/afm/fast-scan/bruker-help/Content/SPM%20Training%20Guide/Atomic%20Force%20Microscopy%20(AFM)/Atomic%20Force%20Microscopy%20(AFM).htm)

3.4.2 Scanning electron microscopy

The scanning electron microscope (SEM) uses a focused beam of high-energy electrons to generate a variety of signals on the surface of solid specimens. Compared to AFM, the SEM is more attractive because it can not only reveal the specimen surface features, but can also magnify the 3D image. The important part of the SEM is the electron column, which consists of an electron gun and several electron lenses and apertures. For acquiring a high resolution images, some electron source parameters, such as brightness and lifetime, combine to affect the quality of the image. The structure of an SEM is illustrated in figure 3.12 [8].

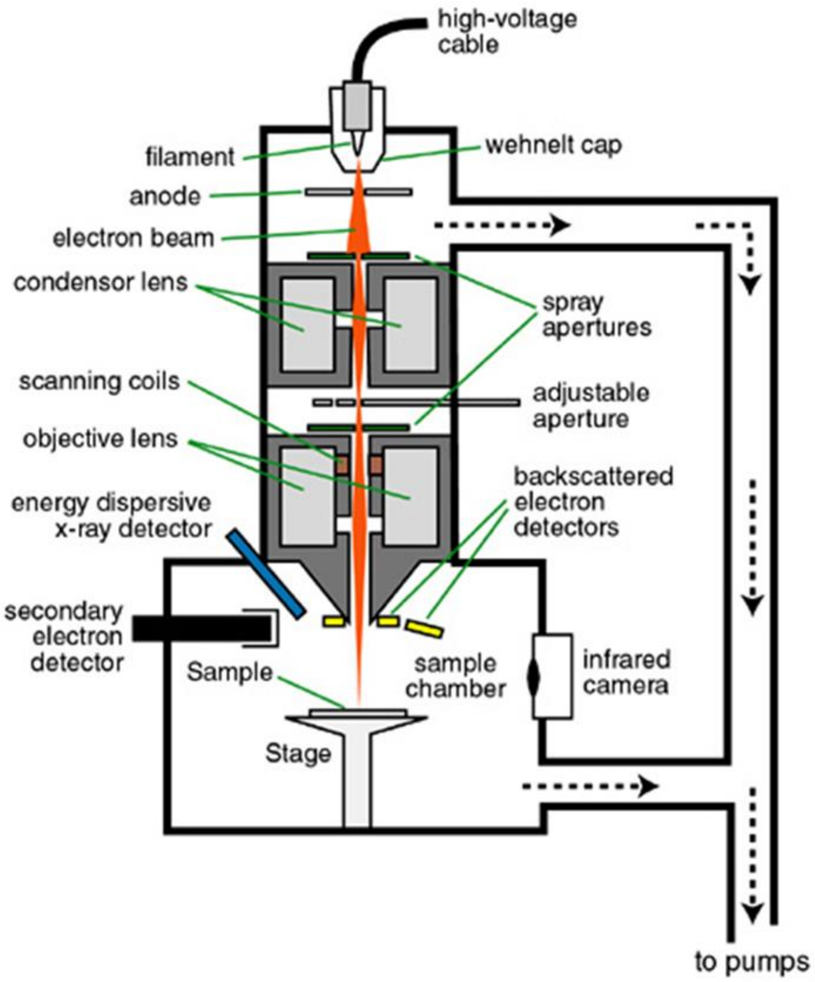

Figure 3.12. Schematic diagram of the electron column of the SEM (acquired from Ref [8])

In older SEMs, the electron beam is generated by either a tungsten hairpin filament or a lanthanum hexaboride crystal (LaB_6), with high voltages is applied to the electron gun. Only when the filament is heated to a white hot temperature, around 2700K, can it produce abundant electrons, which are emitted from the tip to form a beam current. These electrons are accelerated by the electron gun by adjusting the lens system. Eventually, they arrive in the sample vacuum chamber, and interact with the specimen located on the stage. During the beam current production process, the filament continues at an extremely high temperature, Therefore, the filament lifetime is a key point of reliability in electron beam generation. Another key parameter, the brightness, is also a crucial point in electron source performance, which can determine the image quality. Lanthanum hexaboride crystal (LaB_6) has a smaller size, and has a longer lifetime with a lower work function electron source. However, it does provide more (about 5 to 10 times more) brightness compared to tungsten, under the same conditions. In order to achieve a high quality image, some advanced electron sources, such as the field-emission gun (FEG), have been employed instead of filament or crystal.

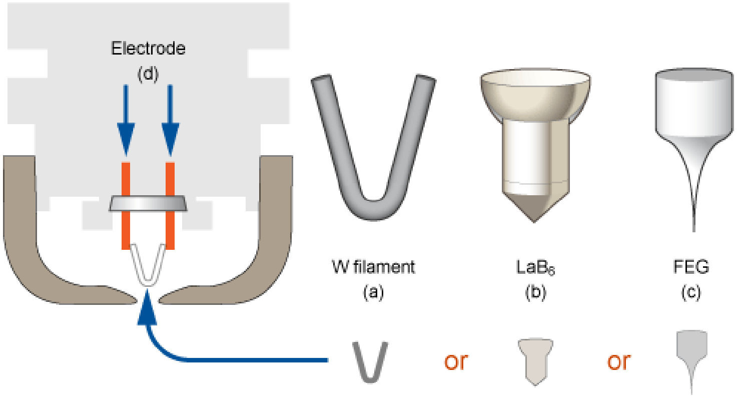

Figure 3.13 Three kinds of conventional electron emission elements with their different shapes (acquired from http://li155-94.members.linode.com/myscope/sem/practice/principles/gun.php).

The shape of these electron sources are provided above in Figure 3.13. It is clear that the FEG tip is the sharpest of all of them. This makes it easier for electrons to escape from the source. The field emission gun has two classes: the cold cathode type and the thermal (thermally assisted) Schottky field emission type. The related parameters, which compare different electron sources are displayed in Table 2.

Source	Brightness $A/cm^2 sr$	lifetime (h)	source size (nm)
Tungsten	10^5	40-100	$3 \times 10^4 - 10^5$
LaB_6	10^6	200-1000	$5 \times (10^3 - 10^4)$
Field emission			
Cold cathode	10^8	>1000	< 5
Thermal assisted	10^8	>1000	< 5
Schottky	10^8	>1000	15-30

Table 2. Comparison of different electron sources parameters at 20 eK (acquired from Ref [8])

From this table, it can be seen that the field emission electron gun can provide more brightness, has a longer lifetime as well as a smaller size of electron beam. The smaller source size means that a better electron probe can be achieved on the specimen surface, gaining a good resolution in the SEM. In my experiment, a thermal assisted Schottky field emission gun has been used to observe and measure the sample geometry. The electron emission and acceleration theory is demonstrated in Figure 3.14. The electrons are produced by a large electrical field, about $10^5$to 10^8 V/cm, between the tip and first anode (V_1). The voltage difference between the second anode and the tip (V_o) determines the acceleration of the electron beam [8].

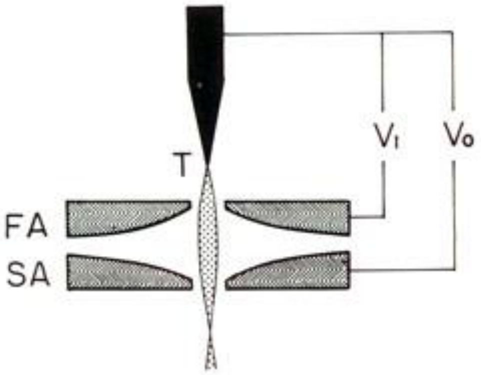

Figure 3.14 Schematic diagram of the field emission source (acquired from Ref [9])

As mentioned above, the crossover of the electron beam, which is g by FEG, through two or three lens focuses and demagnification, finally forms an electron probe of about 1 nm diameter, with its current impinging on the sample surface [9]. This probe current raster over the sample region generates several types of signals through beam-specimen interaction, which are capable of carrying information about the specimen composition, topography, local fine-scale surface texture and thickness. The major signal is caused by secondary electrons (SE) and backscattered electrons (BSE) [10].

The secondary electrons are specimen electrons, which receive enough kinetic energy from the electron beam. With inelastic collisions they are ejected from the specimen atom with energies in the range of 0 to 50 eV. These low-energy electrons are collected and accelerated by a detector which is connected to a raster scan generator, through A/D conversion to display an image on a computer monitor. This image production relies on primary beam raster scans on the sample surface. At the same time, the angle between the incident beam and sample determines the amount of secondary electrons which can escape and be captured by the detector, thereby affecting the image brightness and resolution. Secondary electrons are the main source of building the sample image in SEM.

Different to secondary electrons, the high-energy backscattered electrons come from the electron beams directly. They are reflected or back-scattered electrons which emanate from the specimen interaction volume through elastic scattering interactions with specimen atoms. The intensity of BSEs depends on the element types in the sample. Usually, heavy elements (with a high atomic number) backscatter electrons more strongly than light elements (with a low atomic number). Thus, the image contrast in this mode is clearer than in the SE mode. In addition, it can be used to study the distribution of elements in the sample.

Figure 3.15 provides an example of a cross-section of the sample which consists of the deposition of two kinds of material on a silicon wafer. The first layer is a photoresist and the second layer is PMMA. Since PMMA is an insulator material, when the electron beam focuses on the sample, the monitor display only shows the electrons drift movement on the surface, and there is no generation of SEs or BSEs. Under these conditions, the simple deposition of a thin layer (a few nanometers) of a conductive layer material, such as Au, can solve this problem. The sample is fixed by a carbon sticker onto a special sample holder (at a 45° tilt angle) and through manual adjustment of the angle of the electron it is finally brought to focus on this area.

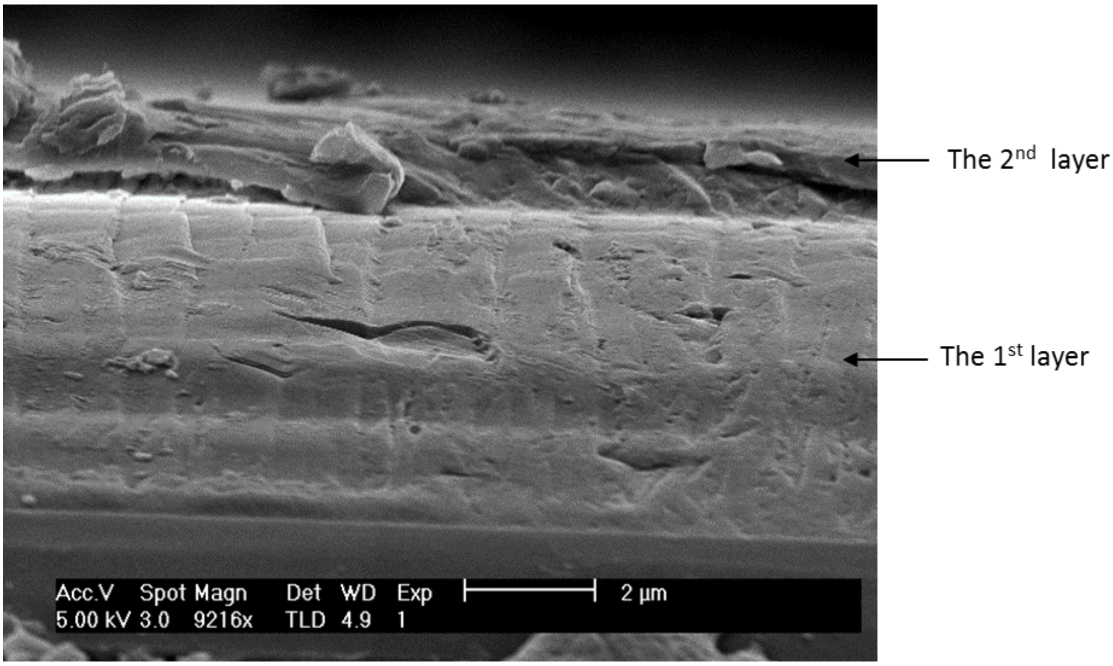

Figure 3.15. A cross-section of a sample image by SEM. The first layer is photoresist and the second layer is PMMA.

3.5 Measurement Techniques

3.5.1 Probe station

A probe station is quite useful for acquiring a signal from a semiconductor device, and it is also popular in academic research on electronics and material in science subjects. It usually contains three or four very fine conductive needles that connect to a semiconductor analyzer. In the testing procedure, taking the TGTC transistor as an example, the sample is fixed on the stage by a vacuum system, and two needles must carefully pierce the dielectric layer to rest on the source and drain electrodes, before another needed is placed on the gate. This is shown in Figure 3.16 below.

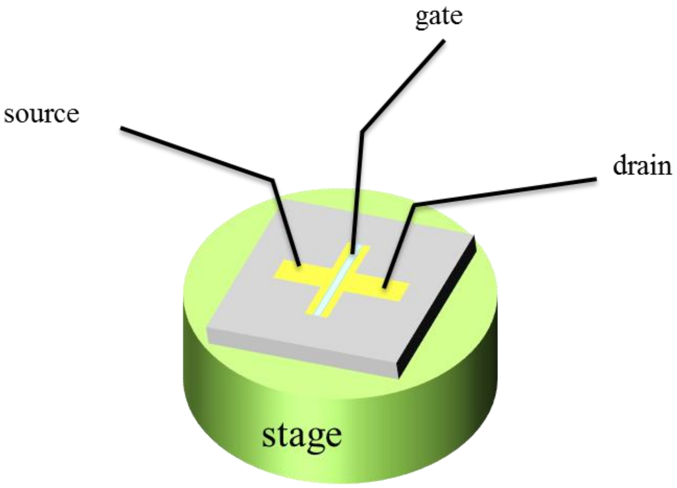

Figure 3.16 Transistor connection with a probe station

Depending on the type of semiconductor, positive or negative voltage will be applied on the gate, source and drain electrodes. According to the requirements, the probe station can also be refitted and connected to a vacuum system in a low temperature environment, providing a good environment for device measurement. Figure 3.17 illustrates the traditional whole probe station.

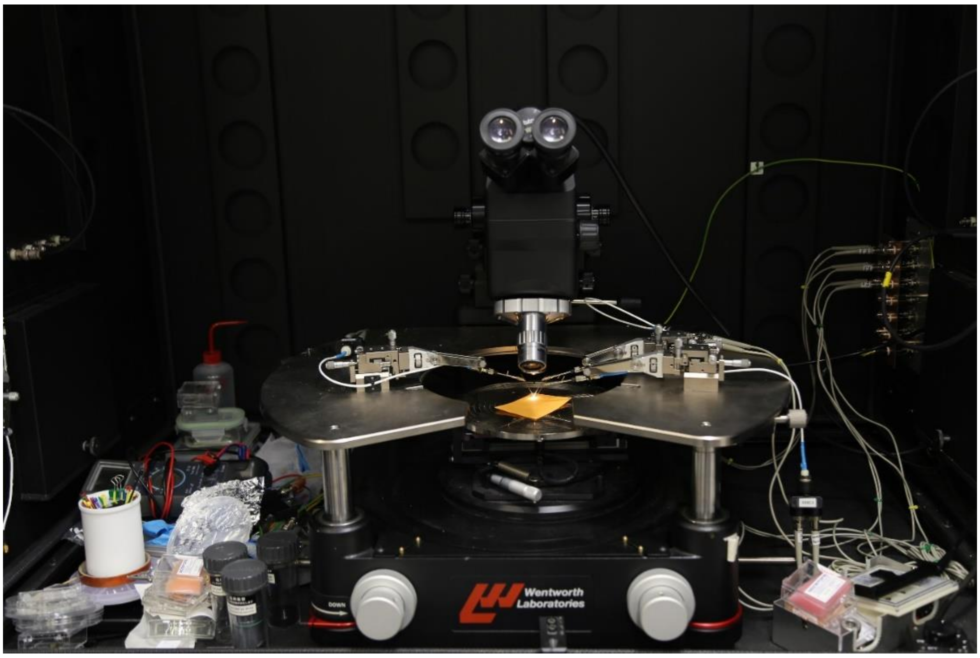

Figure 3.17 The probe station

3.5.2 Semiconductor analyzer

In my experiments, the probe station is connected to a semiconductor analyzer (Agilent 4516C) which can measure the device parameters after setting a proper voltage range between the source, drain and gate. The data can be collected and plotted on the screen.

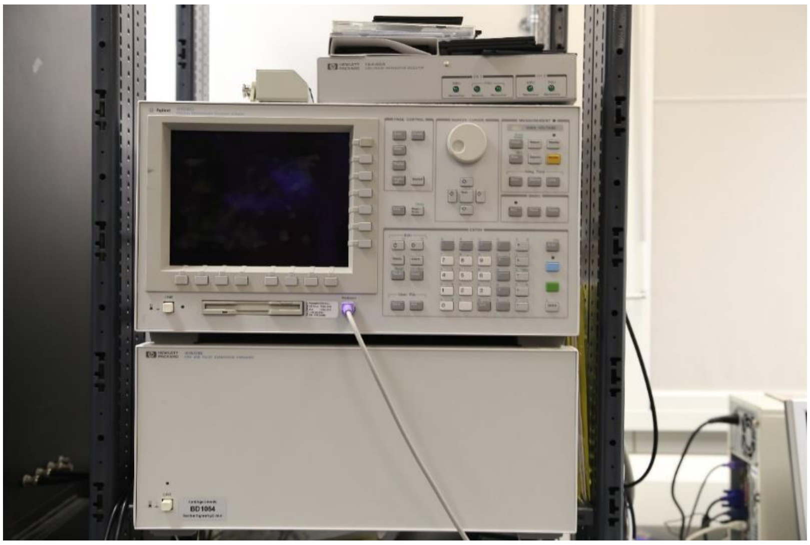

Figure 3.18 The Agilent semiconductor parameter analyzer (Agilent 4516C)

3.6 Summary

In this chapter, all the experimental instruments with their principles and operation method have been introduced. The traditional device fabrication process and techniques also have been introduced.

Reference

1 Alcorn, P. *Intel Xeon E5-2600 v4 Broadwell-EP Review*, <http://www.tomshardware.com/reviews/intel-xeon-e5-2600-v4-broadwell-ep,4514-2.html> (2016).

2 Cui, Z. *Micro-nanofabrication: technologies and applications*. (Springer, 2006).

3 Cardinaud, C., Peignon, M.-C. & Tessier, P.-Y. Plasma etching: principles, mechanisms, application to micro-and nano-technologies. *Applied Surface Science* **164**, 72-83, (2000).

4 Belkin, E. V. S. k. a. V. S. Cleaning properties of atomic oxygen excited to metastable state 2s22p4(S10). *J. APPl. Phys.*, 102, (2007).

5 Graves, D. B. & Humbird, D. Surface chemistry associated with plasma etching processes. *Applied surface science* **192**, 72-87, (2002).

6 Binnig, G., Quate, C. F. & Gerber, C. Atomic force microscope. *Physical review letters* **56**, 930, (1986).

7 *Scanning Electron Microscope overview.*, <http://nau.edu/cefns/labs/electron-microprobe/glg-510-class-notes/instrumentation/> (2016).

8 Goldstein, J. I. *et al.* in *Scanning Electron Microscopy and X-Ray Microanalysis* 21-60 (Springer, 2003).

9 Heinrich, K. F. *Electron beam X-ray microanalysis*. (Van Nostrand Reinhold Co., 1981).

Chapter 4

Patterned organic material wires

4.1 Introduction

In this chapter, the details of organic materials solution preparation for several pattern techniques will be introduced. The organic materials include both semiconductors and insulators. The pattern technique I used here take full advantage of the "coffee-stain" effect that most scientists and engineers are always trying to avoid in their experiments.

4.2 Organic materials solutions preparation

In my experiments, six organic materials and four solvents have been used; and each of these materials has their own properties, such as colour, molecular weight and solubility, etc. As I have mentioned above, solubility is an advantage for organic semiconductors in comparison with traditional semiconductors. Therefore, choosing a proper solvent to dissolve those solutes and making them form a homogeneous solution is very important for device fabrication.

4.2.1 Organic semiconductor materials solution preparation

First of all, I would like to introduce three kinds of organic semiconductor materials in my work. They are poly(3,3′′′-didodecylquaterthiophene) (PQT-12), poly(9,9-dioctylfuorene-co-dithiophene) (F8T2) and poly{[N,N′-bis(2-octyldodecyl)-1,4,5,8-naphthalenedicarboximide-2,6-diyl]-alt-5,5′-(2,2′- bithiophene) (P[NDI2OD-T2]). In the Chapter 2, the history and characteristics of them have been described.

PQT-12, a kind of dark red powder, can only be dissolved by 1’2-dichlorobenzene ($C_6H_4Cl_2$) (DBC). The chemical structure of this solvent is illustrated in Figure 4.1.

(a) **(b)**

Figure 4.1. The chemical structure of 1’2-dichlorobenzene
(a) The structural formula (b) the model of DCB
(acquired from https://en.wikipedia.org/wiki/1,2-Dichlorobenzene)

The high boiling point, about 180℃, of this solvent means that its evaporation speed is very slow. This feature is of benefit for thin film deposition during spin-coating. The PQT-12 is relatively difficult to dissolve in comparison with the other two materials. Even when totally dissolved by solvent, the solution exhibits colloidal status under a room temperature environment. Thus, before the spin-coating process, the PQT-12 solution has to be heated on a hot-plate at 50℃ until it becomes a red transparent liquid. The F8T2, also called as 2008P, is a kind of yellow, cotton-like polymer semiconductor and its corresponding solvent is Toluene (C_7H_8). See the Figure 4.2 below.

(a) (b)

Figure 4.2. The chemical structure of Toluene.
(a) The structural formula (b) the model of Toluene
(acquired from https://en.wikipedia.org/wiki/Toluene)

The F8T2 can be dissolved rapidly by this chemical, forming a light yellow transparent solution at room temperature and pressure.

The last polymer material, an n-type organic semiconductor, is P[NDI2OD-T2]. The solvent for this dark blue bulk material is the same as for PQT-12, the 1’2-dichlorobenzene.

For studying the organic small molecule crystalline orientation characteristic during the material recrystallization, the material I used in my experiment is tetrabenzoporphyrin. The solvent for this material is chloroform ($CHCl_3$). The chemical structure is shown in figure 4.3 below.

(a) (b)

Figure 4.3. The chemical structure of chloroform
(a) The structural formula (b) the model of chloroform
(acquired from https://en.wikipedia.org/wiki/Chloroform)

All of the semiconductor solution preparations are operated in a glove box in order to isolate water vapour and prevent oxygen interference. The pattern results of material with the solution concentration control will be introduced in Section 4.4.1.

4.2.2 Organic insulation materials preparation

In the OFET fabrication, the quality of the insulator layer should also be considered because the roughness of dielectric layer can affect the carrier movement on the interface between these two layers. Therefore, making the dielectric material dissolve sufficiently to increase the surface smoothness of the surface during spin-coating from solution can reduce the electron trapping probability.

The first material is named poly(4-vinylphenol) (PVP). This white powder materiel can be easily dissolved in isopropyl alcohol (IPA). The solute and solvent structural formulae are demonstrated in Figure 4.4.

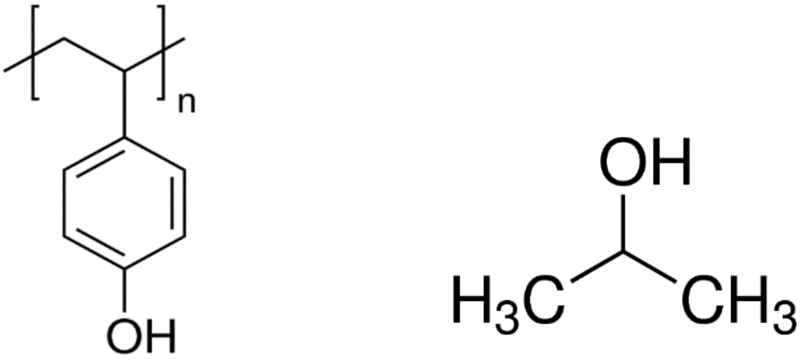

(a) (b)

Figure 4.4. The chemical structure for both of materials
(a) Poly (4-vinylphenol) (b) Isopropyl alcohol
(Both images are acquired from http://www.sigmaaldrich.com/catalog/substance/poly4vinylphenol123452497970211?lang=en&region=GB and http://www.mpbio.com/product.php?pid=02194006&country=222, respectively)

The second material is poly(methyl methacrylate) $(C_5O_2H_8)_n$ (PMMA), also known as acrylic glass material. The monomer of PMMA is the result of methacrylic acid and methanol interaction. The German chemist Wilhelm Rudolph Fittig discovered the polymerization process that turns methyl methacrylate into poly(methyl methacrylate) in 1877. Nowadays, this kind of material is used in lots of fields, such as eyeglasses, due to its good impact strength, light weight and excellent visible light transparency. In my experiment, the solvent is butyl acetate ($C_6H_{12}O_2$). Both of these organic material chemical structures are illustrated in Figure 4.5.

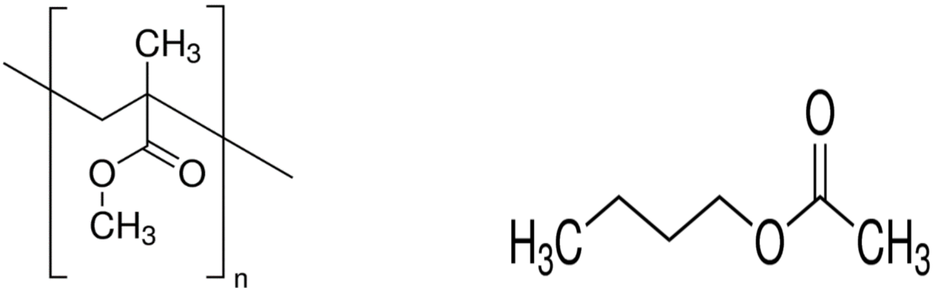

(a) (b)

Figure 4.5. The chemical structure for two kinds of materials
(a) Poly (methyl methacrylate) (b) Butyl acetate
(Both of images are acquired from http://www.sigmaaldrich.com/catalog/substance/polymethylmethacrylate12345901114711?lang=en&region=GB and http://www.sigmaaldrich.com/catalog/substance/butylacetate1161612386411?lang=en&region=GB, respectively)

The third organic material that I used in experiment is named polystyrene (PS). It is one of the most widely used materials in plastic products. The composition of polystyrene was first discovered in 1839 by Eduard Simon [1], an apothecary from Berlin. Because of the poor isolation ability of oxygen and water vapour, this material cannot be used in organic electronic device fabrication. In my experiment, it is used to study the pattern theory. The solvent for polystyrene is either DCB or toluene. The chemical structure of polystyrene can be seen in Figure 4.6.

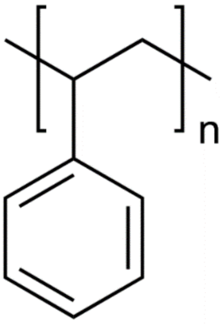

Figure 4.6. The chemical structure of polystyrene (acquired from http://www.sigmaaldrich.com/catalog/product/sial/00926?lang=en&region=GB)

In the organic pattern experiments, all of the organic semiconductor materials and PMMA have been involved in electronic device fabrication. PS and PVP are utilized to study the features of material pattern geometry in a confined structure.

4.3 The PDMS template preparation

The features of the PDMS stamp are another important factor for high-resolution patterning for solution-processable materials on a silicon wafer. The structured stamp template is made by the photo lithography technique using different widtha and separations of lines, 10μm/10μm, 20μm/20μm, and 30μm/30μm, on a photomask. The PDMS rubber stamp is then duplicated by pouring commercial silicone elastomer (Slygard@184, Dow Corning) fully stirred with its cross-linker in a 10:1 mixed ratio, to the structured stamp template. Before the annealing, the colloidal liquid must be put on a flat surface for a period of time until the air bubbles that are in the liquid disappear. The purpose is avoiding defects producing during the PDMS stamp formation. The annealing is done at 70℃ and lasts for 1 hour. This procedure has been demonstrated in Figure 4.7.

Figure 4.7. The silicone elastomer annealing on a hotplate

From this image, we can see the four structures of the templates are fixed on the bottom of a container with silicone elastomer colloidal liquid covering them. Through repeated experiments, I determined that the best amount of colloidal liquid is 20 ml in order to form about 5 mm thickness stamps which can get good patterning results.

Under this confined geometry, in the patterning process, the solvent can evaporate slowly and finally leave a structure which has been designed by photo lithography.

4.4 The theory and results of patterning organic materials

Liquid flow/drying-induced edge deposition from solution/suspension is frequently observed in our daily lives. For instance, natural levees that are formed through the deposition of sediments along flooded river banks have been utilized for settlement and agriculture since ancient civilizations and still remain interesting in modern archaeology [2] [3]. As was discussed in Chapter 1, the drying of a solution deposited on a solid surface often leaves a dense, ring-like solute deposition along the perimeter, which is known as the “coffee-stain effect.” This effect can be used to generate small features that normally require digital deposition and strict tuning of the chemical properties of both the deposited solution and the substrate surface [4] [5].

4.4.1 Patterning method

Patterning of the polymers was performed on a specially fabricated stainless steel clamping tool, which allowed proper sample/template alignment and the application of controlled pressure. The stainless tool is illustrated in Figure 4.8.

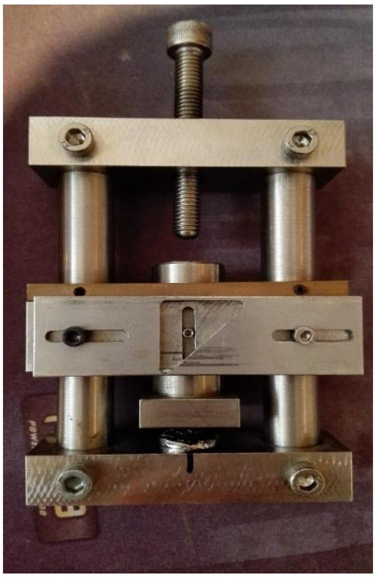

Figure 4.8. The stainless steel clamping tool

This whole patterning procedure has been shown in Figure 4.9. The polymer coated film was gently brought into contact with the solution-wetted template for about 5 seconds and was subsequently dried at room temperature for 45 min under a small applied pressure (~5 MPa). Finally, the template was removed, leaving the patterned polymer on the substrate. The idea of this work is mainly motivated by groove-pinning of a contact line theoretically proposed several decades ago for drying liquid on a grooved substrate [6] [7]. In my work the grooves are fabricated on a flexible rubber objective which can effectively guide the pattern formation on the substrate and is reusable.

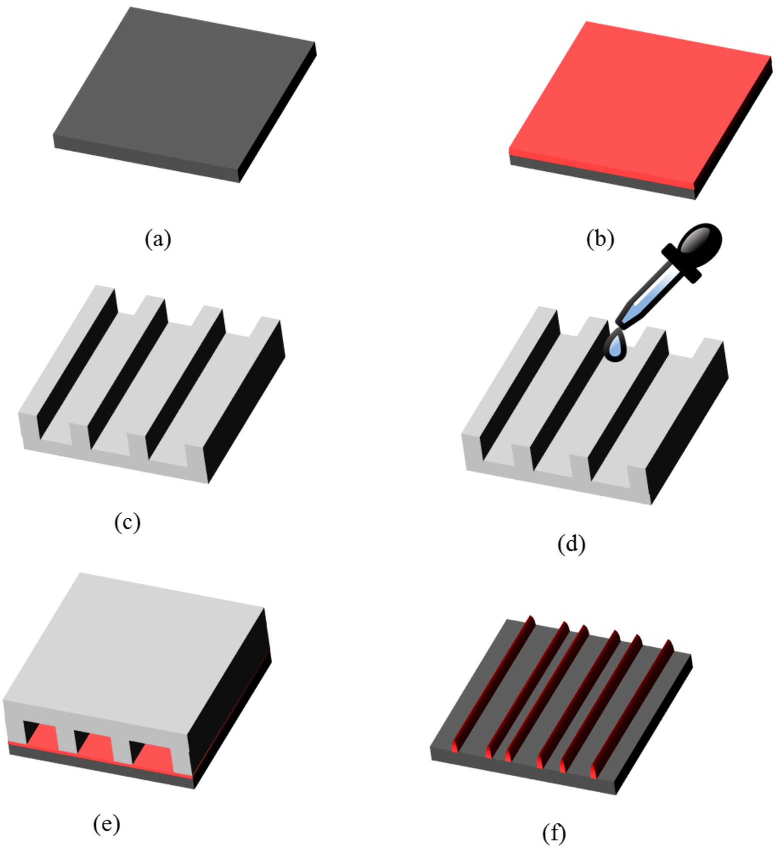

Figure 4.9. The procedure of pattern process of soluble organic material
(a) Well cleaned Silicon substrate
(b) Material deposition by spin-coating
(c) PDMS stamp preparation (d) a small drop of solvent onto the stamp
(e) Stamp presses on the thin film material with proper pressure
(f) Several lines formed after solvent evaporation

During the pattern processing, the material is spin-coated on a substrate. For getting the best pattern results, several experiments have been done attempting to get the best parameters. From Chapter 2, we have known that solution concentration decides the quality of the wire, therefore, I prepared a series of polystyrene (PS) solutions with different concentrations (0.6 mg/ml, 10 mg/ml, 30 mg/ml and 50 mg/ml) and patterned all of them by using identical PDMS stamps. All the results are displayed in Figure 4.10, from which we can easily observe that the wire size grows as the concentration is increased; when the solution concentration reached about 50 mg/ml, a separated wire array was very difficult to obtain. Furthermore, a fixed concentration of solution (2.5 mg/ml) with varied groove sizes in the PDMS stamps (2µm, 10µm, 40µm, 120µm) have also been patterned and all of the resulting images are illustrated in Figure 4.11.

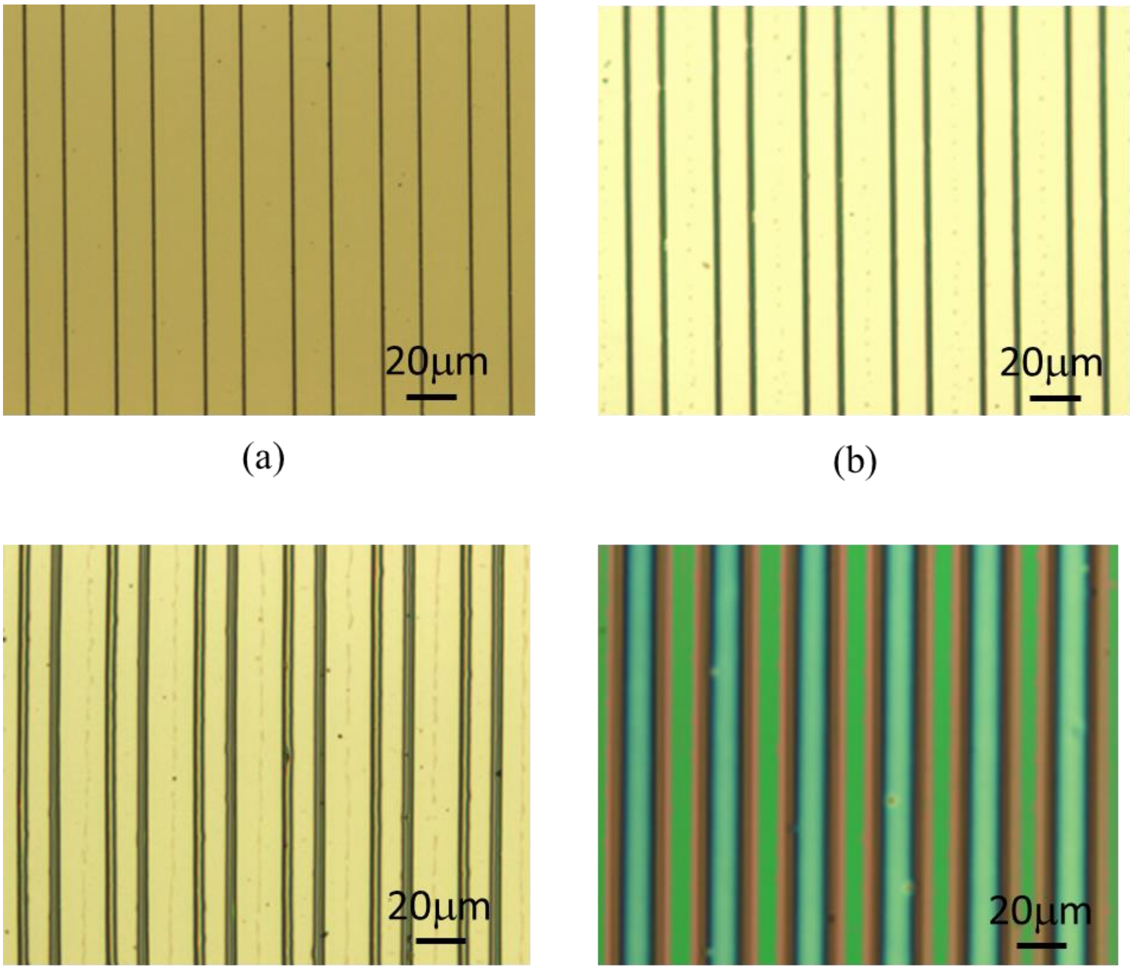

(a) (b) (c) (d)

Figure 4.10. The different concentration of PS solution patterned on silicon substrate (a) 0.6 mg/ml (b) 10 mg/ml (c) 30 mg/ml (d) 50 mg/ml

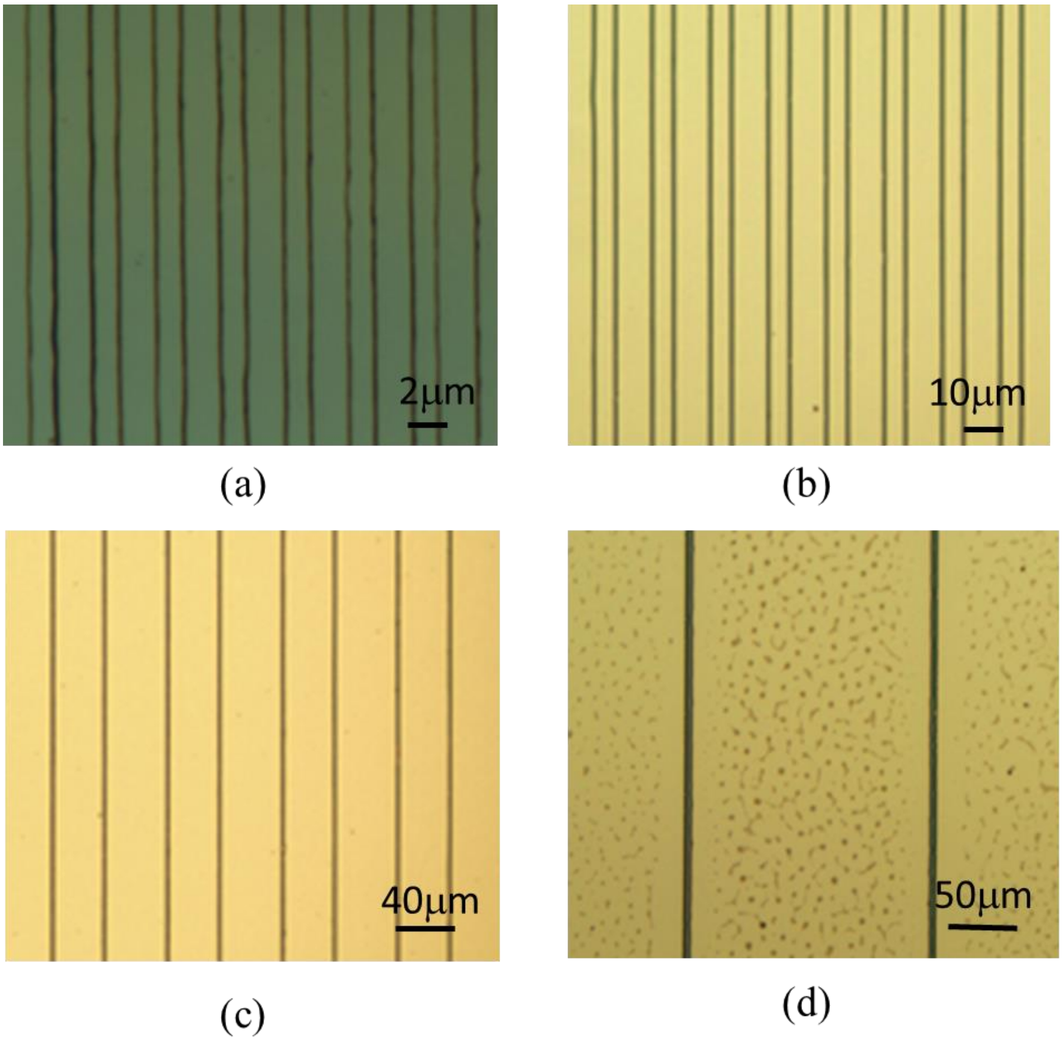

Figure 4.11. The fixed concentration of PS solution patterned wires dependent in stamp size: (a) 2μm (b) 10 μm (c) 40 μm (d) 120 μm

In order to ensure the experimental accuracy, I prepared another organic material, PVP, solution with variable concentrations (0.6 mg/ml, 10 mg/ml, 50 mg/ml and 100 mg/ml) that were then also used in patterning process. Compared to PS solution, the results were quite similar. See the Figure 4.12 below. The fixed concentration (2.5 mg/ml) with variable groove size stamps have been done as well. The Figure 4.13 demonstrates these patterning results.

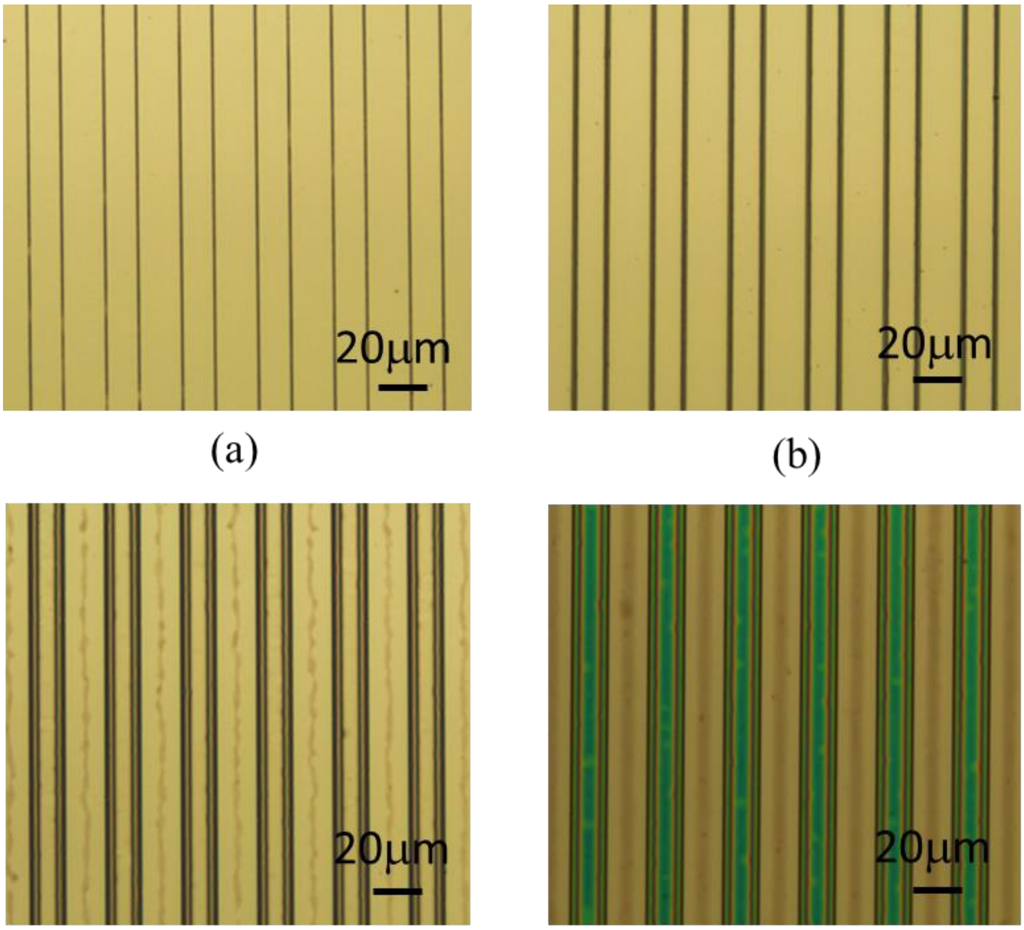

(a) (b)

(c) (b)

Figure 4.12. The different concentration of PVP dependent in IPA solution patterned wires on silicon substrate
(a) 0.6 mg/ml (b) 10 mg/ml (c) 50 mg/ml (d) 100 mg/ml

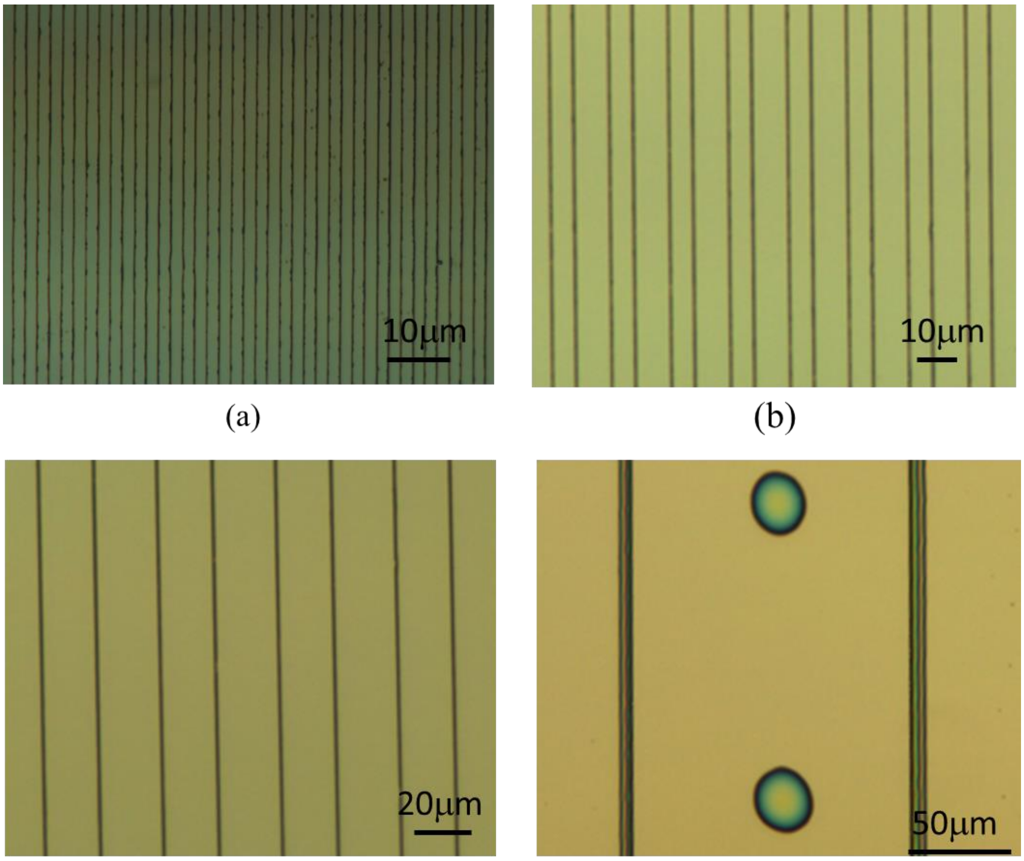

(a) (b) (c) (d)

Figure 4.13. The fixed concentration of PVP solution patterned wires dependent in stamp groove size: (a) 2.5 µm (b) 10 µm (c) 20 µm (d) 120 µm

Finally, the concentration of solution has been chosen at 6 mg/ml in order to control the thickness of film below 200 nm; the parameters of spin speed and time were set at 3000 revolutions per minute and 3 minutes, respectively. The solvent is drop-casted onto a micro-structured PDMS stamp surface with controlled volume of about 3 µl/cm^2. Figure 4.14 demonstrates a large area of PVP pattern.

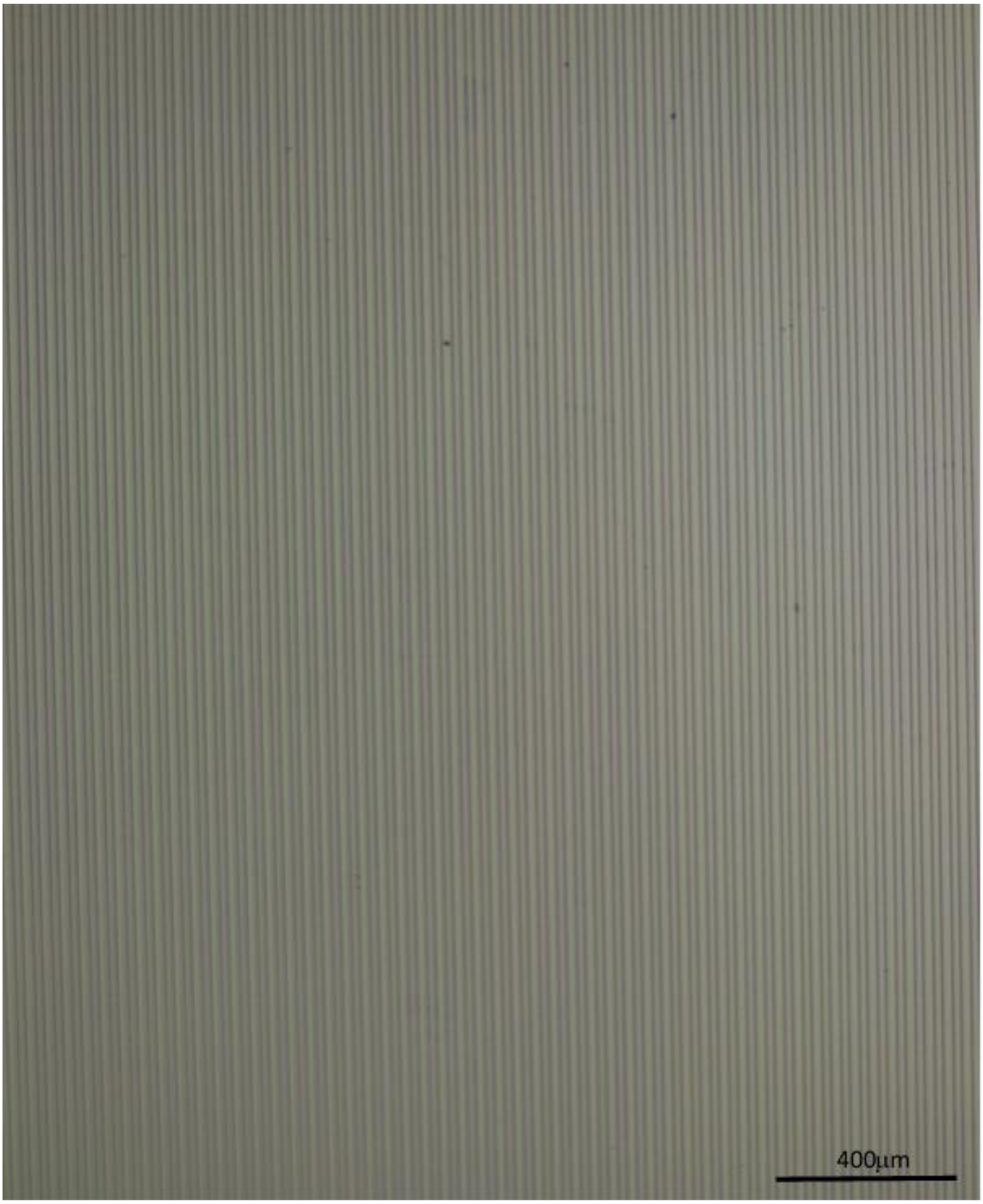

Figure 4.14. The optical image of large-area PVP wires array pattern

4.4.2 The theory of patterning

In order to understand the principles of the patterning process, two types of patterning experiment were designed which are schematically illustrated in Figure 4.15 and Figure 4.16, respectively. In the first experiment a layer of solution is introduced between a flexible micro-structured template and a substrate and is dried at an appropriate temperature.

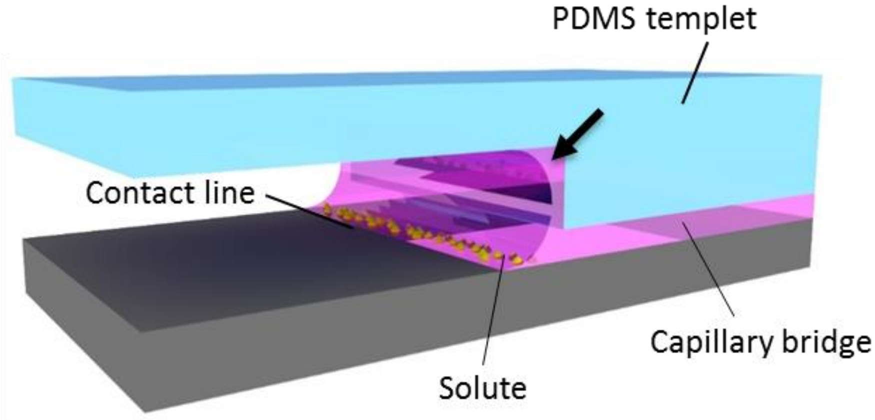

Figure 4.15. The schematic diagram of spacer-free of patterning

As solvent evaporation progresses, the solution splits in the grooves, and the fresh liquid surface migrates towards the sidewalls of the grooves, thus, the solution is patterned into liquid bridges held between the substrate and ridges of the template. Because the template is well wetted with organic solvent, a tiny amount of solution is trapped in the groove corners (indicated by black arrow) [8] [9], and merges into the capillary bridges. Thus, the contact line between the liquid bridge and the substrate is also pinned by the groove, because a liquid film is always trapped between the template-ridges and substrate when a template is attached to a wet substrate. The template moves down as the solvent evaporates, eventually touching the substrate when drying is complete. The second condition is when a spacer is applied to suspend the template, as show in Figure 4.15. As the solvent evaporates further, the capillary bridge splits and is dragged towards the groove, whereas the solute is further deposited next to the groove-pinned contact line. A spacer with sub-micrometer height can be directly fabricated on the template surface to control the gap between the template and the substrate.

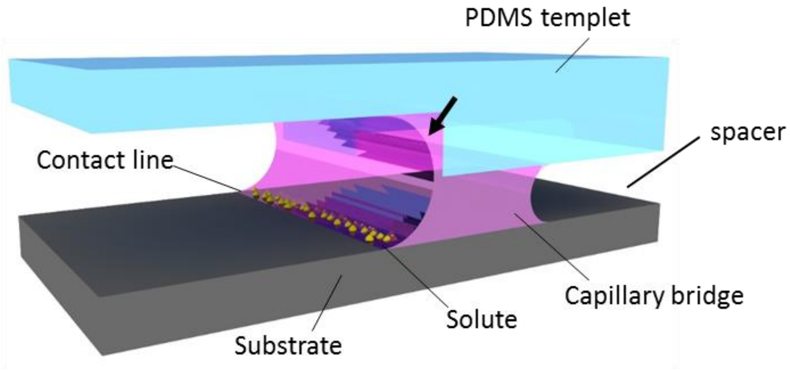

Figure 4.16. The schematic diagram of spacer-applied between template and substrate

Fabrications “with” and “without” a spacer were performed here, and I denote these two cases as “spacer-applied” and “spacer-free” configurations, respectively. Two experiments have been designed to prove this principle. The Figure 4.17 shows the result of a “spacer-free” experiment using poly(9,9-dioctylfluorene-alt-bithiophene) (F8T2), a p-type semiconductor polymer patterned from DCB solution. To further confirm the role of liquid bridges, I performed a double patterning in which the first layer of patterned lines acted as a spacer for patterning the second layer. The first patterned lines are created by poly-4-vinylphenol (PVP) from IPA solution via the same process as used for the F8T2 polymer, and then, the PVP pattern was used as a spacer to further pattern polystyrene (PS) from DCB solution. Figure 4.18 shows a grid image consisting of perpendicularly orienting PVP and PS lines, which were perfectly jointed at cross points. Both types of lines had similar morphologies originating from their similar formation mechanisms. Such multilayer fabrication is interesting for creating patterns from different functional materials, such as laterally heterojunction structures.

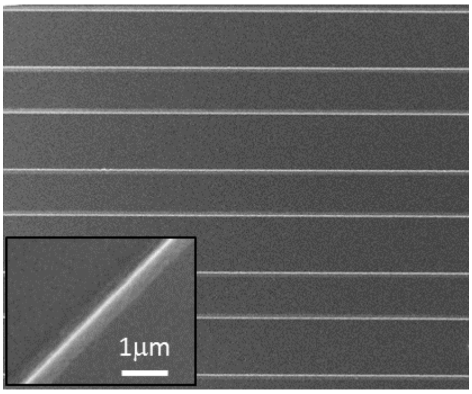

Figure 4.17.
The SEM image of patterned F8T2 lines

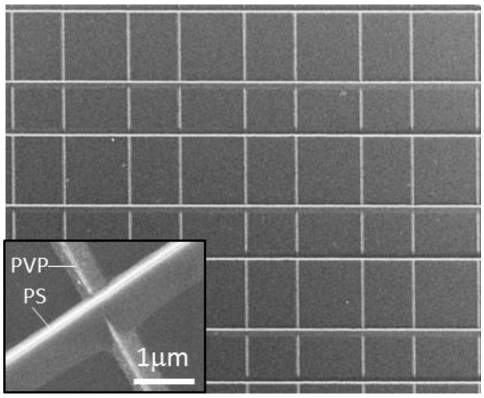

Figure 4.18.
The image of two materials cross joint structure

4.4.3 Liquid drying mechanics

To investigate the drying process an in-situ microscope was used to observe and track the pattern formation. Both transmissive and reflective modes were used. Samples were clamped in transparent plastic boxes with open holes to allow solvent evaporation. To observe the F8T2 pattern-formation using the transmissive mode glass substrates were used, whereas Si substrates were selected to investigate the drying dynamics of PS in reflective mode. The schematic diagram is illustrated in Figure 4.19.

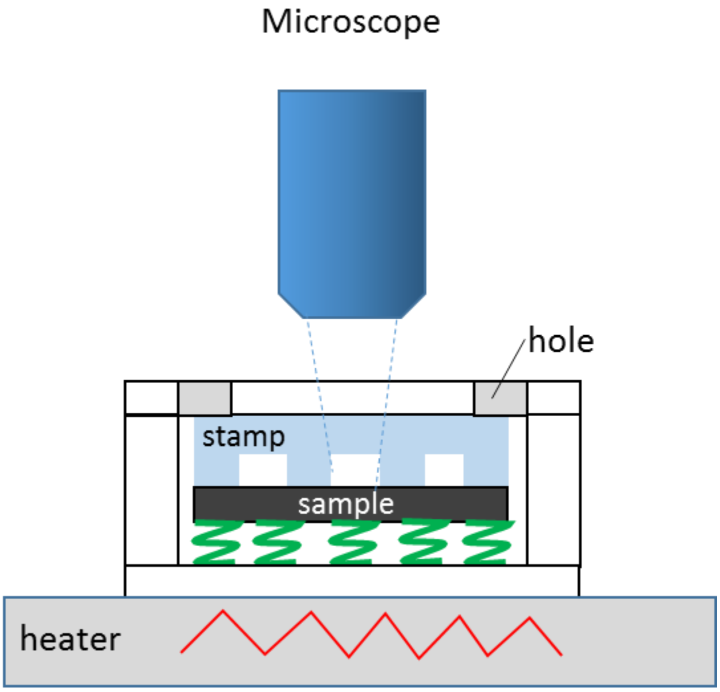

Figure 4.19.
The schematic diagram of dry processing observation by optical microscope

Taking advantage of the yellow colour of F8T2 polymer semiconductor, the "groove-pinning" mechanism was evident when the drying was observed under a microscope with transmitted light. Figure 4.20 shows an image taken at an earlier stage of drying (about2 min after the moment of sample loading) of a sample with the spacer-free configuration on a glass substrate, clearly showing the liquid-splitting and migration of the newly formed liquid/air interface towards the sidewalls of the grooves (indicated by a black arrow).

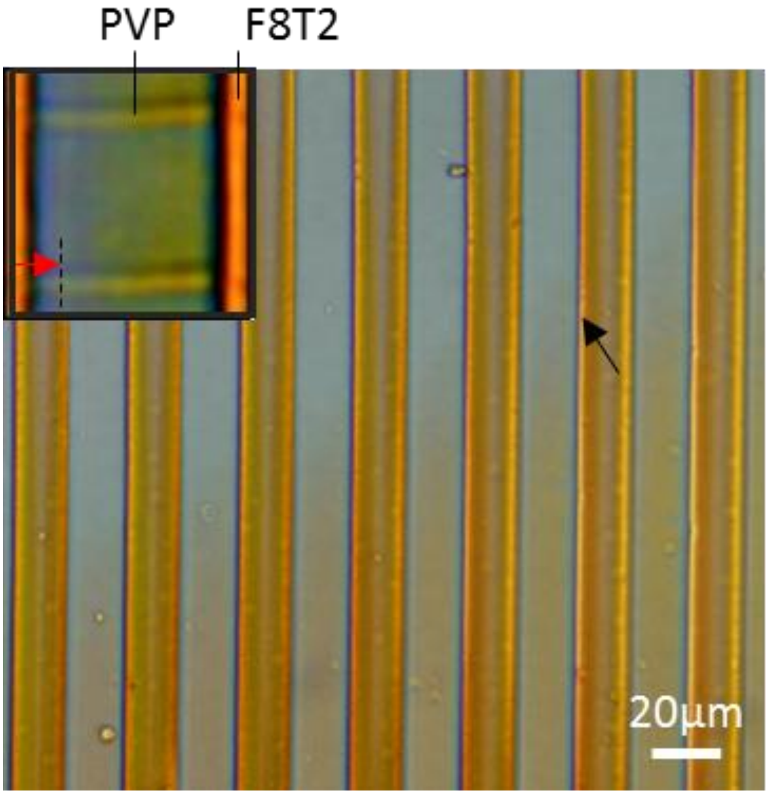

Figure 4.20. The optical image of patterning F8T2 lines

A similar event was noted in the spacer-applied configuration when pre-patterned PVP lines were used as the spacer for the F8T2 patterning. A splitting of the liquid film underneath the ridges of the template occurred for samples with the spacer-applied configuration (red arrow in the inset of Figure 4.20). Figure 4.21 shows an in-situ image taken from the same sample as Figure 4.20 at a later stage of drying (about 10 min after sample loading), revealing fine 2008P lines deposited next to the sidewalls of the grooves.

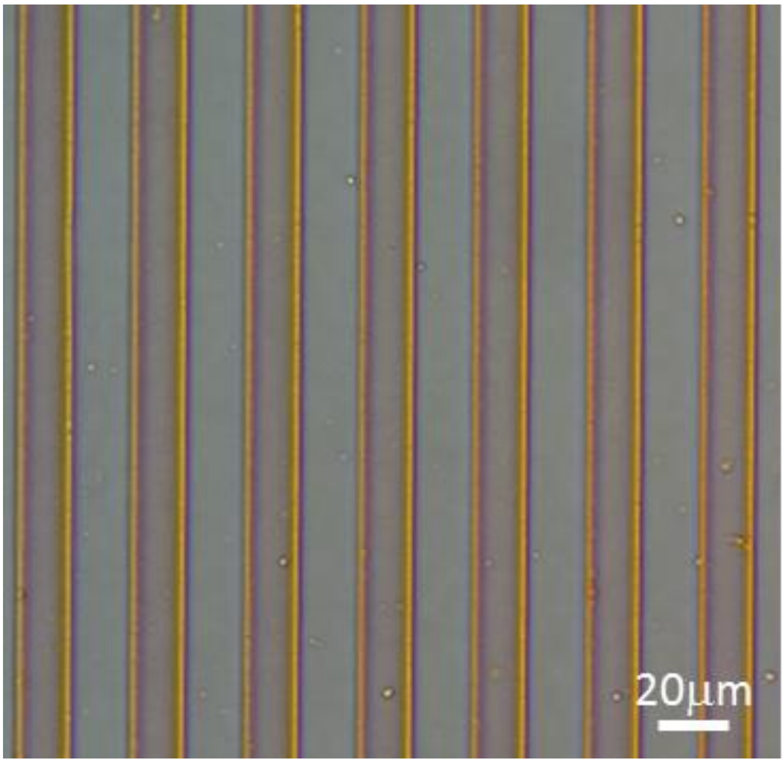

Figure 4.21. The pattern result of F8T2 wires array

The “groove pinning” is the central mechanism needed to achieve such fine patterning, although the substrate itself also contributes to the contact line pinning. If the “groove pinning” at one side of a template’s ridge is lost, the pinning strength of the substrate/solution’s contact line alone is not sufficiently strong to pin the liquid, and the solution is dragged into the space under the ridge by capillary forces and eventually merges with the liquid that is pinned by the neighbouring groove. This phenomenon was occasionally observed in my experiment and was likely caused by the structural deformation of the PDMS template resulting from shearing force, which can be avoided by optimizing both the mechanical properties of the template materials, such as adjusting the mixture ratio between the silicone elastomer and its cross-linker or enhancing the annealing temperature to make stamp more firmly, and the design of the experimental system. Figure 4.22 shows the failed patterning of F8T2 with PVP lines as the spacer on the Si substrate.

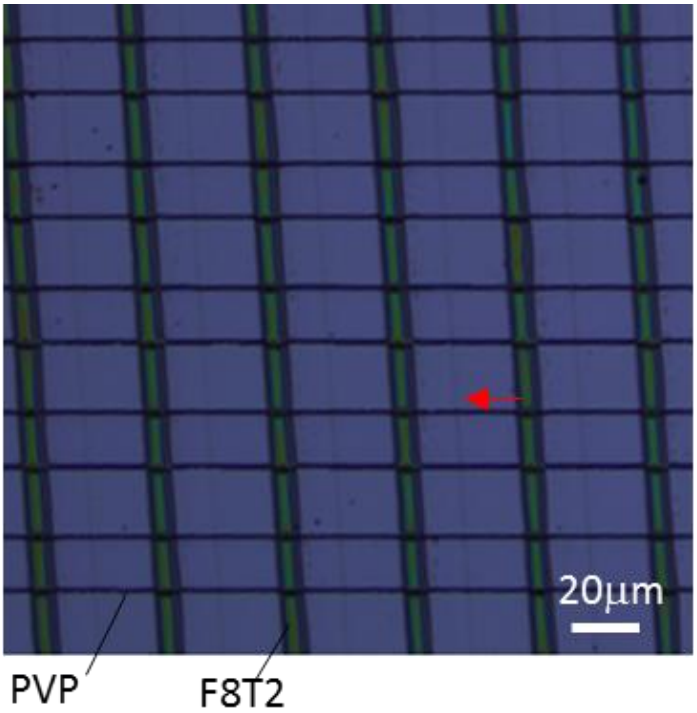

Figure 4.22. One of the sidewall depinning during the pattern processing

Fine polymer lines formed before the onset of depinning are clearly evident (indicated by a red arrow), indicating that the capillary flow-induced edge deposition in the liquid bridge was the dominant mechanism for solute transportation to the contact line. If the pattern formation arises because of solution aggregation and condensation onto the pinning lines, solute deposition will not occur before depinning, and thus, no such fine lines will be seen. Compared with liquid drops on a flat solid surface, the micro-liquid bridge is more favourable for solute transfer to the pinned contact line because the evaporation from the top surface is restricted. Thus, the resulting outward flow can carry all of the dissolved material to the pinning lines.

For the template (12 mm×12 mm with 10 mm×10 mm patterned area) used here, normally we cannot observe obvious traces that reveal how air is introduced from the external environment during drying under an optical microscope. Both externally migrated air and air trapped in the PDMS materials can contribute to the solvent extraction [10]. When a PDMS template, which is cut in its structured area along the direction perpendicular to the grooves, is used, air trapping from the external environment can be seen with reflected light under a microscope. To observe the air-inletting process, PS was dried from a DCB solution on a silicon substrate using both the spacer-free and spacer-applied configurations. Figure 4.23 shows the air-inletting into the template grooves during drying with the spacer-applied configuration.

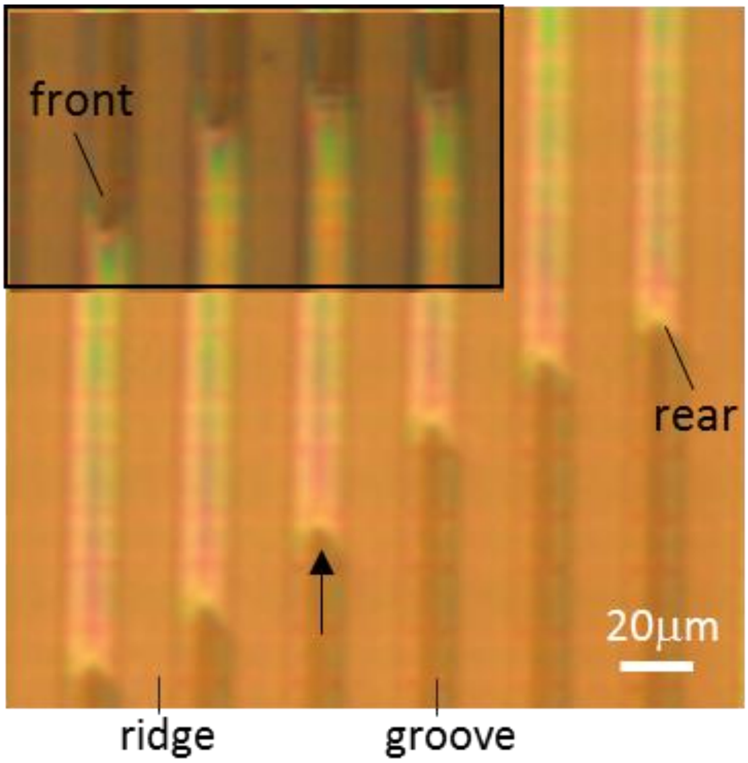

Figure 4.23. The air-inletting into the template grooves

Both the “front” (inset of Figure 4.23) and the “rear” of the mixed region have similar concave shapes and move into the sample from the edge with equal speed. In this case, the rear of the bright stripe is the region where the liquid splits in the grooves and pattern formation begins (an arrow indicates the rear of a mixed region and its moving direction in Figure 4.23). Although the air inlet and the liquid patterning process are different from those observed using the F8T2 sample without cutting the template (Figure. 4.20), the obtained fine patterns were similar.

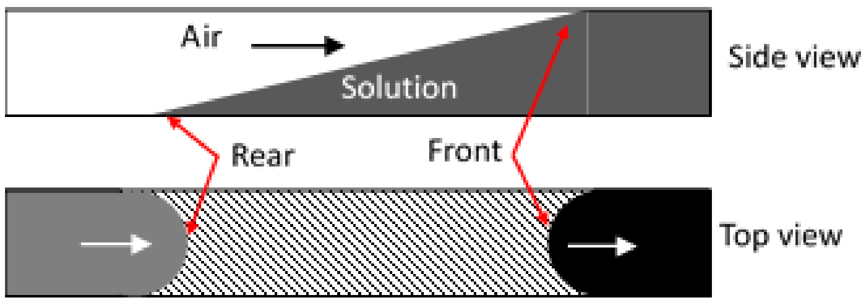

Figure 4.24. The side-view and top-view of solution movement in PDMS channel

Figure 4.24 shows a schematic illustration of the mixed region of air and solution in a template groove. The direction of air movement and a wedge-shaped liquid are shown in the side-view panel. The shaded area in the top-view panel corresponds to the bright stripe observed under the optical microscope. White arrows indicate the advancing direction of both the front and rear of the mixed region. Under an optical microscope with reflected light the air/liquid interface was highly reflective and appeared to be brighter.

The result of the “space-free” patterning PS experiment with 200 nm feature size has been shown in Figure 4.25. During the SEM observation, I also found a set of secondary patterns with very high resolution (about 50 nm feature size) decorated on the walls of the lines generated above (i.e., the primary pattern). Figure 4.26 and Figure 4.27 show these nano-sized stripe patterns on the PS and F8T2 wires generated with the spacer-free configuration.

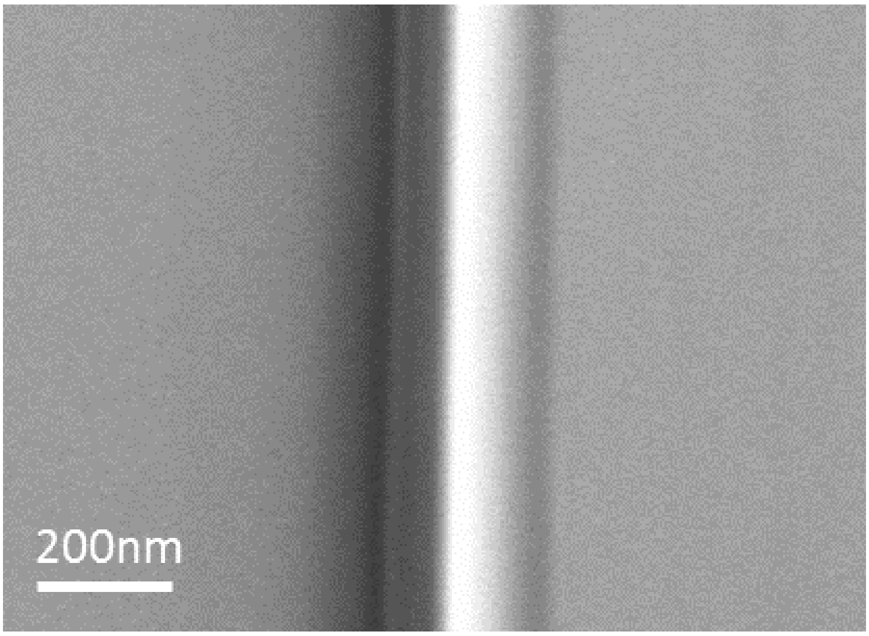

Figure 4.25. The SEM image of PS line

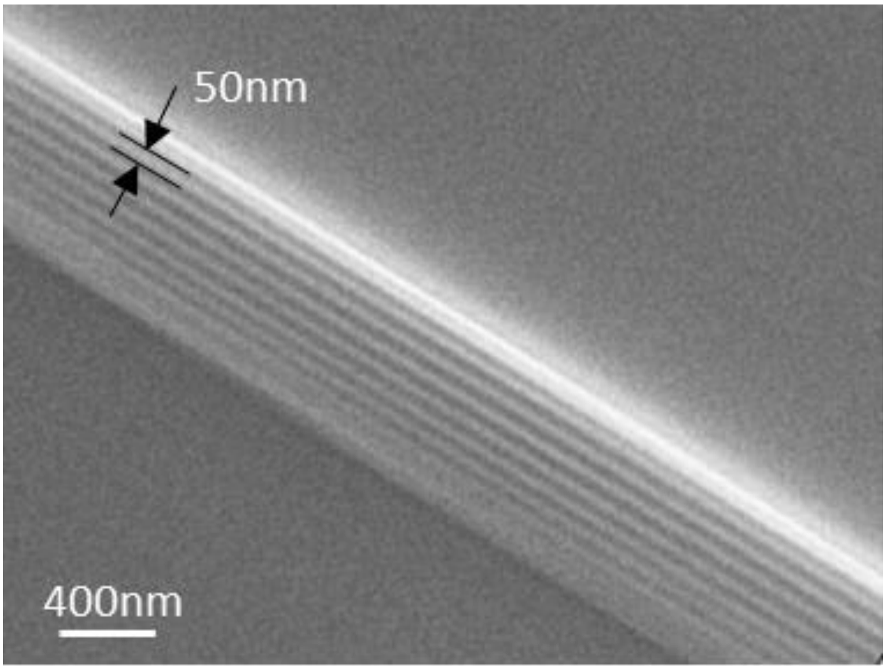

Figure 4.26. The nano-sized stripes in PS wire

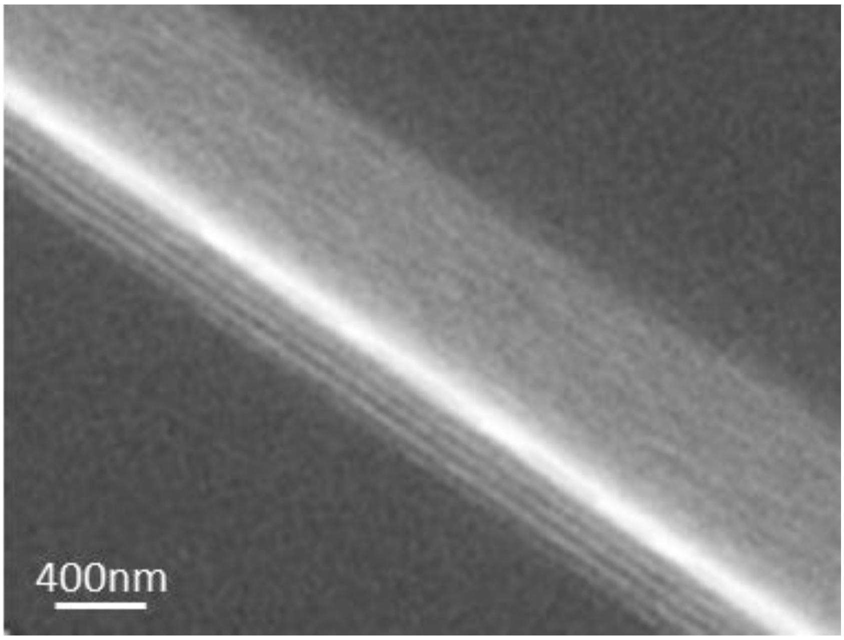

Figure 4.27. The nano-sized stripes in F8T2 wire

The nano-stripes only appear on the sidewalls that face the template ridges when patterning is conducted with the spacer-free configuration. I explain this feature as resulting from a repeated pinning-depinning event during the late stage of drying when the template-ridges reach the substrate and a tiny amount of solution becomes trapped in a wedge-shaped space between a sidewall of a groove and the adjacent newly formed primary polymer line. This process has been illustrated in Figure 4.28. The feature size of the nano-stripes was two orders of magnitude smaller than that previously observed for self-assembled micrometre-sized structures formed from drying solution [11][12].

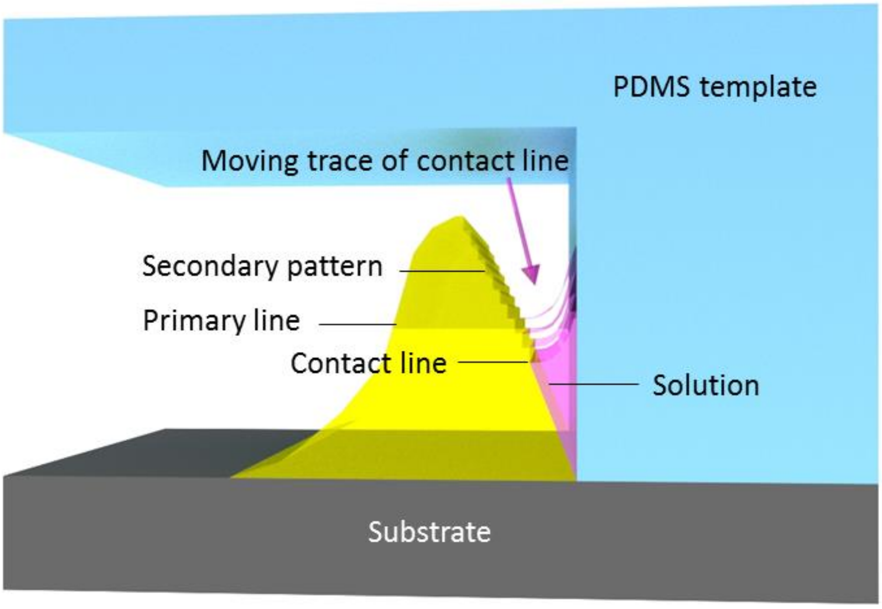

Figure 4.28. The secondary pattern formation on between the sidewall and contact line

There is some similarity between the secondary pattern found here and that observed from a drying solution confined between spherical/flat surfaces: In both cases, the liquid was confined in a wedge-shaped space, and the obtained stripe-distance varied gradually [11]. Carefully examining the nano-stripes revealed that the inter-stripe distance varied uniformly with about 3-4 nm increment between two neighbouring stripes in the PS pattern. See the Figure 4.29 below.

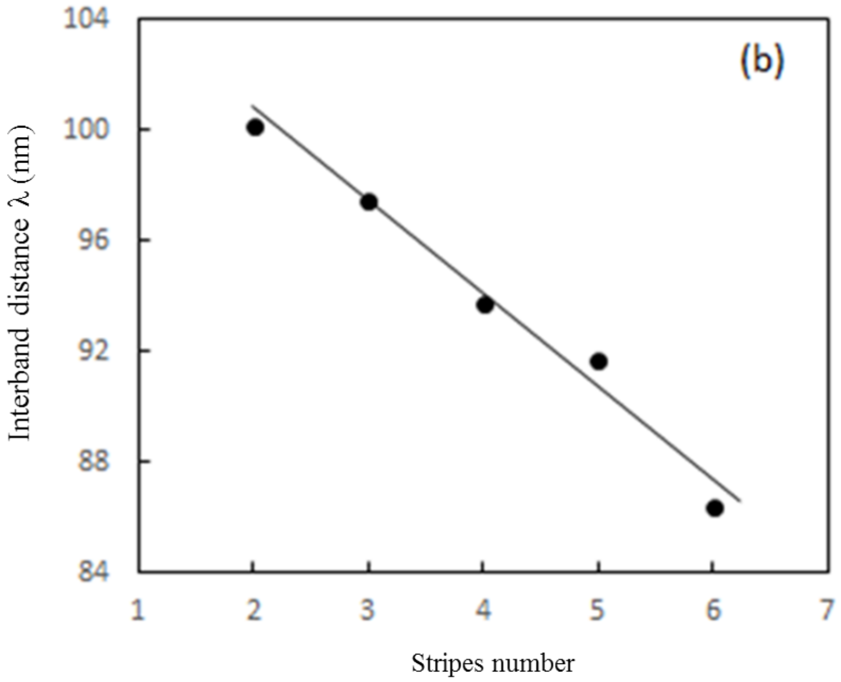

Figure 4.29. The variation of inter-stripe distance with stripe number

The Figure 4.30 shows a SEM image of a cross-section of a fabricated PS line. Although the morphology was strongly disturbed during sample cleavage, the profile on the sidewall can still be seen.

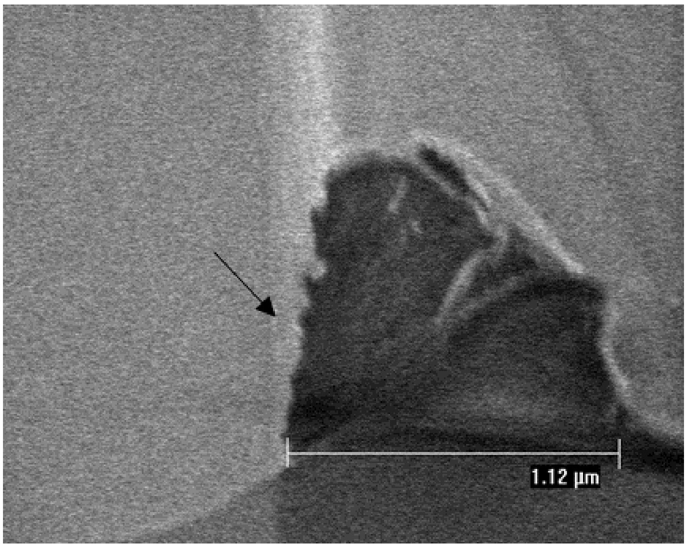

Figure 4.30. The SEM image of PS line cross-section

I have also used the “space-free” method to pattern P[NDI2OD-T2] on a silicon substrate, Figure 4.31 shows the patterning result with 400 nm feature size under SEM observation.

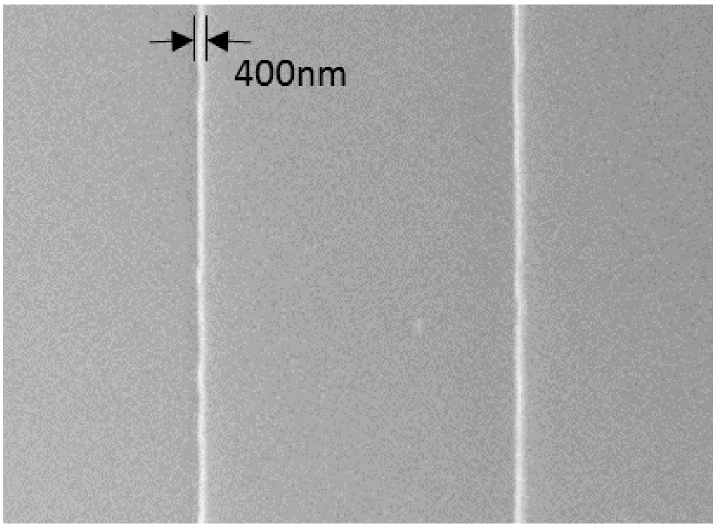

Figure 4.31. The SEM image of P[NDI2OD-T2] line

4.4.4 Solvent extraction at variable temperatures

I have chosen DCB and IPA as the solvents in my experiments because a high-boiling point solvent allows for sufficient implementation time. Additionally, if drying the samples at elevated temperature or using a solvent with a low boiling point, the patterning can be achieved in a minute, revealing the potential to scale-up this process. This fast pattern formation results from efficient solvent extraction during drying. To obtain more information about solvent extraction, I performed an in-situ investigation at various temperatures, in which PS was dried from DCB solution on a silicon substrate with the spacer-free configuration. A series of samples at different temperatures were examined. I measured the advancing speed of the air-front at various temperatures and confirmed that the advancing speed of the air-front did not depend on its location; i.e. it is constant regardless of its location on the sample (i.e., edge or centre). Taking the advancing speed of the air-front at 40°C degree for example, the original data have been displayed in Table 3.

From this table, the linear relation between the air-front displacement and time revealed that the air-font advanced with a constant speed in the grooves. This relationship has been illustrated in Figure 4.32 (a) below. The advancing speed at 50℃ and 60℃ has also been examined and data are displayed in table 4 and 5, respectively.

Distance (μm)	0	7	14	21	28	35	42	49	56	63	70	84	91	98	112	126	140
Time (s)	0	2	5	9	12	15	18	21	24	27	30	33	36	39	42	45	48

Table 3. The advancing speed of the air-front at 40℃

Distance (μm)	0	14	28	36.4	37.8
Time (s)	0	2	5	10	25

Table 4. The advancing speed of the air-front at 50℃

Distance (μm)	0	42
Time(s)	0	3

Table 5. The advancing speed of the air-front at 60℃

Ignoring the measurement uncertainty, the speed, *V,* and drying temperature, *T,* exhibit an exponential relationship:

$$V = V_0 \exp(-Q/kT) \tag{5}$$

where *Q* and *k* are the activation energy and Boltzmann constant, respectively. The constant speed observed at a giving temperature was unexpected because the advancing speed of the air-front should have slowed when it was propelled into the deep side of the sample if the solvent extraction was controlled by vapour diffusion. By fitting my experimental *V-T* curve in Figure 4.32(b) with equation (5) above, through calculation, the activation energy $Q = 5.96\times10^{-20}$ (J) and enthalpy of vaporization of the solvent $E = N_aQ$ = 36000 (J/mol) were determined, where N_a is Avogadro's constant. This value is in good agreement with the chemical data sheet value of 39400 J/mol. Thus, the drying was controlled by the energy required by a solvent molecule to escape from the liquid surface rather than by diffusion. In other words, the solvent vapour can quickly be extracted once it leaves the liquid surface.

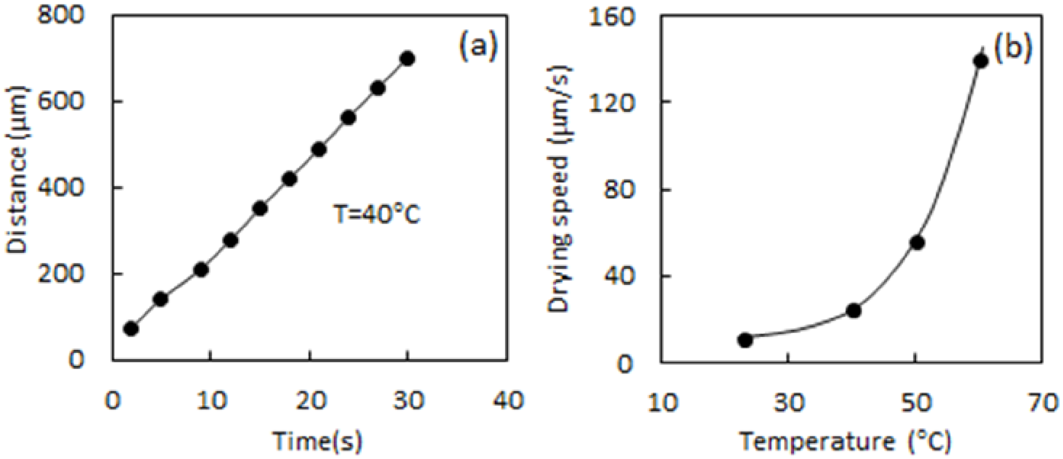

Figure 4.32. (a) Time dependence of displacement of air-front measured at 40 °C.
(b) Smooth interpolation (line) of the advancing speed of air-front at measurements (dots) at different temperatures

4.4.5 Patterning PVP wire by polymer material stamp

In the previous experiments, all the material wires were produced by the PDMS stamp patterning method. The wire geometry was confined by the PDMS structure. If we want to obtain the opposite structure, the plasma etching technique is necessary, but it inevitably increases the cost of fabrication. Another kind of polymer material will be introduced in this part, and a pattern transfer of the PDMS structure can be obtained by it. The specific processing has been demonstrated in Figure 4.33.

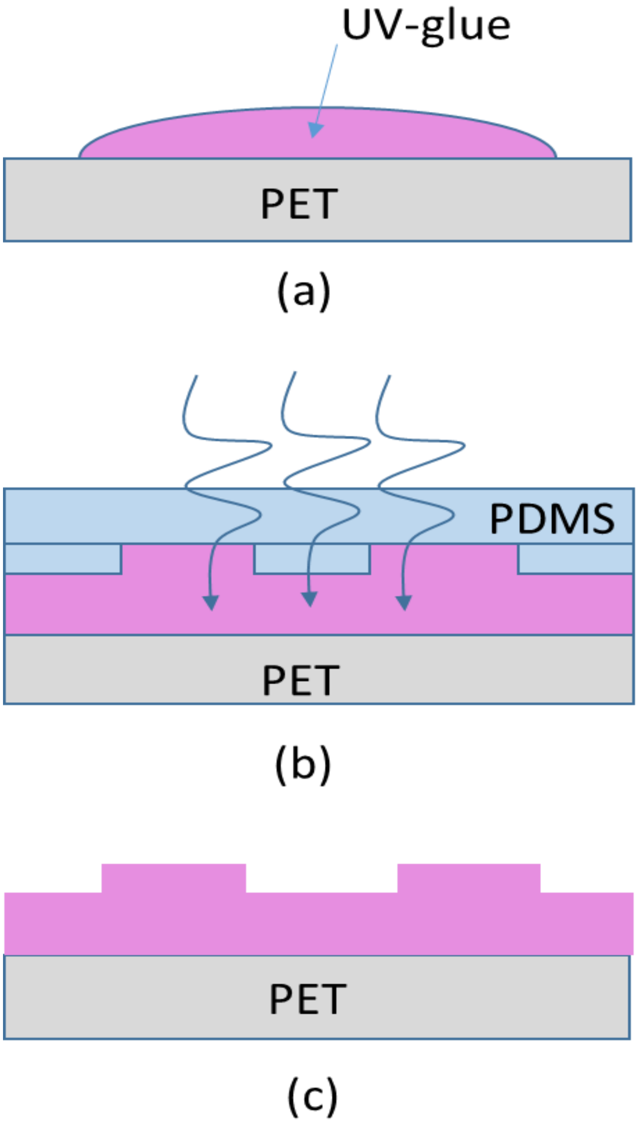

Figure 4.33. The PDMS structure pattern transfer to UV-glue material on PET substrate.
(a) Deposit UV glue on PET substrate (UV glue: NEA 123L)
(b) UV Cure under PDMS
(c) Peel off PDMS

The full name of NEA 123L is Norland Electronic Adhesive, which is a single component adhesive that cures tack free in seconds to a tough, resilient polymer when exposed to ultraviolet light. The specific parameters and properties of this material can be found on the supplier's website. The UV-glue solution was drop cast on a well cleaned PET substrate (10mm×10mm), the thickness of the film was about 1 μm. Then, a certain pressure was given by the clamping tool on the prepared PDMS stamp until the stamp's grooves were embedded into the material surface. Under the UV light, the material cured quickly. The final step was peeling the PDMS off and leaving an opposite structure on the PET substrate. The PVP lines have been successful patterned by using this new template. The PVP lines patterned by the UV-glue template are demonstrated in Figure 4.34.

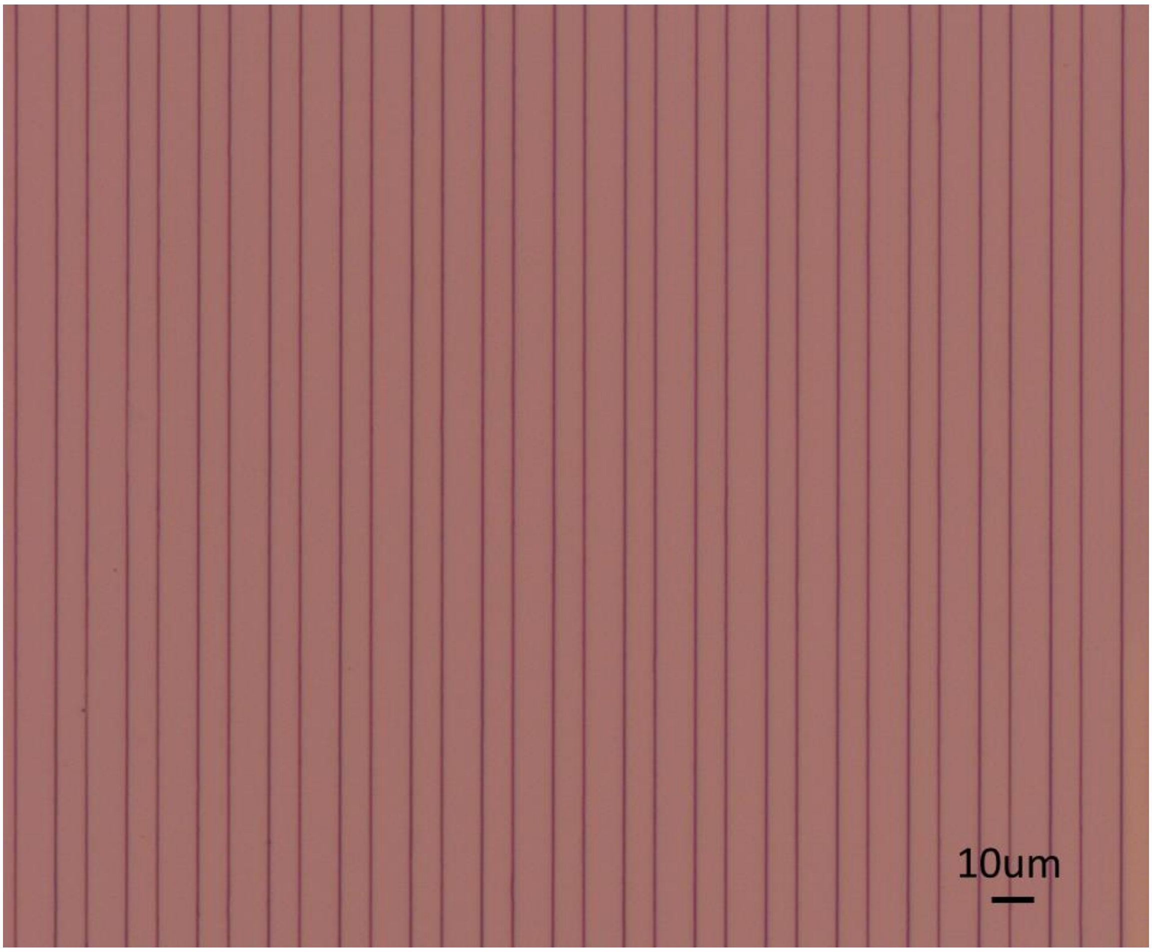

Figure 4.34. The PVP line array patterned by UV-glue template on a Si substrate

Compared to the previous patterning method, this is the first time I used polymer material to fabricate the groove structure stamp on a flexible PET substrate. From the image of the PVP line array, we can see the quality of wire array is the same as those wires which were fabricated by a PDMS stamp. This shows that no matter what kind of material is used to make a stamp, as long as the regular groove structure in the stamp is formed and the edge of groove is rigidity and sharp enough, in the patterning process, the wire array can be easily acquired.

4.6 Summary

All of the organic semiconductor materials with their effective solvents have been introduced in this chapter. In the pattern processing part, the details of both PDMS template preparation and optimization of the solution parameters are described, finally obtaining well-ordered beautiful organic material wires based on the “coffee-stain” phenomenon. The “space-free” and “space-applied” experiments have been done to reveal the mechanism of the wire formation during the patterning process. From which, we can understand that the core mechanism to achieve the fine wire array patterning is “groove pining”. If we want to acquire the best result both sides of the template’ ridges must be pinned firmly; losing one of side will result in patterning failure. Besides, the PDMS stamp fatigue is another factor that can affect the result. We know that the rubber will age if it is used for a long time. Therefore, it is observed that the edge has a concave deformation or defects before clamping, the stamp must be replaced. Anyway, the

PDMA stamp technique achieves large-area well-ordered organic material stripe array patterning compared to the flow coating method, and also obtained grid structures that once were thought to be difficult to achieve.

Reference

1 Bellis, M. The History of Plastics. *About. com Inventors. In article*, (2011).

2 Brierley, G. J., Ferguson, R. J. & Woolfe, K. J. What is a fluvial levee? *Sedimentary Geology* **114**, 1-9, (1997).

3 Pizzuto, J. E. Sediment Diffusion during Overbank Flows. *Sedimentology* **34**, 301-317, (1987).

4 Zhang, L. *et al.* Inkjet printing high-resolution, large-area graphene patterns by coffee-ring lithography. *Adv Mater* **24**, 436-440, (2012).

5 Fang-Chung, C., Jhih-Ping, L. & Wen-Kuei, H. Using Ink-Jet Printing and Coffee Ring Effect to Fabricate Refractive Microlens Arrays. *IEEE Photonics Technology Letters* **21**, 648-650, (2009).

6 Huh, C. & Mason, S. G. Effects of Surface-Roughness on Wetting (Theoretical). *J Colloid Interf Sci* **60**, 11-38, (1977).

7 De Gennes, P.-G. Wetting: statics and dynamics. *Reviews of modern physics* **57**, 827, (1985).

8 Seemann, R., Brinkmann, M., Kramer, E. J., Lange, F. F. & Lipowsky, R. Wetting morphologies at microstructured surfaces. *Proceedings of the National Academy of Sciences of the United States of America* **102**, 1848-1852, (2005).

9 Pomeau, Y. Wetting in a Corner and Related Questions. *J Colloid Interf Sci* **113**, 5-11, (1986).

10 Toepke, M. W. & Beebe, D. J. PDMS absorption of small molecules and consequences in microfluidic applications. *Lab on a Chip* **6**, 1484-1486, (2006).

11 Xu, J. *et al.* Self-assembly of gradient concentric rings via solvent evaporation from a capillary bridge. *Physical review letters* **96**, 066104, (2006).

12 Lin, Z. & Granick, S. Patterns formed by droplet evaporation from a restricted geometry. *J Am Chem Soc* **127**, 2816-2817, (2005).

Chapter 5

Organic transistor fabrication and measurement

5.1 Introduction

In the previous chapter, the principle and method of patterning organic material wires have been introduced and the related results also were demonstrated. In this chapter, all the detail results of different type OFET fabrication by using these patterned wires and the device performance will be presented.

5.2 Organic field effect transistor fabrication and measurement results

When these organic polymer semiconductor wires are patterned successfully, the next task is transistor fabrication. The specific steps have been introduced in Chapter 3. Compared to the conventional fabrication method, the active layer geometry is to have a polymer wire array instead of thin films. But the rest of procedures, such as the baking and post-baking time, are identical with the conventional method.

5.2.1 The shadow mask preparation

Because the active materials have been self-assembly deposited on the substrate during the patterning process, the electrode fabrication has to be completed by using a shadow mask. For the shadow mask preparation, I chose a piece of aluminum as the mask template due to its softness. By cutting out a rectangular piece in the middle of the aluminum board, one can then fix several 20 μm diameter gold wires on the rectangular area. Thus, a “handmade” shadow mask is completed. The whole production process is demonstrated in Figure 5.1.

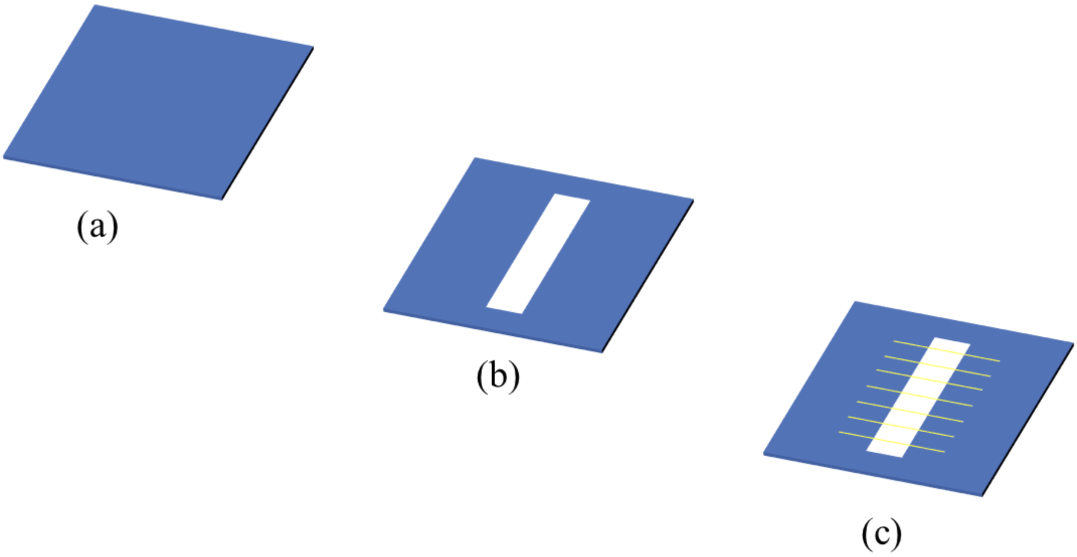

Figure 5.1. The handmade shadow mask
(a) An aluminum board
(b) Cutting out a rectangle piece from the board
(c) Fixing gold wires on the rectangle area

Another kind of special shadow mask was also designed to ensure that electrodes can be deposited on both ends of each wire as shown by Figure 5.2. The purpose of designing this mask is to measure the single polymer wire characteristics.

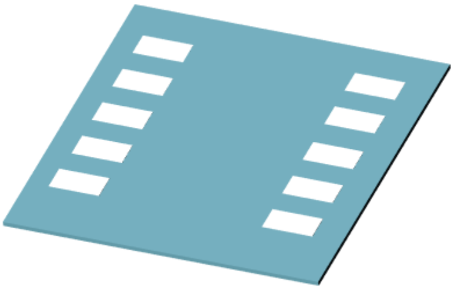

Figure 5.2. The shadow mask for the wire ends

The last part is the photomask. This is a column of transparent square structures in the middle of a black glass substrate as shown in Figure 5.3. The specific application of this photomask will be introduced in the following sections.

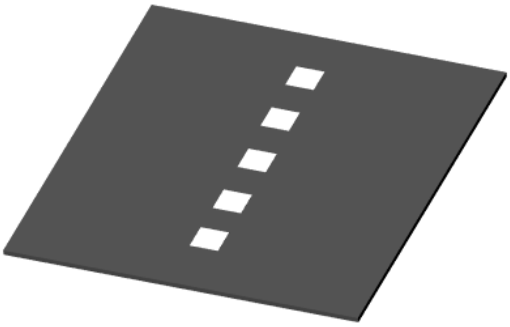

Figure 5.3. The photo-lithography mask of holes

In brief, three kinds of masks have been demonstrated here. All of them have been employed for different purposes. The details will be discussed in the following experiments.

5.2.2 Organic field effect transistor fabrication (OFET) and result

In the device fabrication, all polymer solutions were spin-coated on SiO_2(300nm)/Si substrate. Before material patterning, the silicon dioxide wafer must be well cleaned to ensure there is not any contamination on the surface. The wafers were first immersed in acetone and ultrasonically cleaned for 15 minutes. After cleaning, they were rinsed repeatedly with isopropyl alcohol for 2 minutes and then rinsed again with deionized water for 5 minutes. After been blown with water droplets by a nitrogen gun, the wafers were finally dried at 80℃ on a hotplate for 3 minutes to evaporate the surface thin film water and then used immediately. The polymer semiconductor thin film was transformed to the wires through the patterning process.

The first device I fabricated was a top-gate field effect transistor (FET) made with an array of P(NDI2OD-T2) wires (about 700 nm width) created from DCB solution on a substrate. We can see from Figure 5.4 that the purple area is the transistor channel. This image was taken before the gate electrode deposition on the channel area, but the electrodes deposition was finished and a 20 μm length of channel formed on substrate.

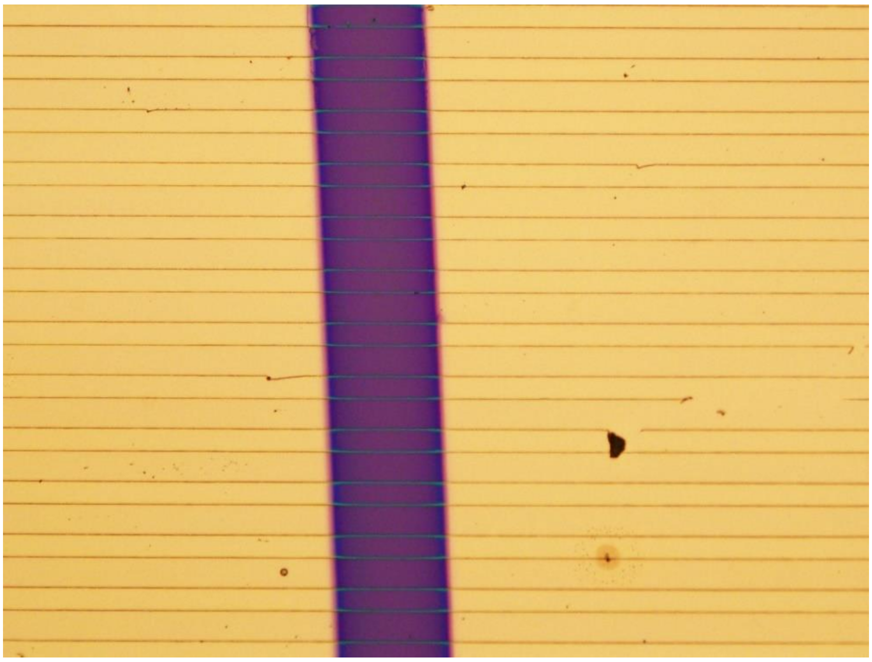

Figure 5.4. The optical image of top-gate P(NDI2OD-T2) wires array field-effect transistor with 20μm of channel length

These wires were annealed at 110°C for 4 hours after drying at 80℃ for 10 minutes. Then spin-coated poly (methyl methacrylate) (PMMA), thermally evaporated Au

(30 nm)/Cr (10 nm) and Al (30 nm) by shadow mask were used as the dielectrics, source/drain and gate electrodes. Because the gold cannot stick on the silicon wafer firmly, therefore, a 10 nm thick Chromium layer was evaporated on the silicon wafer firstly as a seed layer for the Au electrode deposition. This method was also used in other devices fabrication. The device was tested by a semiconductor analyzer. Since it was an n-type transistor, in the testing process, the drain voltage was set at 30 volts; the range of gate voltage was given from -10 volts to 30 volts. The result of the original transfer curve has been acquired and demonstrated in Figure 5.5. In this figure, the value of the threshold voltage cannot be easily determined. Therefore, usually, I expressed the result logarithmically and obtained a corresponding outcome that has been displayed in Figure 5.6. From which we can see clearly that the transistor was switched “on” when 0 voltage was applied on it and reached saturation state when the voltage was 30 volts. The on/off current ratio and the charge carrier mobility of the device were about 10^4 and $1.75 \times 10^{-2} \mathrm{cm}^2/\mathrm{Vs}$, respectively, which are similar to the values we obtained using a device containing a P(NDI2OD-T2) thin film [1]. The output curves have been demonstrated Figure 5.7, which also shows that the device begins to work at 0 volt.

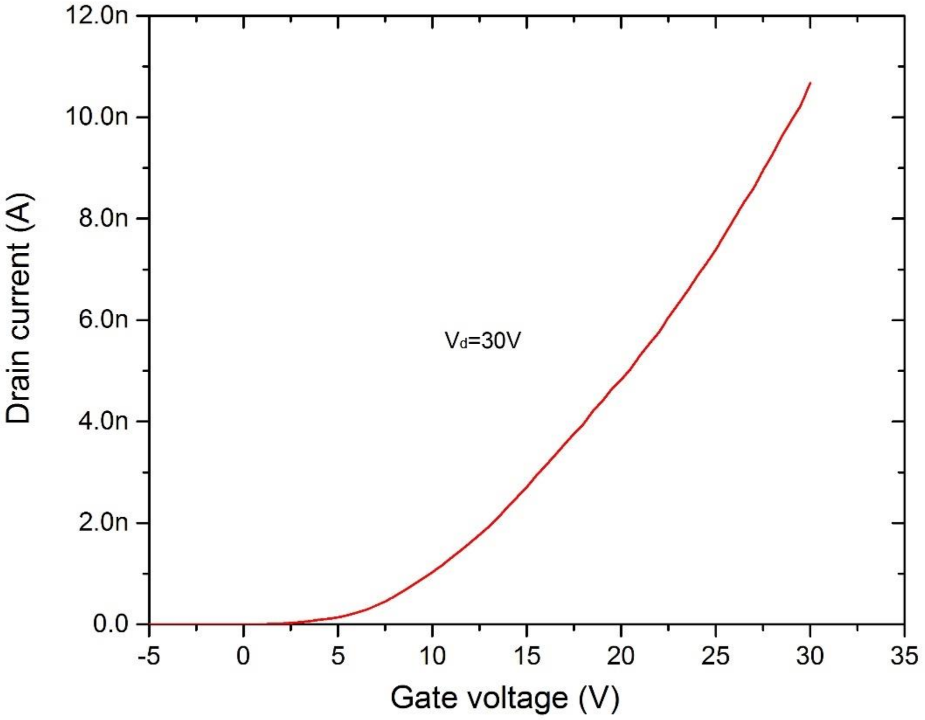

Figure 5.5. The transfer curve of P(NDI2OD-T2) top-gated field effect transistor

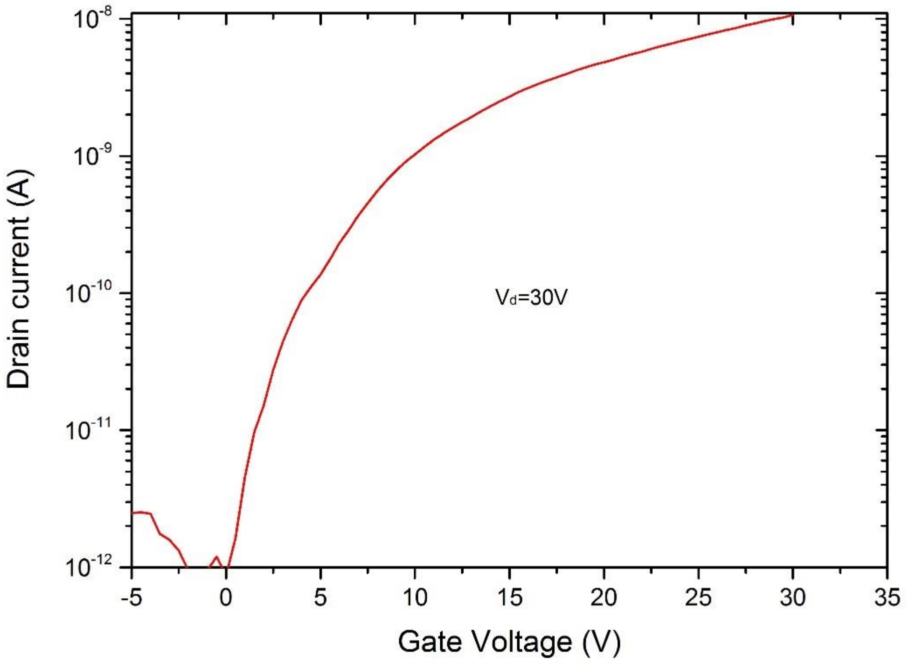

Figure 5.6. The logarithmic transfer curve of P(NDI2OD-T2) top-gated field effect

transistor

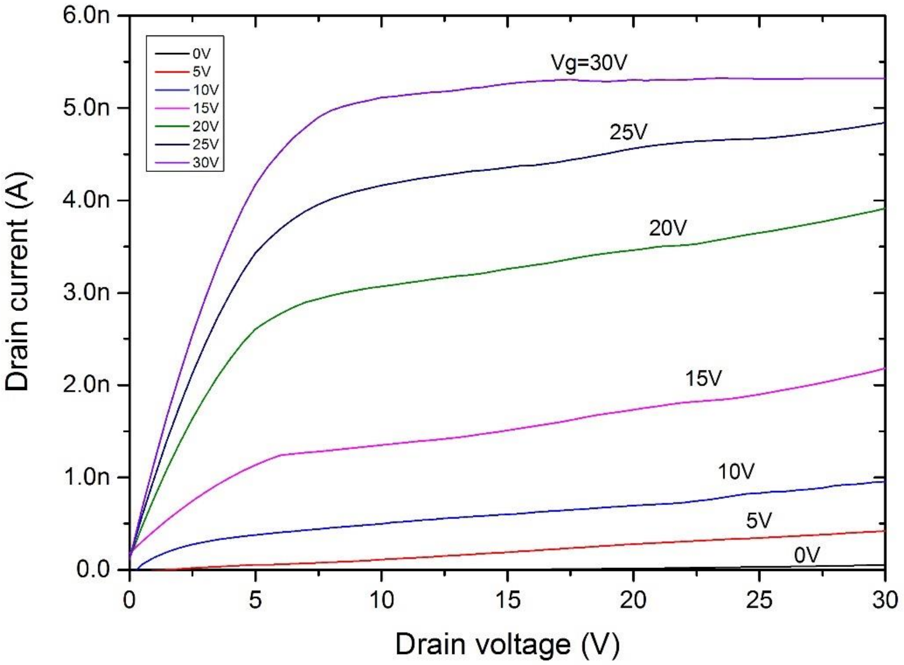

Figure 5.7. The outputs curve of P(NDI2OD-T2) top-gated field effect transistor

Figure 5.8 shows the fabrication process of a bottom-gate OFET made from p-type poly(3,3‴-didodecylquaterthiophene) (PQT-12) wires. An array of PQT-12 wires with 800 nm widths was created by drying PQT-12 from a DCB solution on SiO_2(300nm)/n+-Si substrate. In the annealing step, the PQT-12 wires were dried at 80℃ for 10 minutes followed 140℃ for 30 minutes. Au (30 nm)/Cr (10 nm) source/drain electrodes were finally deposited by thermal evaporation through a shadow mask. In this device, Si was used as the gate electrode. Because the material of substrate is silicon and silicon dioxide, the gate fabrication process was very simple; I just used a diamond cutter to scratch the silicon dioxide area on the opposite side of the channel until the silicon was exposed. The device optical image has been shown in Figure 5.9.

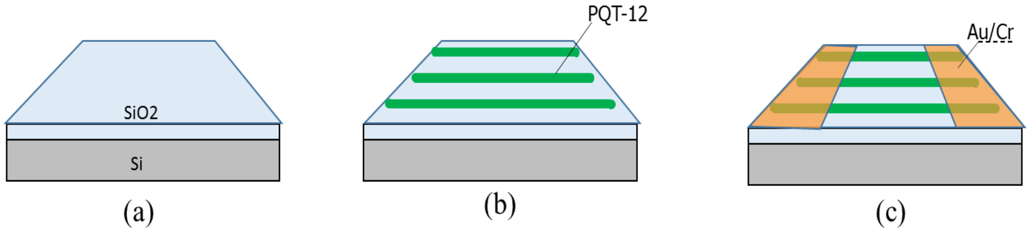

Figure 5.8. The fabrication process of bottom-gated PQT-12 FET
(a) Substrate preparation
(b) Semiconductor wires creation
(c) Source and drain electrode deposition

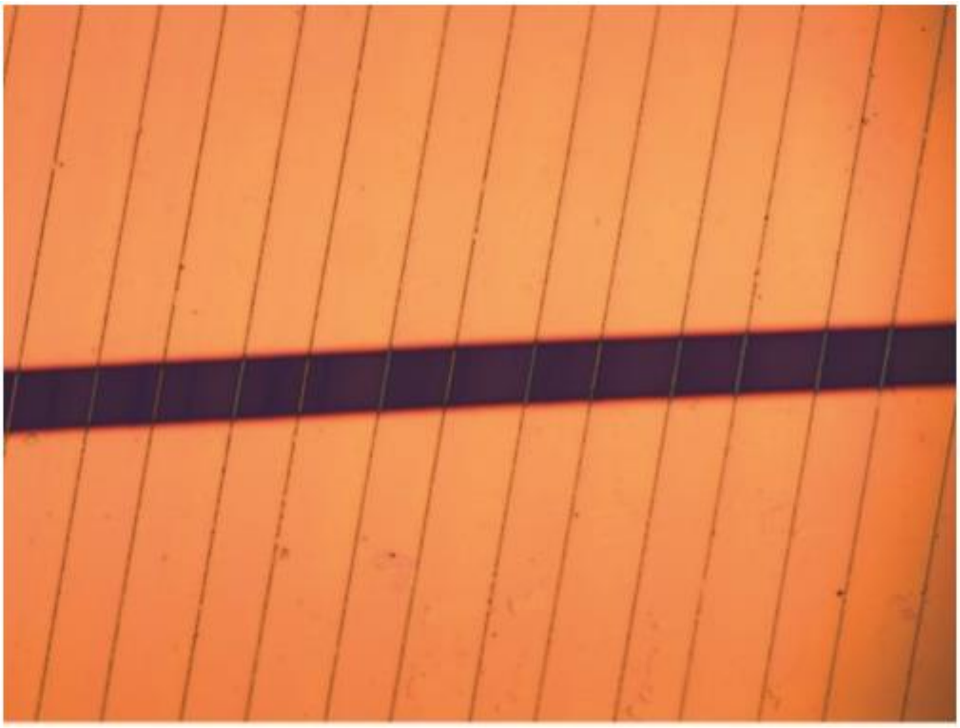

Figure 5.9. The optical image of bottom-gate poly(3,3‴-didodecylquaterthiophene) (PQT-12) field-effect transistor

The bottom-gate OFET original transfer curve with its corresponding logarithmic transfer curve are displayed in Figure 5.10 and Figure 5.11, respectively. Since the active layer material in this device was a kind of p-type organic semiconductor, the device should work when a negative voltage was applied on the gate electrode. In the testing process, the range of gate voltage value was set from 20 volts to -50 volts. The drain voltage was set at -30 volts. In Figure 5.11, we can understand that the minimum voltage (threshold voltage) to switch "on" the device was about 0 volt, and the gate was "off" when the gate voltage reached at -50 volts. The on/off current ratio was about 10^3. The hole mobility of the device was found to be 1.75×10^{-3} $\mathrm{cm^2/Vs}$. The outputs with different gate voltages is displayed in Figure 5.12, from which we can find that the minimum current was generated when the gate voltage was zero. Both results match excellently.

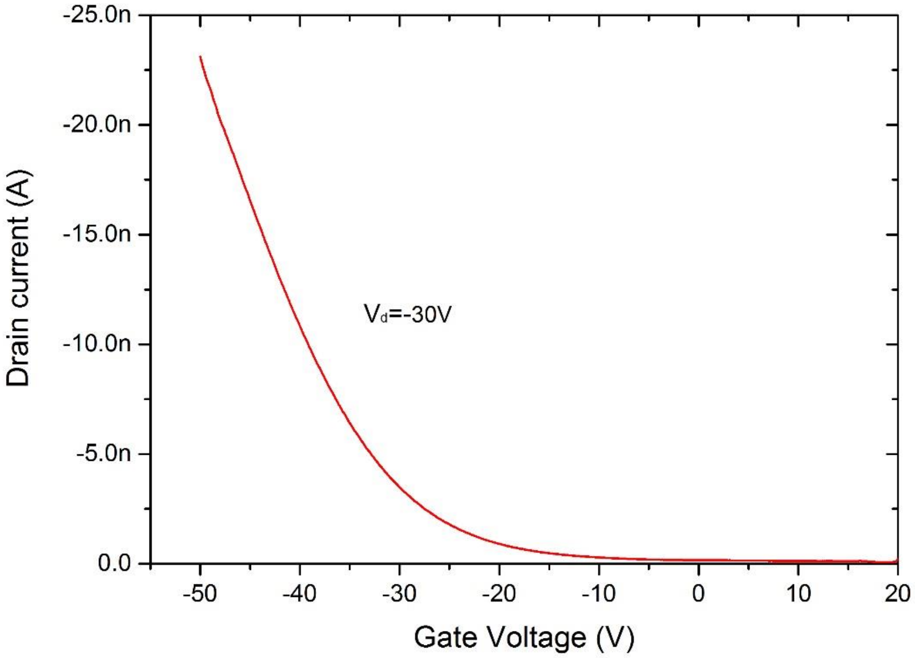

Figure 5.10. The transfer curve of poly(3,3‴-didodecylquaterthiophene) (PQT-12) top-gated field effect transistor

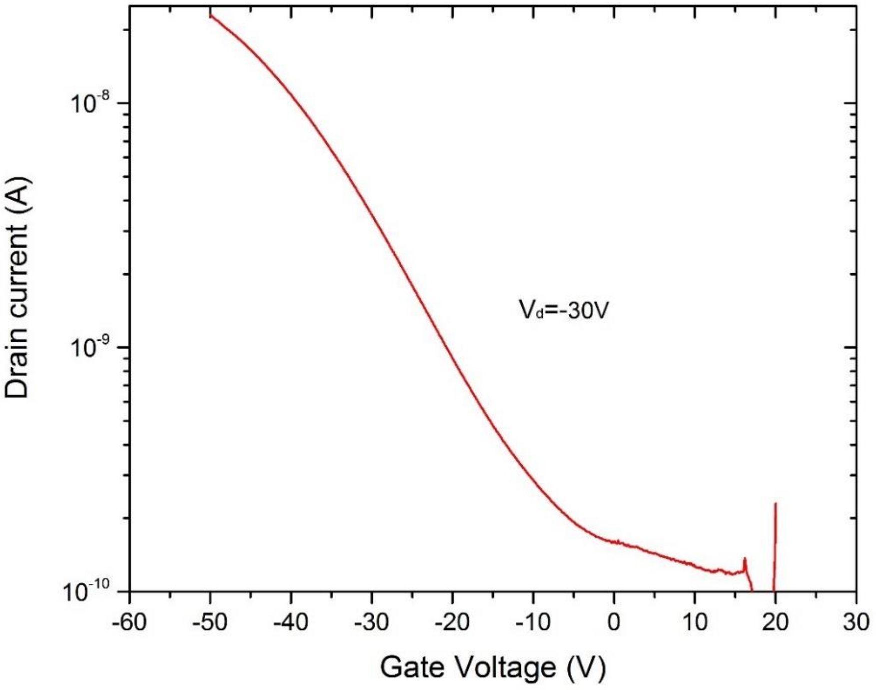

Figure 5.11. The logarithmic transfer curve of poly(3,3‴-didodecylquaterthiophene) (PQT-12) top-gated field effect transistor

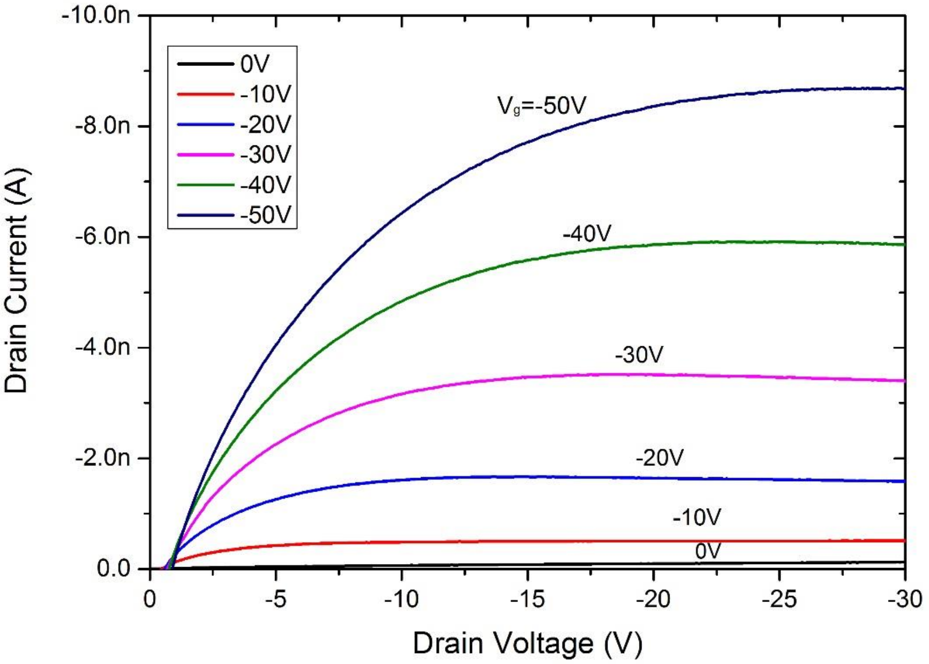

Figure 5.12. The outputs curve of poly(3,3‴-didodecylquaterthiophene) (PQT-12) top-gated field effect transistor

So far, the top-gate and bottom-gate OFET fabrication by utilizing different types of polymer semiconductor have been presented. Since the active layer geometry was changed from thin film to wires, therefore, the charge mobility formula was also modified from the original, which has been introduced in Section 2.4.2.3, to fit the experiment conditions:

$$\mu = \frac{2\lambda L d I_D}{W \varepsilon_r \varepsilon_0 \xi (V_G - V_T)^2} \tag{6}$$

where ξ and λ are the width and period of the patterned semiconductor wires, respectively; W and L are the channel width and length of the electrodes, respectively; ε_r, d and ε_0 are the relative permittivity, thickness of the dielectrics, and vacuum permittivity, respectively; and I_D, V_G, and V_T are the drain current, gate voltage and threshold voltage, respectively. The electron and hole mobility in n-type and p-type OFET are calculated through this equation, respectively.

In the polystyrene wire array patterning, the excellent result meets the requirement of OFET channel size. From Figure 5.13, through optical microscopy observation, we can see that the PS wire size was almost equal and the substrate area where it was uncovered by wires are clean. Based on this feature and excellent result, another top-gate p-type OFET has been fabricated.

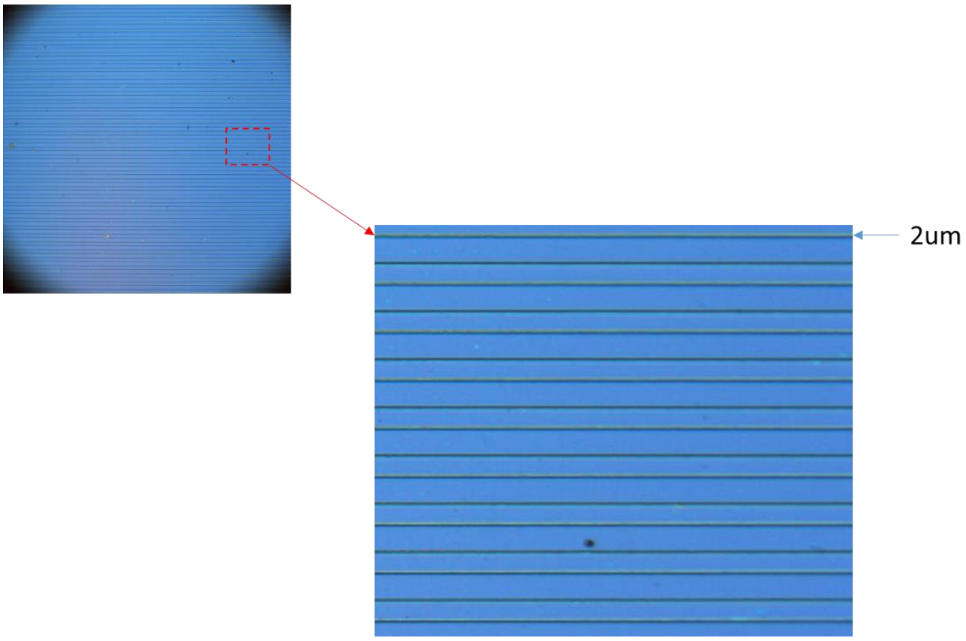

Figure 5.13. The optical image of patterning PS wires (×50) on silicon dioxides substrate

This whole fabrication process is shown in Figure 5.14. The PS wires are well patterned on the SiO_2 substrate surface at first. Different with the previous steps, Au/Cr are deposited by thermal evaporation before the polymer semiconductor deposition. Then PS wires are dissolved by a solvent in a lift-off step, leaving a very fine, about 1 μm, channel for the transistor. The success of this process has been demonstrated by Figure 5.15. Finally, the p-type F8T2, PMMA and Al were used as the semiconductor layer, the dielectric layer and the gate, respectively.

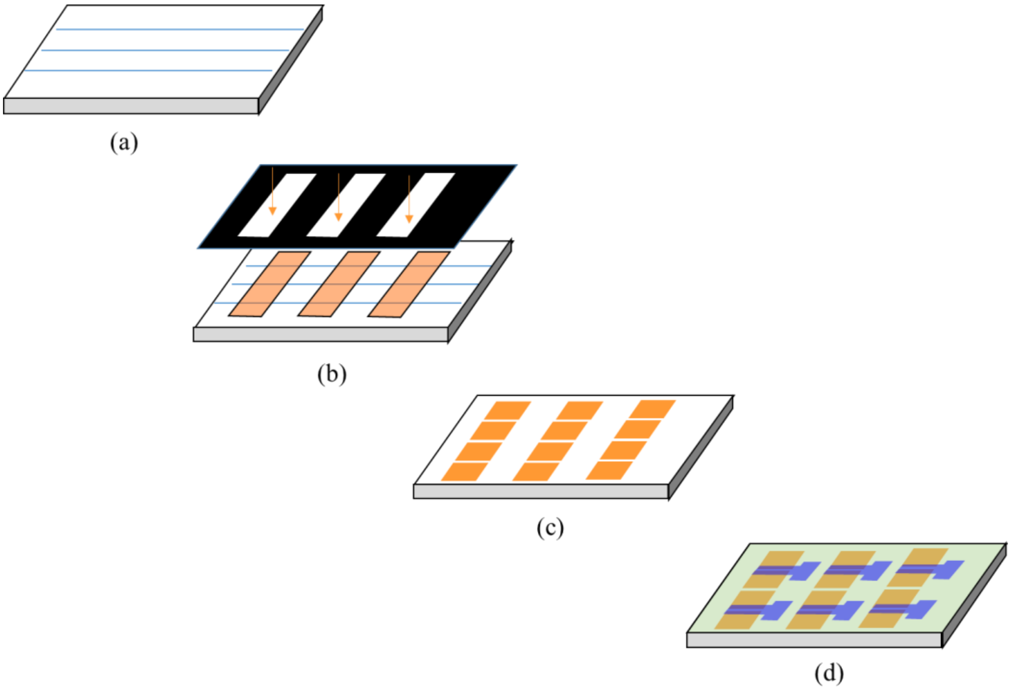

Figure 5.14. The top-gated F8T2 OFET fabrication process
(a) Pattern PS wires on silicon dioxide substrate
(b) Au/Cr deposition by shadow mask
(c) Dissolve PS wires by DCB (lift-off)
(d) Deposition F8T2 semiconductor, dielectric layer and gate

Figure 5.15. The SEM image of the final transistor channel formation after the gold electrodes deposition and lift-off step.

Figures 5.16 and 5.17 display the device original transfer curve and the logarithmic transfer curve, respectively. The active layer material in this device was p-type organic semiconductor as well, so the testing method was same as for the PQT-12 OFET; the drain bias was set at -30 volts and the range of gate bias value was set from 20 volts to 60 volts. From Figure 5.17, we can see that the device switched "on" at around 0 volt and "off" when the gate voltage was -60 volts. So the on/off current ratio is about 10^5 and the hole mobility is $6.9 \times 10^{-4} \mathrm{cm}^2/\mathrm{Vs}$ as calculated by the original charge carrier mobility formula which has been introduced in Chapter 2. The device output curves with corresponding gradient gate voltages is shown in Figure 5.18. Different with pervious device testing results, the output beginning point was shifted from 0 to about -5 volts on the drain voltage axis. This means that at the beginning the hole injection is in a difficult situation. The reason for this phenomenon was because the polymer crystallized on the two types of material, gold and silicon, at the same time. As we known, the different materials have different surface energies which can affect the polymer crystallization orientation and degree as the initial energy they provide are different. Actually, the surface energy of silicon dioxide is lower than Au. In the molecule crystallization process, molecular crystals are tending to stand on the dielectric material surface, while tiling up on the metal surface. As result, it was difficult to keep the orientation of material crystallization consistent on both the Au and silicon surfaces during the annealing process, which results in the contact resistance increasing, Furthermore, it also increases the difficulty of hole injection into the transistor channel. The related study about organic molecule crystallization orientation will be introduced in Chapter 6.

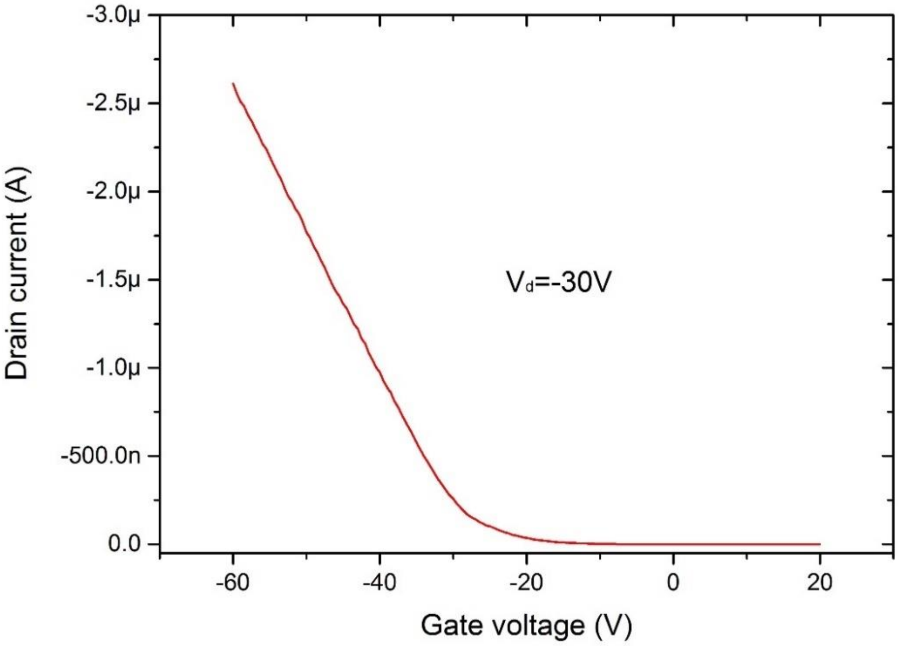

Figure 5.16. The transfer curve of **poly(9,9-dioctylfluorene-alt-bithiophene)** (F8T2) top-gated field effect transistor

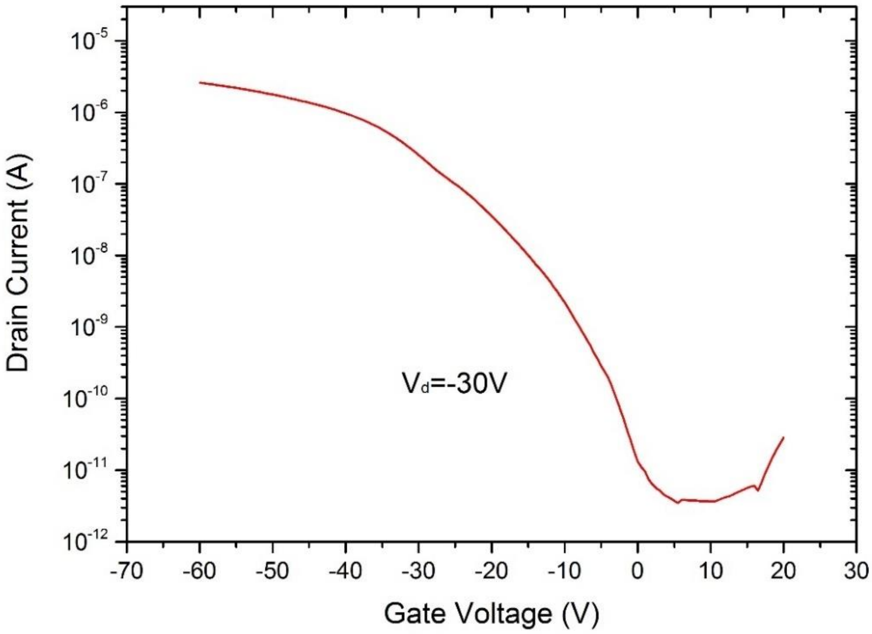

Figure 5.17. The logarithmic transfer curve of **poly(9,9-dioctylfluorene-alt-bithiophene)** (F8T2) top-gated field effect transistor

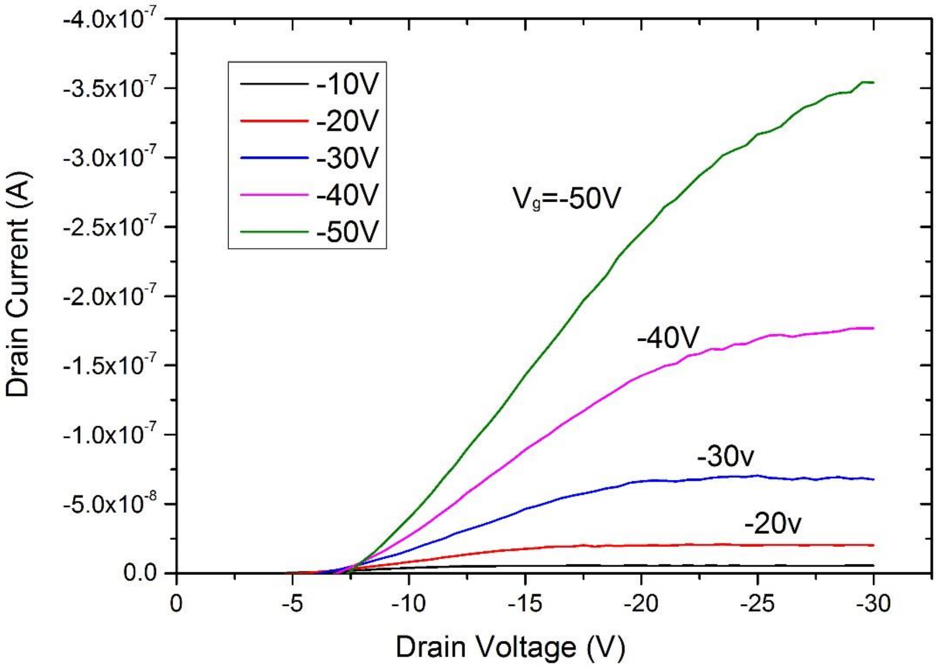

Figure 5.18. The outputs curve of **poly(9,9-dioctylfluorene-alt-bithiophene)** (F8T2) top-gated field effect transistor

5.3 Organic Electro-Chemical Transistor (OECT) fabrication

In Chapter 2, the previous achievements by other scientists and engineers have been reviewed. To further demonstrate the potential of our process, we fabricated arrays of devices with individually electrically addressed wires of the active materials. Poly(3,4-ethylenedioxythiophene)-poly(styrenesulfonate) (PEDOT:PSS)-based electrochemical transistors were chosen because PEDOT:PSS is sufficiently robust to the photolithography process, and such a device has promising applications for electrophysiological recording [2].

5.3.1 Thin film organic electro-chemical transistor

PEDOT:PSS films are usually utilized as a hole injection layer in the organic electronic device [3]. Different from other organic semiconductor materials, PEDOT:PSS is a water-based solution. When the PEDOT:PSS is spin-coated on a substrate, the liquid film transfers to the solid as the water is evaporating. When putting the sample into water, the whole material film can be peeled off from the substrate. This experiment proved that once the PEDOT:PSS material is cross-linked through annealing, it cannot be dissolved by water again. Therefore, the patterning method which I previously used was unsuitable for PEDOT: PSS because of this unrepeated dissolution property. The PEDOT:PSS (Clevios PH-1000) water-based suspension was received from Heraeus company. To enhance the conductivity, the aqueous PEDOT:PSS solution is modified by adding 20% ethylene glycol (received from Sigma-Aldrich) to improve the conductivity. By this method, the conductivity of the film can be increased by more than two orders of magnitude [4]. Additionally, 1% Triton-X100 (Sigma-Aldrich) was added to reduce the surface tension and to obtain a highly uniform film.

Nowadays, the FET-based biosensor has attracted great attention because it can capture and convert biological signals to electrical or optical signals. Due to PEDOT:PSS's extremely robust and water solubility characteristics, it may be an idea material for biotransducer device fabrication. Normally, the biosensor is classified in several types; one of them is electrical-chemical biosensor. This kind of sensor also contains three electrodes; the structure is almost same as a transistor. The PEDOT:PSS based thin film electro-chemical transistor fabrication process was quite similar to the top-gate F8T2 transistor. But, there are two differences compared with the top-gate F8T2 transistor: 1) The substrate used here is glass (received from Corning Company) and 2) The dielectric material is replaced by PBS buffer solution. The specific fabrication process is demonstrated in Figure 5.19.

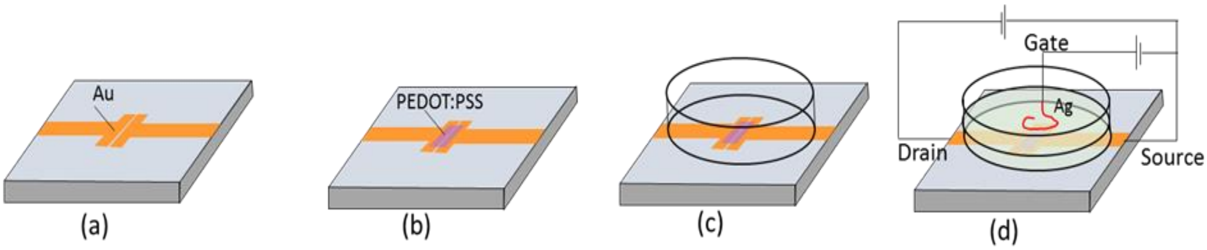

Figure 5.19. The electro-chemical transistor fabrication process
(a) Gold electrodes deposition
(b) PEDOT:PSS deposition and annealing (140°C, 1hour)
(c) Attaching plastic ring
(d) Filling in PBS solution

The full name of PBS is phosphate buffer saline and it is usually employed as a cell culture solution. The main positive ion in this solution is Na^+. The purpose of using this solution will be explained later. The device measurement method has been presented in Figure 5.20.

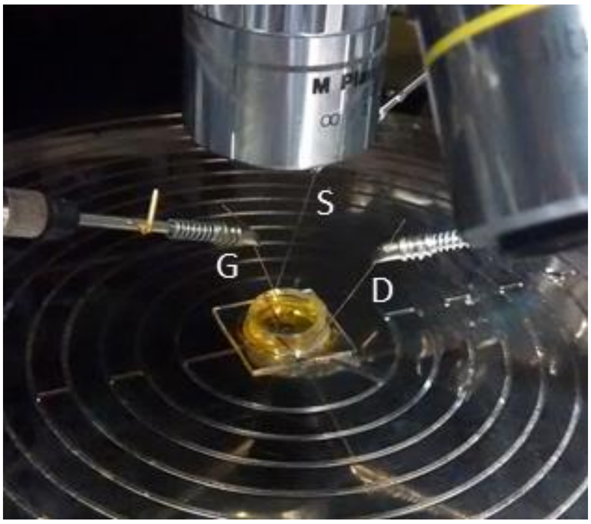

Figure 5.20. The electro-chemical transistor measurement by probe station

During the measurement, the device performance was different from previous devices. Through analysis, that was determined to be because the Na ions were found to be injected into the PEDOT:PSS thin film and combined with PSS^{-} when a positive gate bias was applied. The concept is presented in Figure 5.21. This de-doping process decreases the conductivity of the active layer.

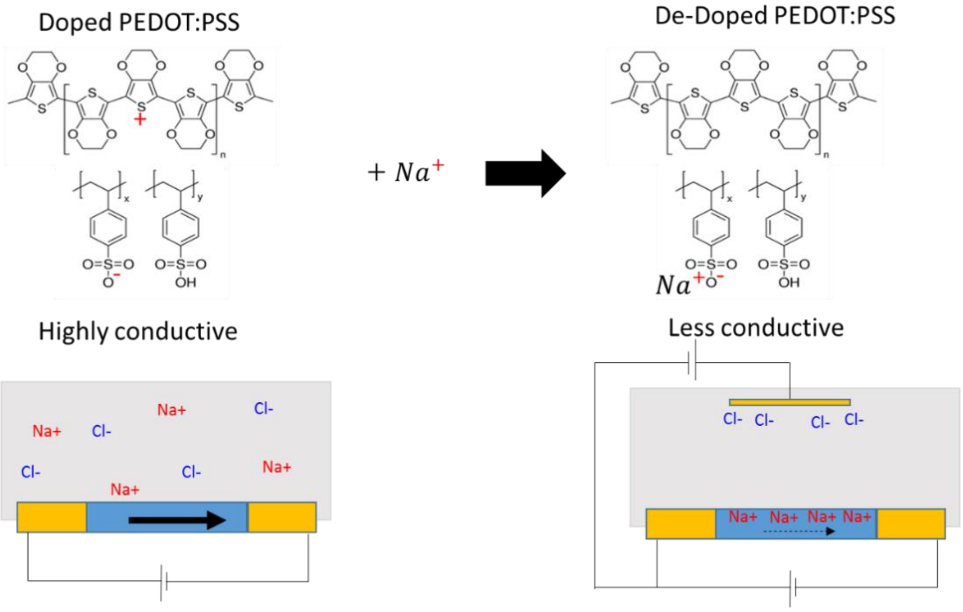

Figure 5.21. The de-doping process of PEDOT:PSS thin film

The device transconductance and output curves are presented in Figure 5.22 (a) and (b), respectively.

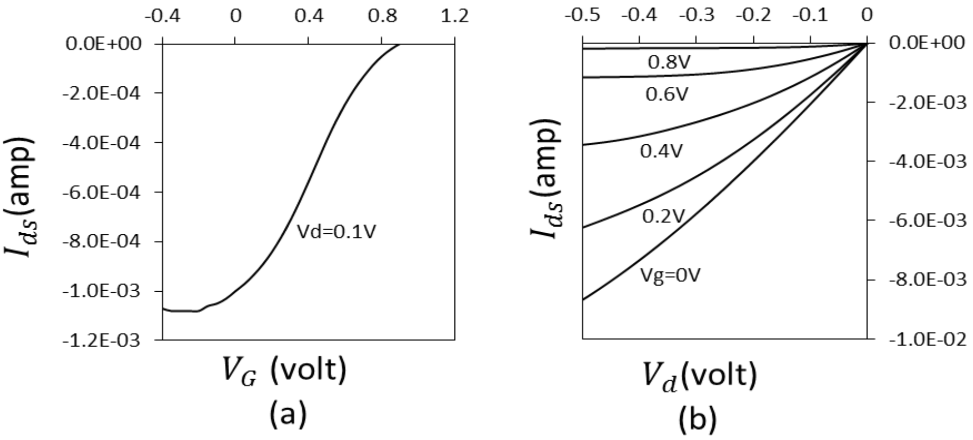

Figure 5.22. The PEDOT:PSS based elector-chemical transistor performance (a) Transconductance curve; (b) The current output under different voltages

From the results, two advantages can be identified in this device. One is that only a small voltage is needed to drive this device; the other is that the device is a highly sensitive ion detection. Both of these advantages satisfy the requirements of a biosensor device.

5.3.2 Geranium wires fabrication by patterning transfer technique

We have developed another patterning technique especially for PEDOT:PSS wires array fabrication. Preliminary experiments were carried out to prove the feasibility of our idea. First, a 100 nm thickness of germanium (Ge) was deposited on well cleaned silicon substrate by thermal evaporation. Then, a 50 nm-thick PS film was spin-coated onto the germanium film, and the PS line structure was created using our patterning method. After dry-etching entirely through the germanium film using CF_4 plasma, the area which was uncovered by PS wires was removed. The PS wires function are equivalent to a mask here. The PS was removed with toluene and finally the array of germanium wires were left on the substrate. Figure 5.23 and Figure 5.24 show the SEM images of the Ge nanowires.

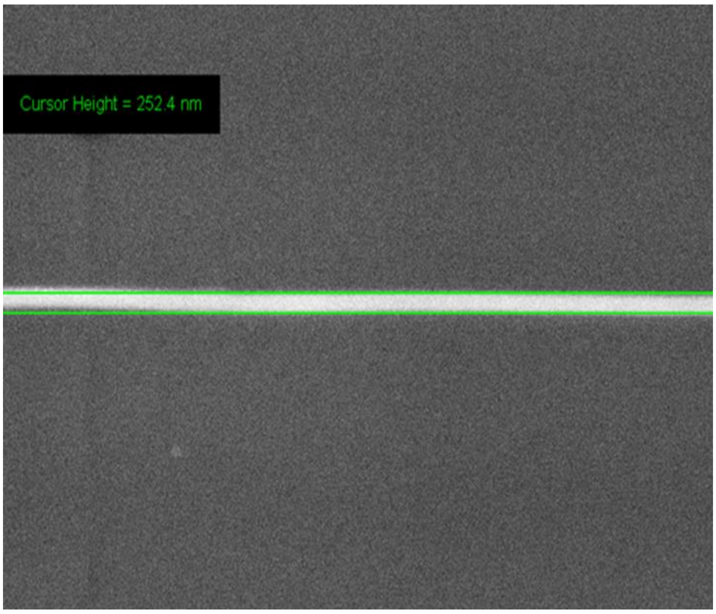

Figure 5.23. The SEM image of a single Ge wire

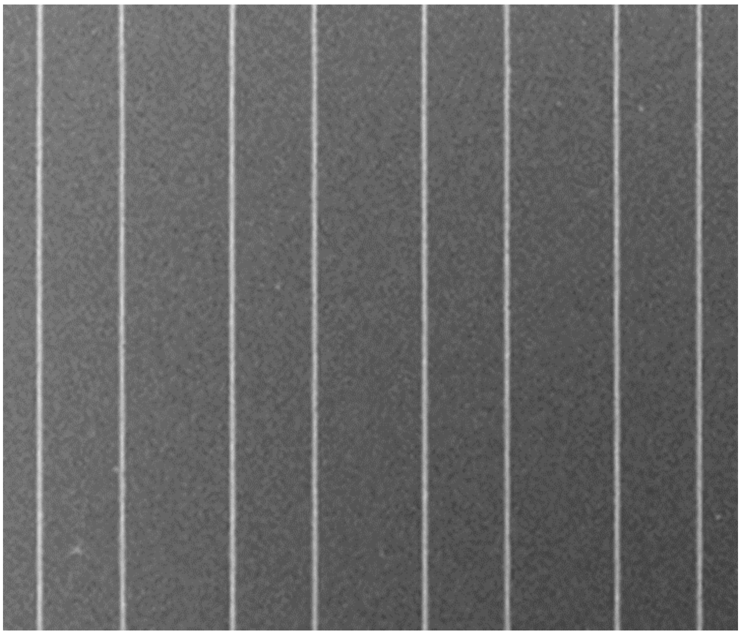

Figure 5.24. The SEM image of a Ge wires array

The success of this geometry patterning transfer trial provides a positive basis for the PEDOT: PSS based transistor manufacture.

5.3.3 The PEDOT:PSS wires array fabrication

In the device fabrication process, the first step is patterning PEDOT:PSS wires by utilizing the above technique. The PEDOT:PSS wires were produced through pattern transfer of a line-pattern into PEDOT:PSS film using the generated PS lines as a mask through a process similar to that used for the germanium wires fabrication. A 90 nm-thick PEDOT:PSS film was formed by spin-coating onto SiO_2 (300 nm)/Si substrate and subsequently annealing it at 140°C for 1 hour. A 100 nm PS film was then spun-coated over the PEDOT:PSS film, and PS lines were created using our developed method. After plasma etching using a gas mixture of CF_4 and O_2 (1:1), the sample was rinsed with toluene to remove the PS lines. The PEDOT:PSS wires array was created successfully. This whole material patterning transfer process have been illustrated in Figure 5.25.

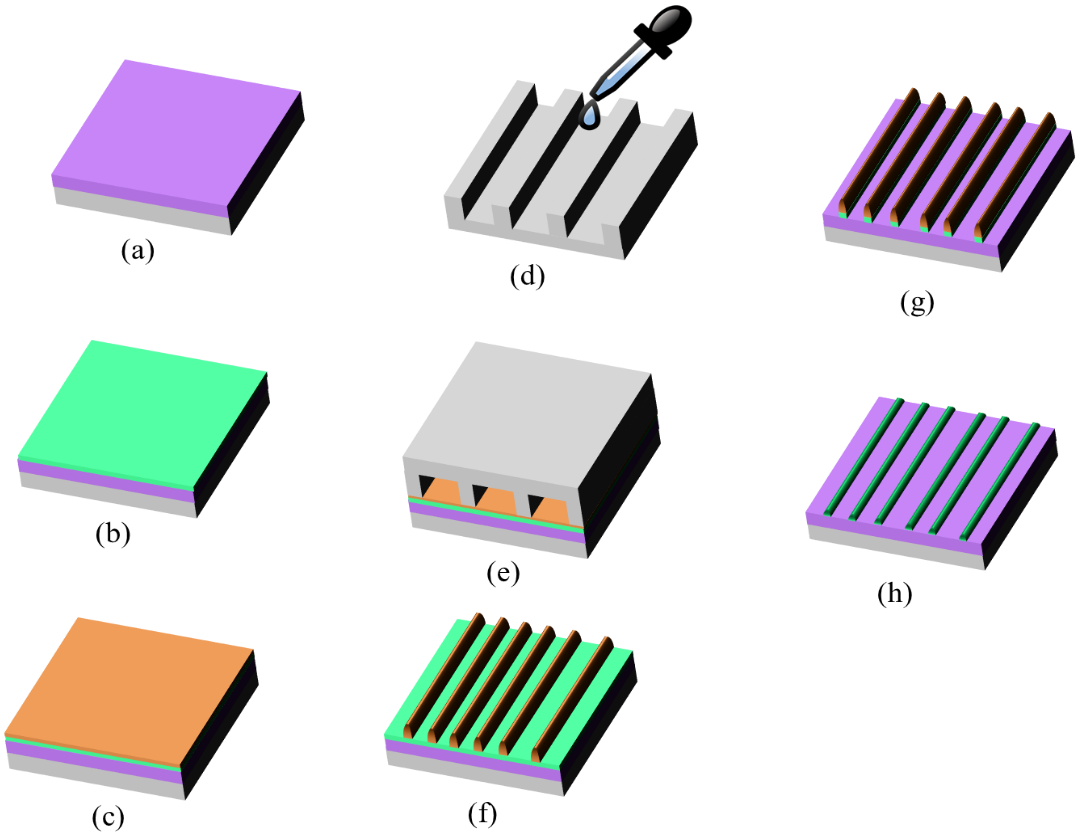

Figure 5.25. The material structure transfer patterning process
(a) Substrate preparation
(b) Spin-coating PEDOT:PSS and annealing
(c) Spin-coating PS on PEDOT:PSS thin film
(d) Small droplet of solvent on PDMS template
(e) Patterning PS lines
(f) PS lines array formation
(g) Plasma etching of PEDOT:PSS thin film
(h) Removing PS lines

Figure 5.26 below demonstrates a part of the PEDOTS:PSS wires array.

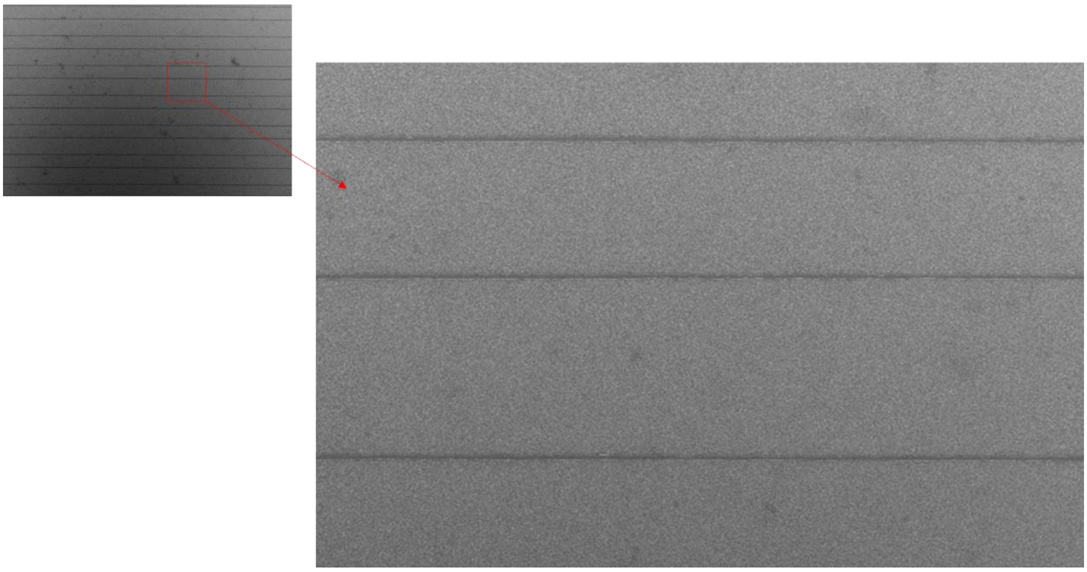

Figure 5.26. The SEM image of PEDOT:PSS wires array

Under SEM observation, the width of a single wire is about 670 nm, nearly half micrometer. The array of PEDOT:PSS wires acquired by the patterning transfer technique from array of PS lines was a significant achievement in my series of experiment.

5.3.4 The Organic Electro-chemical PEDOT:PSS field effect transistor fabrication

Continuing the previous work, the following step was to make gold source and drain electrodes by using a mask aligned on the PEDOT:PSS wires and subsequent optical lithography and lift-off. Figure 5.27 displays the wires array with electrodes attached image.

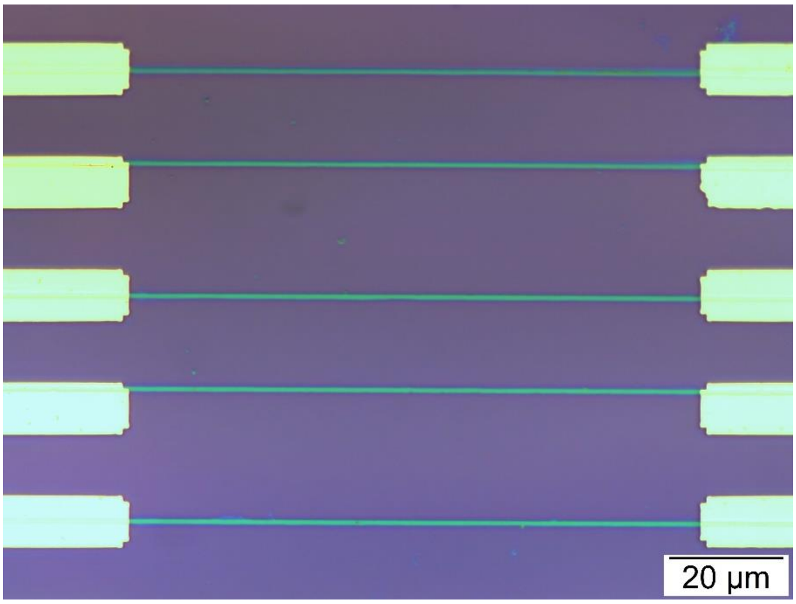

Figure 5.27. The PEDOT:PSS wires array with two gold electrodes touch at both sides

A silver conducting wire and 0.1 M NaCl aqueous solution were used as the gate electrode and electrolyte, respectively, during device characterization. A millimetre-sized PDMS frame was physically attached on the sample surface to confine the electrolyte. In the measurement, a small gate and drain bias (less than 0.5 V) was applied on the transistor. The device transconductance curve and logarithmic curve are shown in Figure 5.28 and Figure 5.29, respectively.

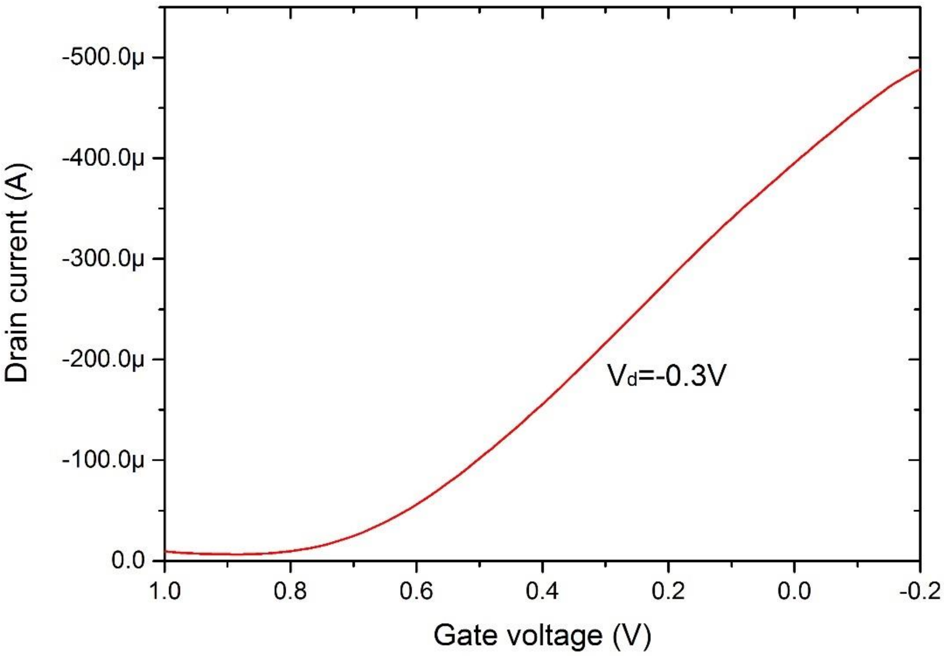

Figure 5.28. The transconductance curve of PEDOT:PSS wires array transistor

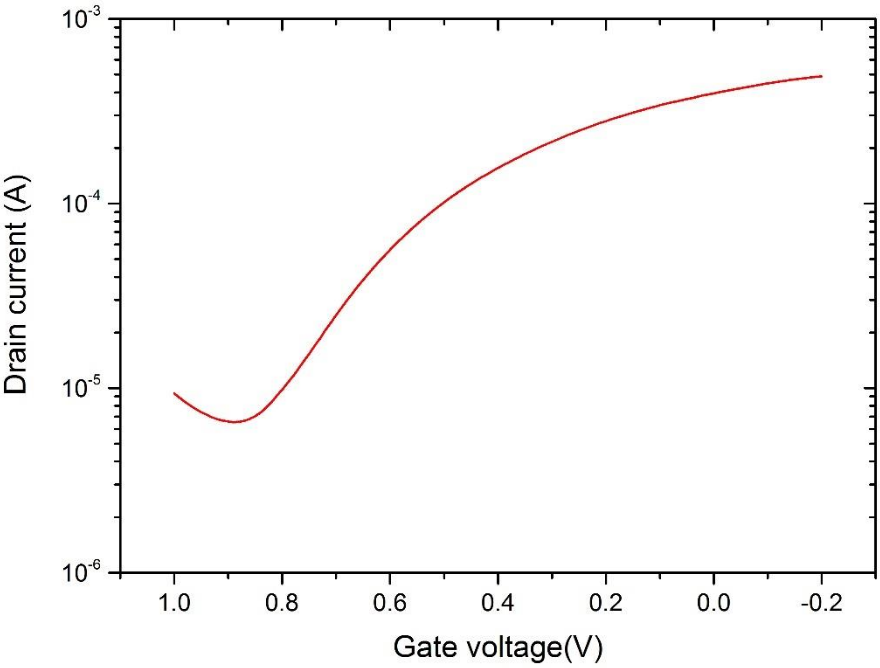

Figure 5.29. The logarithm of transconductance curve of PEDOT:PSS wires array transistor

From both figures, we can notice that different with previous organic field-effect transistor characteristics, the drain current decreased as the gate voltage increased, i.e., working with the depletion model, when a positive bias was applied on the gate electrode some of the negatively charged PSS^- was balanced by Na^+in PEDOT:PSS wires. Furthermore, compared to the polymer field-effect transistor, the PEDOT:PSS transistor just needs a small voltage, below 1 volt, to drive and control it. In addition, the controlling mechanism was through adjusting the concentration of cations in the solution, also different with traditional OFETs. A series of output curves along with the gate bias variation is shown in Figure 5.30.

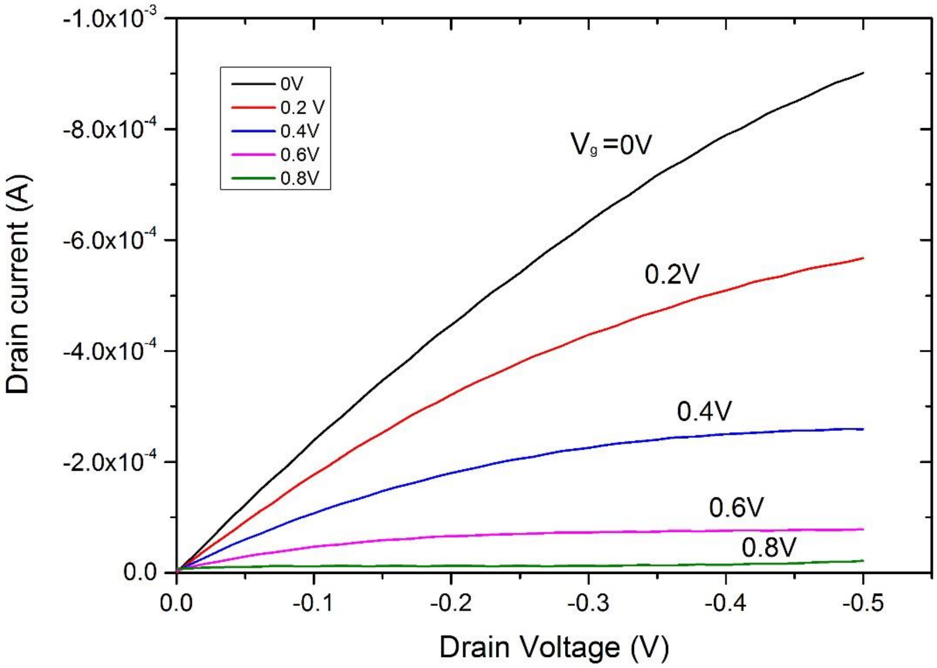

Figure 5.30. The output curves of PEDOT:PSS wires array transistor

From this figure, it is clear that the current outputs varied dramatically when the gate bias was gradually decreased. The current changed about one order of magnitude while the gate voltages just changed 0.8 volts. The same current variation in polymer-based transistor at least needs tens of volts change on gate electrodes. This characteristic proofs the PEDOT:PSS-based transistor is more sensitive compared to polymer-based transistor. A small voltage changes result in a large current output varies, this advantage may be possible to use in biosensor devices because the biological signal variation sometimes is quite small and needs a sensitive device to capture it; in addition, the signal output of PEDOT: PSS is strong enough to drive and electronic device.

To better understand the performance of the device, the single wire transistor measurement also has been implemented. During the measurement process, the drain voltage was 0.3 V as well. Under the same testing circumstance, both transfer curve and logarithmic transconductance curve are shown in Figure 5.31 and Figure 5.32, respectively. The output curves with different gate biases of a single PEDOT:PSS wire transistor are shown in Figure 5.33, from which we found that the output current of the single wire transistor was reduced by two orders of magnitudes compared that of to the wires array transistor.

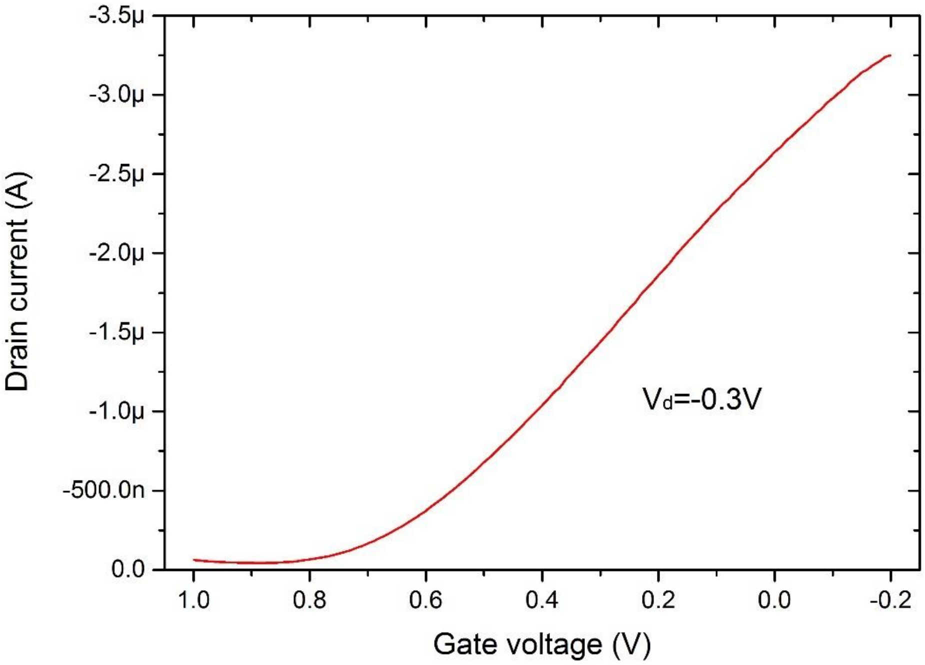

Figure 5.31. The transconductance of a single PEDOT:PSS wire transistor

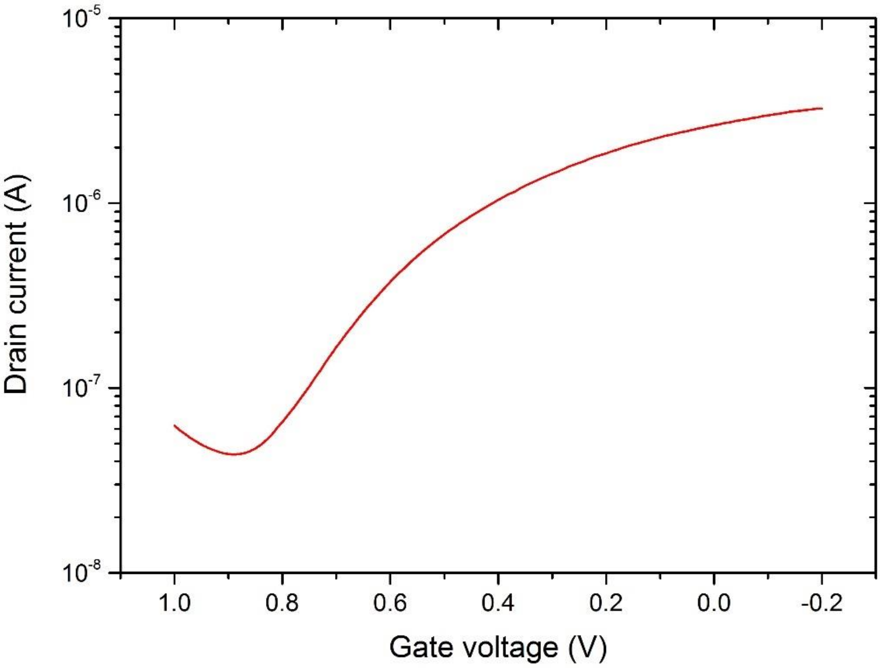

Figure 5.32. The logarithm transconductance curve of a single PEDOT:PSS wire

transistor

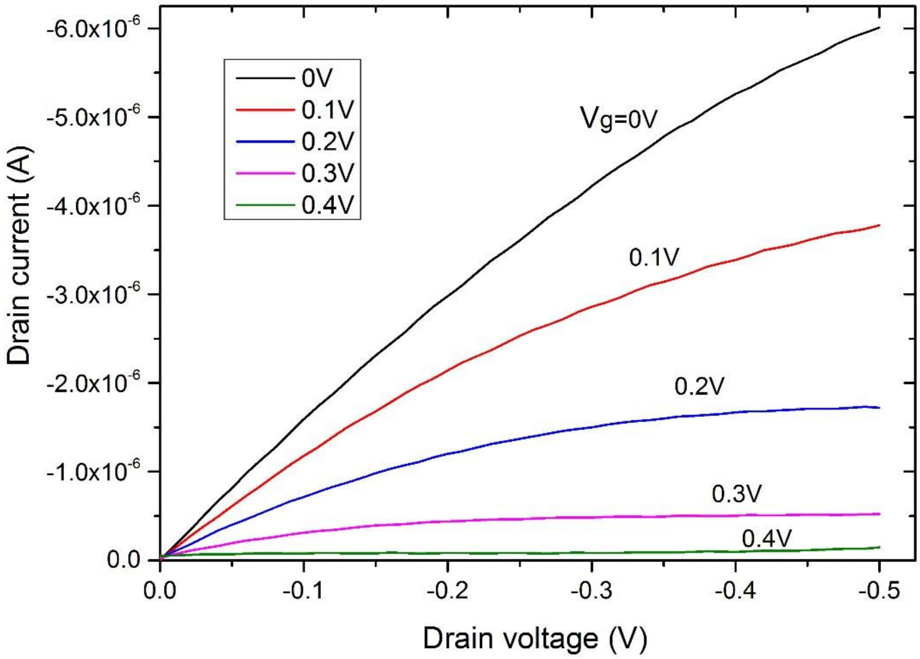

Figure 5.33. The output curves of single PEDOT:PSS wire transistor

5.3.5 Holes on PEDOT:PSS wires array

As we known, in cell biology research, the communications between cells depends on a bioelectrical signal, or bio-signal, which is sometimes generated by the ion cell membrane permeability variation when it receives stimulation. In my previous experiment, the PBS solution was used as buffer material in PEDOT:PSS transistor device fabrication. This kind of solution can be also employed as a tissue cell culture medium. Since the electro-chemical transistor contains several advanced characterizations, such small on/off ratio and small voltage drive, it may be possible to use it in cell signal detection, especially for cancer cell research. Based on this idea, a photoresist film was spin-coated on the PEDOT:PSS wire array and then exposed by UV light under a shadow mask which has been introduced in Section 5.2. (Figure 5.3). Through development, a series of small holes was finally accurate formed on each PEDOT:PSS wire; see Figure 5.34. Those tiny holes on the wire can be used to store liquid, such as electrolyte or cell culture medium. In this way, culturing a cell in a hole and measuring its signal is possible. Besides, the measurement result in a single-wire transistor revealed that the device shows an excellent stability even when doping and dedoping occurs in different areas, which is crucial point for high-resolution sensing, like bio-recording, where the ion concentration varies in the subcellular domain. Both transconductance and logarithmic transconductance curves have been demonstrated in Figure 5.35 and 5.36, respectively. The output curves have been displayed in Figure 5.37. All the measurements were carried out under the same environment as previously and the results were almost the same as those for the single wire transistor in last experiment.

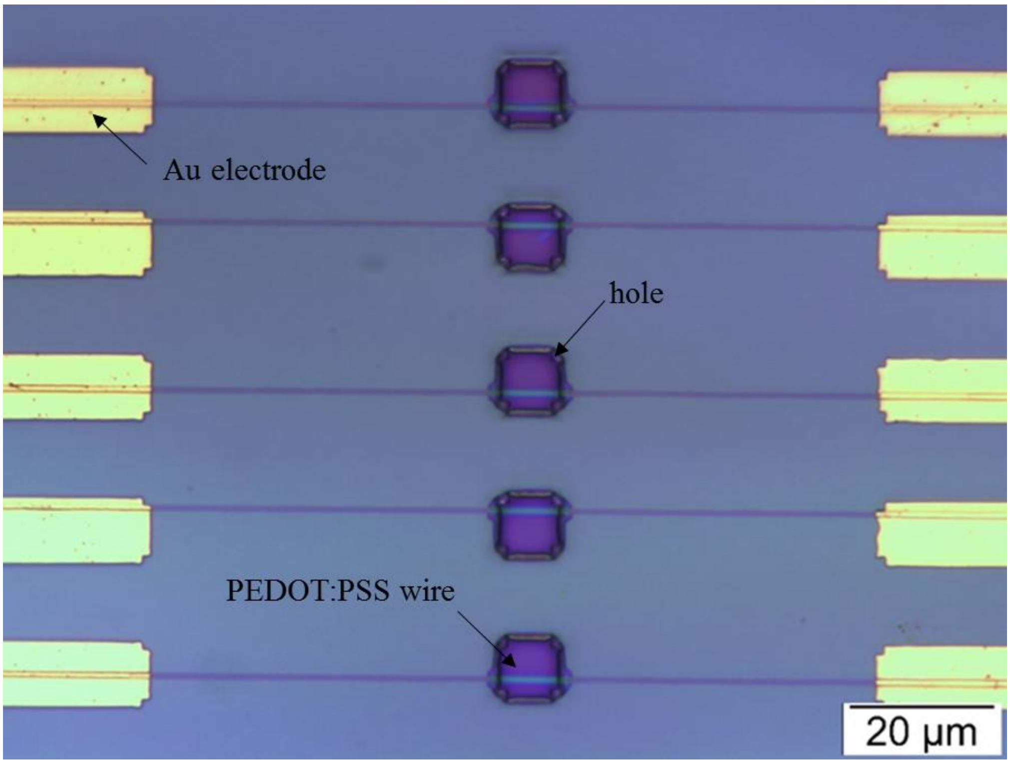

Figure 5.34. The exposed holes on each of PEDOT:PSS wires

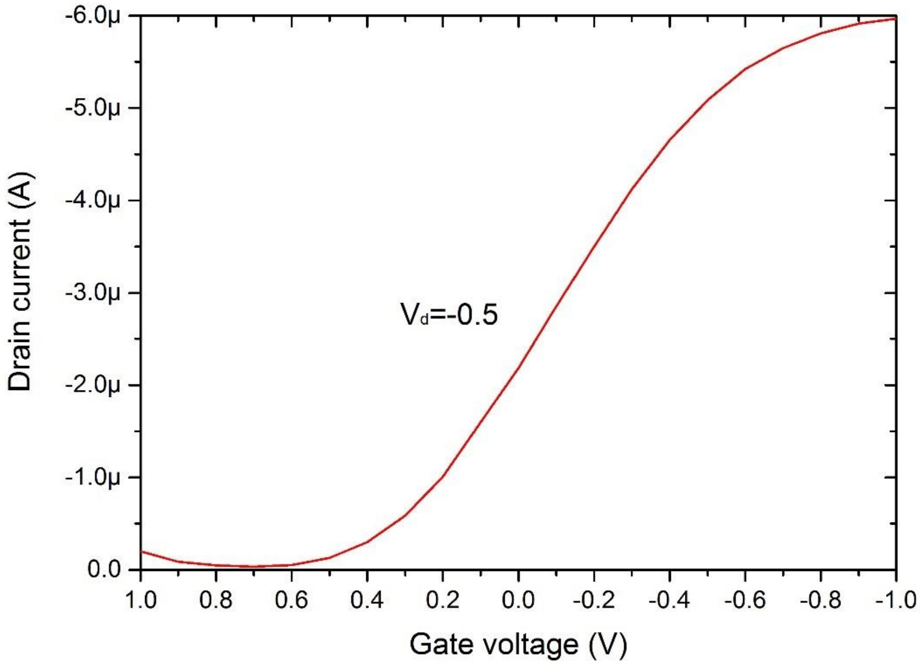

Figure 5.35. The transconductance of a single PEDOT:PSS wire transistor

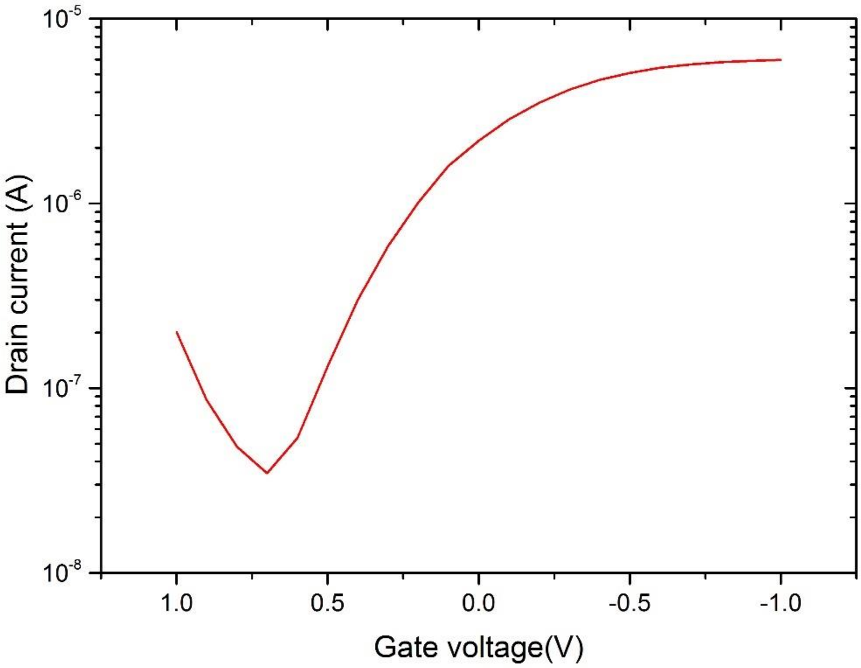

Figure 5.36. The logarithm transconductance curve of a single PEDOT:PSS wire transistor

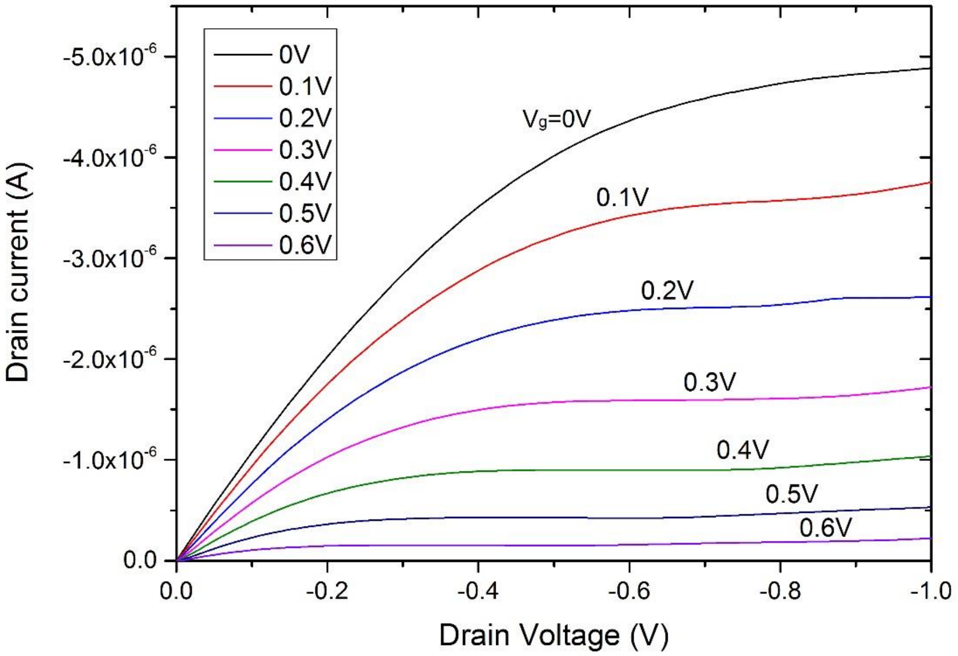

Figure 5.37. The output curves of a single PEDOT:PSS wire transistor

5.4 Summary

In this chapter, four organic field-effect transistors, one n-type, two p-types and one electro-chemical type, have been fabricated successfully, all of these devices are working very well. The patterned organic semiconductor wires greatly enhance the efficiency of manufacture, in this way, lots of OFET can be fabricated at one time on a silicon wafer. Meanwhile, this method avoids the optical photolithography; thereby, the reducing the cost. The single PEDOT:PSS wire transistor output current can be tuned by a small gate bias in a electrolyte solution; this was a novel achievement in this series of experiment. It provides a possible fabrication method for FET-based biosensors.

Reference

1 Chen, W. N., Chu, D. P. & Li, S. P. Air stable complementary polymer circuits fabricated in ambient condition by inkjet printing. *Organic Electronics* **13**, 98-103, (2012).

2 Khodagholy, D. *et al.* In vivo recordings of brain activity using organic transistors. *Nat Commun* **4**, 1575, (2013).

3 Groenendaal, B. L., Jonas, F., Freitag, D., Pielartzik, H. & Reynolds, J. R. Poly(3,4-ethylenedioxythiophene) and its derivatives: Past, present, and future. *Advanced Materials* **12**, 481-494, (2000).

4 Ouyang, J. *et al.* On the mechanism of conductivity enhancement in poly (3, 4-ethylenedioxythiophene): poly (styrene sulfonate) film through solvent treatment. *Polymer* **45**, 8443-8450, (2004).

Chapter 6

Organic semiconductor materials crystallization and spectrum absorption

6.1 Introduction

This chapter reports two experiments. In the previous chapter, the F8T2-based organic field-effect output curves attracted my attention due to the fact that the current output point drifted. An explanation that I gave at that moment was that because of the different material surface energies the molecule crystallization orientation cannot keep consistent during the annealing process. To better understand and explain this phenomenon, an experiment of a small organic molecule material crystallization on two different types of substrates was carried out in order to observe and investigate the organic semiconductor material crystallization characteristic. The reason that I chose a kind of organic small molecule semiconductor material instead of polymer material to do this experiment was because the former is easier to observe through an optical microscope to acquire crystalline geometry images. It is also well known that organic small molecule semiconductors have much higher charge carrier mobility than polymer semiconductors because the high degree of molecular packing/ordering is favourable for charge transportation [1,2]. The investigation results of the organic small molecule material crystallization at different annealing temperatures will be presented and the related initial activation energy for that crystal growth requirement has been calculated and will be introduced in this chapter as well. Another experiment was about polymer semiconductor spectrum absorption after both PQT-12 and polyera materials were annealed at different temperatures.

6.2 The experiment's purpose and material preparation

The synthesis process of nickel-tetrabenzoporphyrin (NTBP) precursor can be found in reference [3]. Usually, for the organic small molecule, the vacuum sublimation process has been widely used to deposit thin film materials on the substrate [4,5], however, to realize low-cost organic electronic products the vacuum processes have to be replaced by solution processes if possible. Thus, the NTBP was prepared in chloroform solution at 10 mg/ml. It is well known that if we want to improve a device's performance, one of the key factors we have to think about is acquiring a high-quality semiconductor layer. Therefore, in the annealing procedure, choosing a proper temperature and time to get the best degree of molecule crystallization is an effective method to enhance the active material quality. Here, we report an experimental study on the recrystallization of NTBP [6,7] from its amorphous precursor films, deposited by spin-coating on different substrates. Tetrabenzoporphyrin is a promising material with high charge mobility for application in printed electronics [6]. The dynamic process of crystallization of NTBP was investigated at the crystal nucleation and growth stages for fabrication of the crystalline thin films with the desired molecule orientation.

For the spectrum absorption experiments, the PQT-12 and N2200 were chosen and their solution preparation methods have been presented in Chapter 4.

6.3 The nickel-tetrabenzoporphyrin (NTBP) recrystallization

During the thermal treatment, the precursor film converts the amorphous precursor into crystalline NTBP. This procedure is demonstrated in Figure 6.1 below.

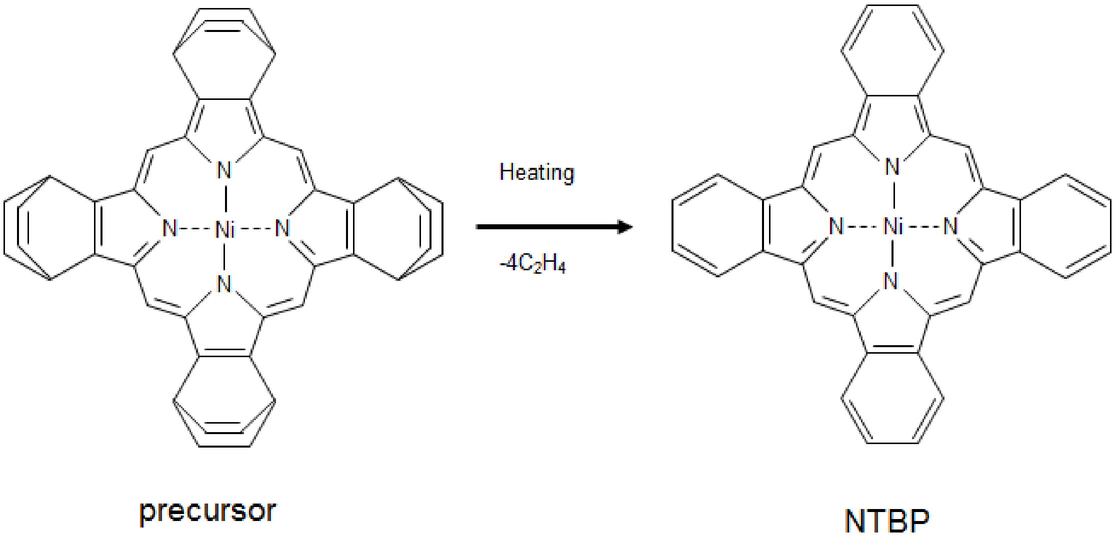

Figure 6.1. The crystallization of solution processable amorphous tetrabenzoporphyrin films

6.3.1 Recrystallization on bare glass and polyimide layer glass substrate

The precursor films were formed by spin-coating from a chloroform solution onto a bare glass substrate and subsequently baking at 60 °C for 30 min. The substrate was treated with oxygen plasma after sequential cleaning with acetone and isopropanol to remove any organic contamination. For all samples in this study, the precursor film thickness was about 50 nm. The structural change was monitored by optical microscope because the optical contrast is excellent between the film crystalline and amorphous phases. A digitally controlled heating system was connected to the microscope and optical images were taken from the top side of the transparent samples. The heating ramp was 30°C/min and the time counting started immediately when the programmed annealing temperature was reached. Other techniques we also have used, like atomic force microscope (AFM), but it did not give clear information due to the poor contrast of the morphologies in such thin films. Figure 6.2 (left) shows the recorded sequential images of the crystal nucleation and growth process under 205°C annealing on the glass with the change of time. The irregular disk-like crystallites grew on the glass substrate under this time-dependent annealing procedure and finally formed "mosaic" crystalline structures on the glass.

For comparison of the material's preferential orientation during the crystallization process, a layer of 1 μm thickness polyimide film on glass substrates was deposited by spin-coating from N-methyl-2-pyrrolidone (NMP) solution (referred as PI substrate) and baked at 250°C for 30 min.

Then, the NTBP solution was spin-coated on the PI substrate. The time counting and observation began when the temperature reached 200℃. Different with the crystallization on a glass substrate, the crystallites appear to be in ellipsoidal form and gradually evolve to a leaf-like shape due to the developed fractal growth in the late stage of crystallization as illustrated in Figure 6.2 (right).

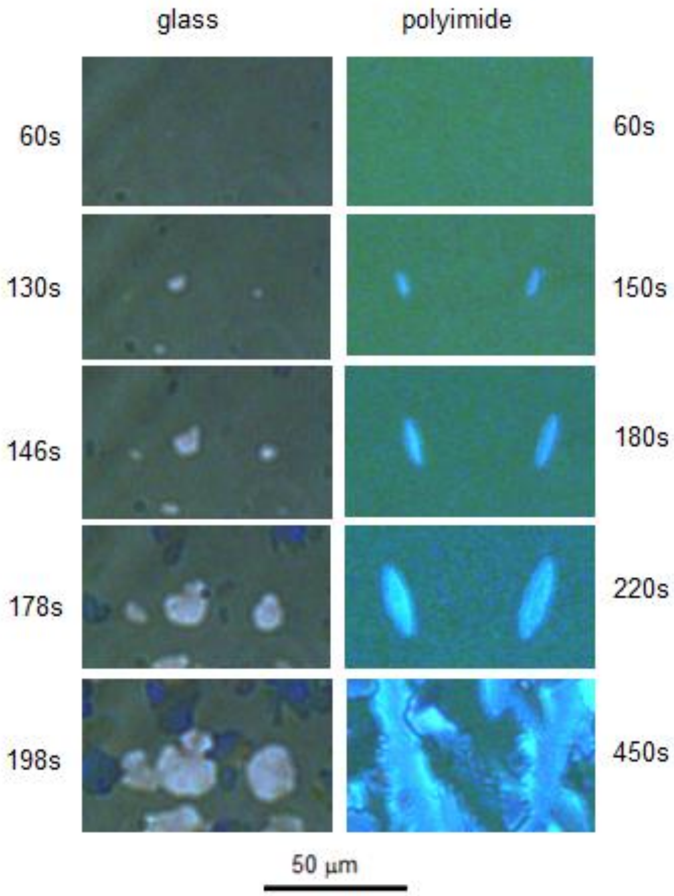

Figure 6.2. Evolution of the crystal nucleation and growth of NTBP on the glass substrate at 205 °C (left) and on the PI substrate at 200 °C (right).

The images of both "leaf"-like structures on PI substrate and the "mosaic" crystalline structures on glass are illustrated in Figure 6.3 below.

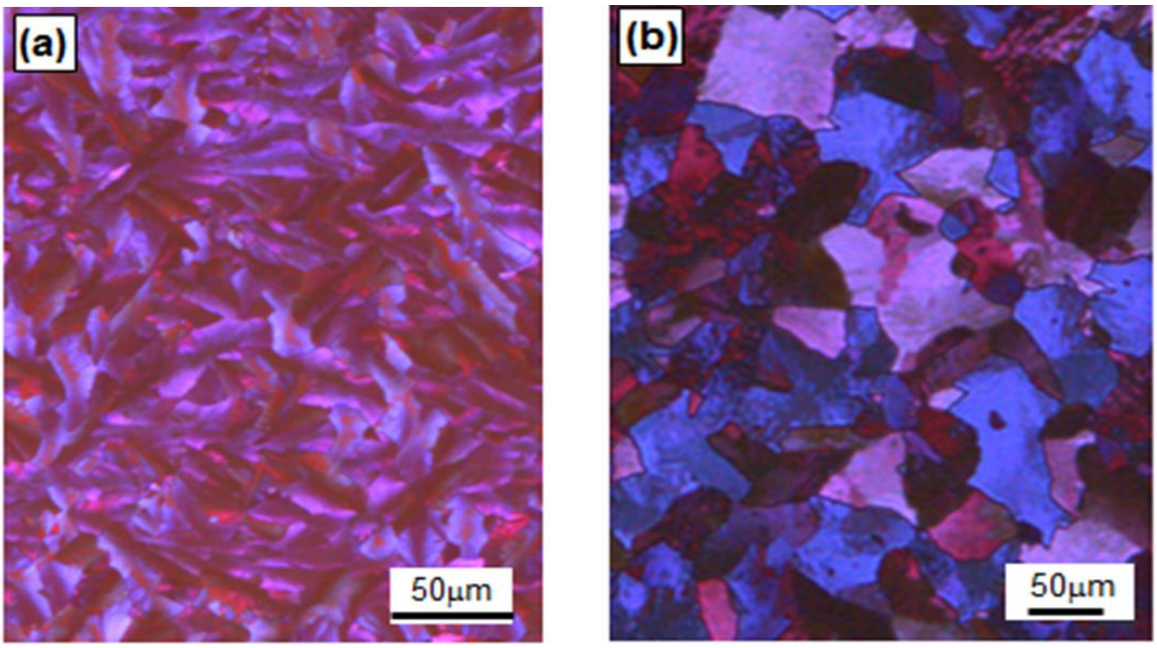

Figure 6.3. The optical images of the "leaf"-like and "mosaic" crystalline structures on (a) the glass and (b) PI substrates.

The variation of the individual crystal size formation with time on these two substrates was measured during the annealing. Figure 6.4 (a) and (c) shows the results taken from the crystals grown on the glass substrate under 205°C and the PI substrate under 200°C, respectively. Average radius was measured for the disk-like crystals, while half the length of the axis (HLA) for both major and minor axes were measured for the ellipsoids. The growth speed (slope of the line) of the crystals on the glass substrate does not change, while on the PI substrate it changes on both axes of the ellipsoids after an initiation stage (as indicated by the arrows). For all the samples observed under a constant annealing temperature the measured speed of crystal growth is constant regardless of which crystal was chosen. The difference in the initiation time of nucleation only causes a line shift as shown in Figure 6.4 (a) and (c). The growing speed of the crystal (V) for different annealing temperatures (T) from 190 °C to 220 °C was measured.

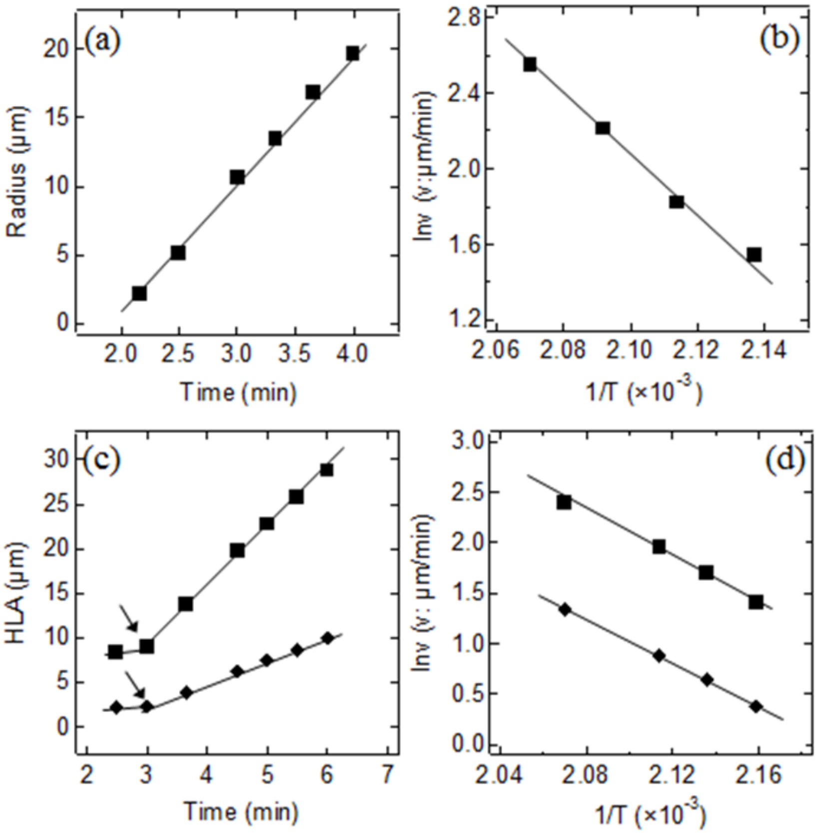

Figure 6.4. Time dependence of crystal sizes and $\log_e$ V ~ 1/T plot taken from the samples on a glass substrate under 205 °C [(a) and (b)] and a PI substrate under 200 °C [(c) and (d)], respectively.

Here, equation (5) in Chapter 4 can be utilized again to show the relationship between the crystal growth speed and temperature elevation. An activation energy Q can be obtained by plotting $\log_e$ V against 1/T according to this equation. Figure 6.4 (b) and (d) shows the experimental $\log_e$ V against 1/T plots from the two types of samples. The obtained activation energy from the samples on the glass substrates is E^G= 1.27 eV, while for the PI substrates they are E_a^P = 0.99 eV and E_b^P =0.94 eV for the major and minor axes of ellipsoid, respectively, with an average of E^p =0.965 eV. For evaluating

E_a^P and E_b^P only the linear part as shown in Figure 6.4 (c) was used. The sudden change for the crystal growth speed in Figure 6.4 (c) can be explained by the facet-roughing Kosterlitz–Thouless (KT) transition as observed previously [8]. The reason of the observed KT transition here is not clear. It might be caused by a tensile stress induced by a volume reduction of the crystalline phase in comparison to its amorphous precursor. In order to understand the crystalline structure, Jerzy Kanicki's group [6] have had measured the crystallized film by X-ray diffraction (XRD) analysis. The measurement result has been shown in Figure 6.5. The crystallographic structure of the NTBP is monoclinic with unit cell parameters are a= 1.236 nm, b= 0.6578 nm, c= 1.519 nm, and β = 100.62°. Numerous diffraction peaks from the samples on the glass substrate indicate that the film displays no preferential crystal orientation. On the other hand, the film on the PI substrate shows a preferential crystal orientation with (001) lies in the film plane. The broad "hump" characteristic of the spectrum is caused by the underlying PI film. The broad "hump" from θ=5° to 30° agrees well with result obtained from amorphous polyimide film in literature [9]. The random nature of the microcrystals observed on the samples on the glass substrates is similar to that observed for TBP crystallized on silicon substrate [6].

A close look at the crystal formed at the initial stage of crystallization (i.e. the primary crystal) on a PI substrate is shown in Figure 6.6 (a) and a schematic drawing of it is given in Figure 6.6 (b). The well-defined flat facets of the primary crystals support the existence of a KT transition. The preferential orientation of NTBP film on the PI substrate can be understood if a local polymer chain order as shown in Figure 6.6 (c) exists on the PI film surface which provides a template for initiating the nucleation of NTBP.

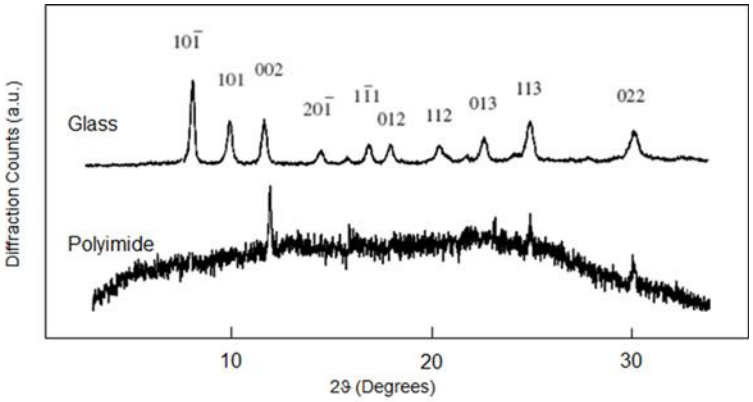

Figure 6.5. The X-ray diffraction (XRD) patterns of the crystalline films on glass (top) and PI (bottom) substrates

The PI surface molecules may also favour the NTBP molecule transfer at the interface of amorphous/crystal phases to promote the crystal growth as the obtained activation energy (about 0.965 eV) there is lower than that on the glass substrate (about 1.27 eV). Figure 6.6 (d) shows a schematic projection view of the b–c plane of the NTBP crystal where one can see that the molecules are piled up in the film plane which is favourable for the in-plane charge transportation as the charge hopping between molecules is a dominant mechanism of conduction in organic semiconductors. While, in the polyimide film X-ray diffraction analysis which was done by Kenji Okuyama’s group [10], the polyimide molecules tend to form a structure with unit cell dimensions a* = 0.79 nm, b* = 0.63 nm, c* = 2.5 nm (molecule axis) and β = 90°. If the surface molecules of polyimide are in the b*–c* (or a*–c*) plane and NTBP/polyimide satisfies relations a parallels to c* and b parallels to b* on the interface, the two types of lattices are well matched (i.e. 2|a| ≈ |c*| and |b| ≈ |b*|).

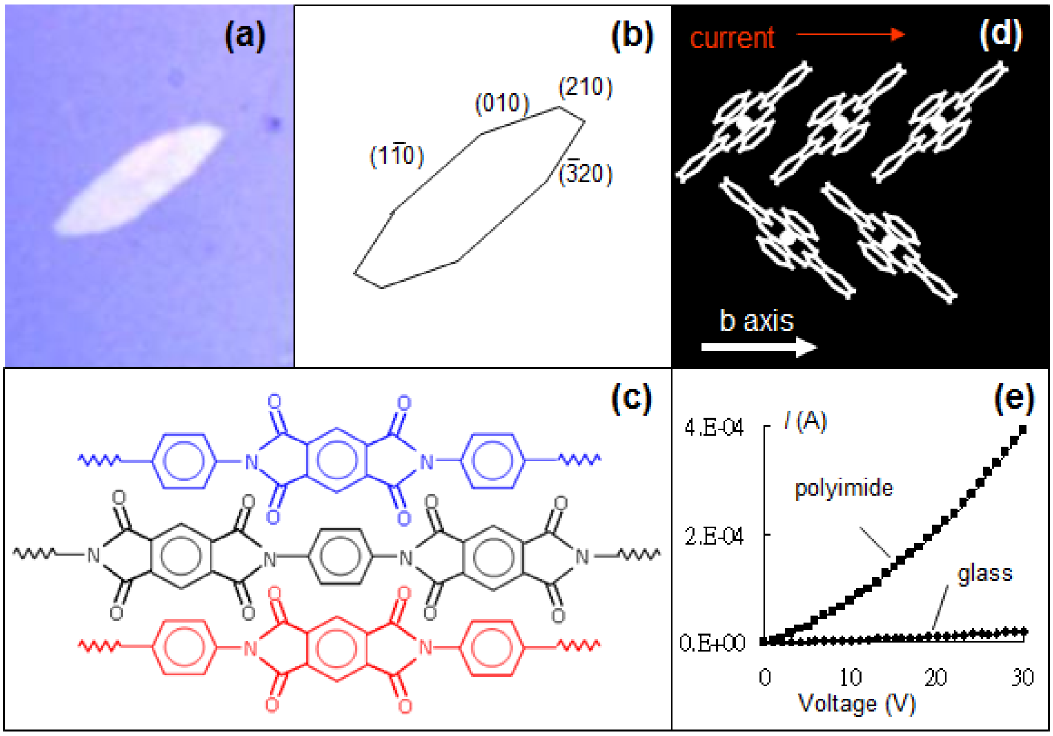

Figure 6.6. (a) A primary crystal of NTBP on polyimide. (b) Its schematic drawing by referring its XRD result. (c) A schematic drawing of molecule ordering on polyamide surface which induces a preferential orientation of NTBP crystal. (d) Schematic illustration of molecule packing when a film is crystallized with (001) lies in the plane of PI substrate. (e) I–V curves of crystalline NTBP films on the glass and PI substrates, respectively.

The result of an electro-transport measurement carried out by an Agilent 4156C Semiconductor Parameter Analyzer in a dry nitrogen ambient on the samples for both glass and PI substrates have been shown in Figure 6.5 (e). The Au (50 nm)/ Ti (2nm) contact electrodes were thermally evaporated through a shadow mask onto the crystalline film. The gap between the electrodes was 20 μm and the width of electrodes was 1 mm, respectively. The conductivity of the film on the PI substrate is σ^P=39 Ω/m which is one order of magnitude higher than that of the film on the glass substrate, σ^G= 2.2 Ω/m. The film thickness “t” was measured using a Dektak profilometer and the film conductance was calculated by formula below:

$$\sigma = L/WRt \qquad (7)$$

where the width of electrode W = 1 mm, the distance between two electrodes L = 20 μm, and the film thickness t is about 50 nm. The resistance R was taken from the measured I–V curves. Although the contact resistance may play a certain role in the measured conductivities it is not a dominant effect because: (i) the electrode deposition was carried out under identical conditions (same batch of deposition) for the two types of samples, and (ii) the work function of Au electrode (5.1 eV) and the highest occupied molecule orbital (HOMO) level of tetrabenzoporphyrin (5.2 eV) [11] are well aligned to ensure an optimized hole injection, as indicated by the good linear behaviour of the I-V curves at low voltages.

6.4 Organic polymer materials spectrum absorption

In this part, the crystallization of conjugated polymer for both PQT-12 and N2200 annealing under fixed temperature with different times have been investigated. In order to get information about film structure, atomic force microscopy (AFM) and spectrum absorption instruments were employed in this experiment.

The PQT-12 films were formed by spin-coating from 1'2-dichlorobenzene (DBC) solution (0.6mg/ml) onto well-cleaned quartz substrates that were subsequently baked in the glove box at 80 °C for 30 min. These were then annealed at 140 °C for 10 min, 20 mins, and 30 mins. Figure 6.6 demonstrates the atomic force microscopy scan on sample surfaces.

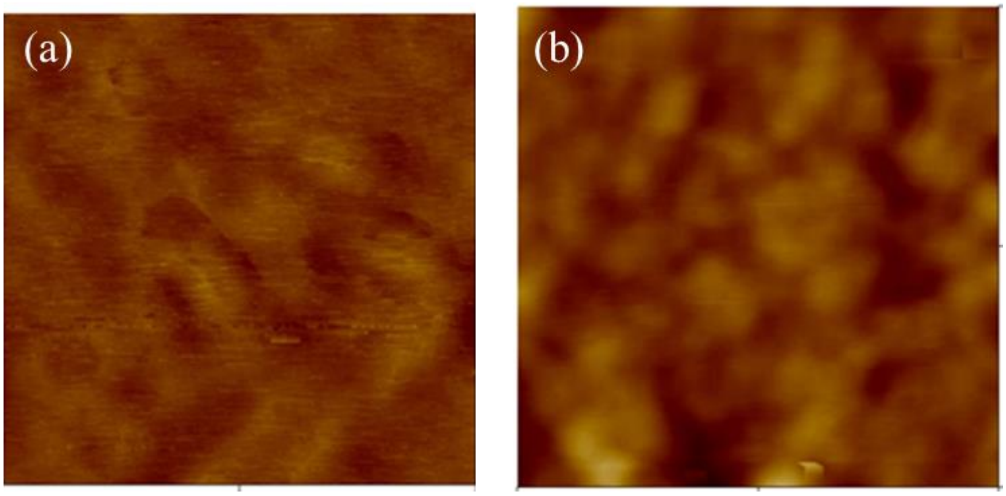

Figure 6.6. The high-resolution AFM images of PQT-12 thin film
(a) Dry at 80 °C for 30 min (b) annealing in glove box at 140 °C for 20min

From these two images, we can understand that the PQT-12 material surface is obviously different by annealing. This is because the 1'2-dichlorobenzene's boiling point is about 180 °C, the rest of the solvent in the material film was slowly evaporated during the annealing process. This is conducive to molecule reorganization, thereby forming a well-ordered packing structure. The spectrum absorption measurement reveals that absorption peak shift was minimal in the post-annealing treatment from 10 mins to 30 mins. That means molecular crystallization was finished in the first 10 mins. The PQT-12 spectrum absorption curves have been displayed in Figure 6.7.

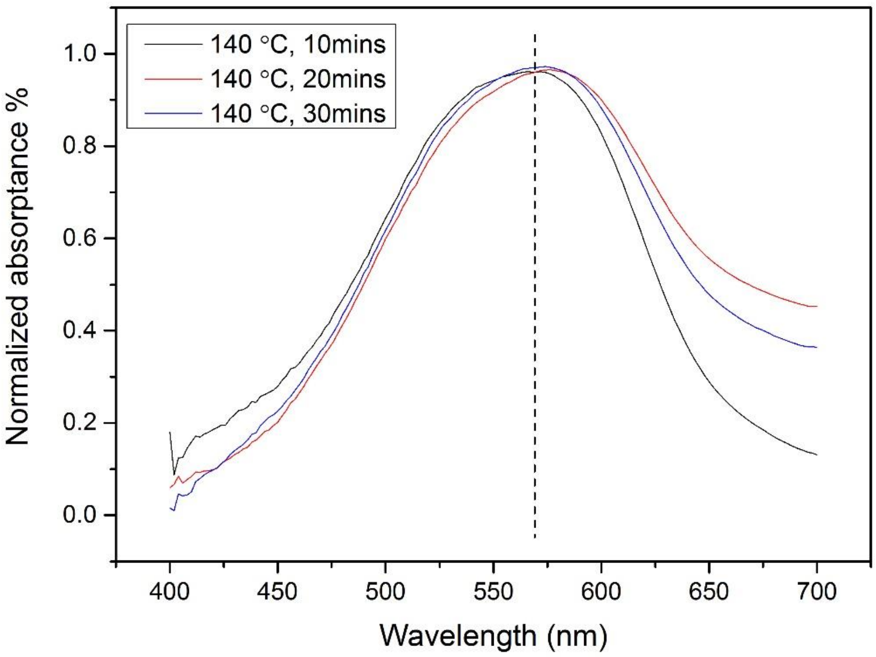

Figure 6.7. The normalized spectrum absorption of the spin-coated PQT-12 film under a fixed temperature with different annealing times.

In order to compare the annealing temperature influences on PQT-12 film, we decreased the annealing temperature to 130°C and 120°C. The spectrum absorption results have been displayed in Figure 6.8. We notice that the absorption peak was shifted dramatically, and when the temperature was 120°C, the film was not formed as an ordered crystalline film. As the temperature increased, the molecule began to reorganize and form a crystalline structure. From this experiment, we confirmed that the temperature is a significant parameter which can affect the molecular crystallization.

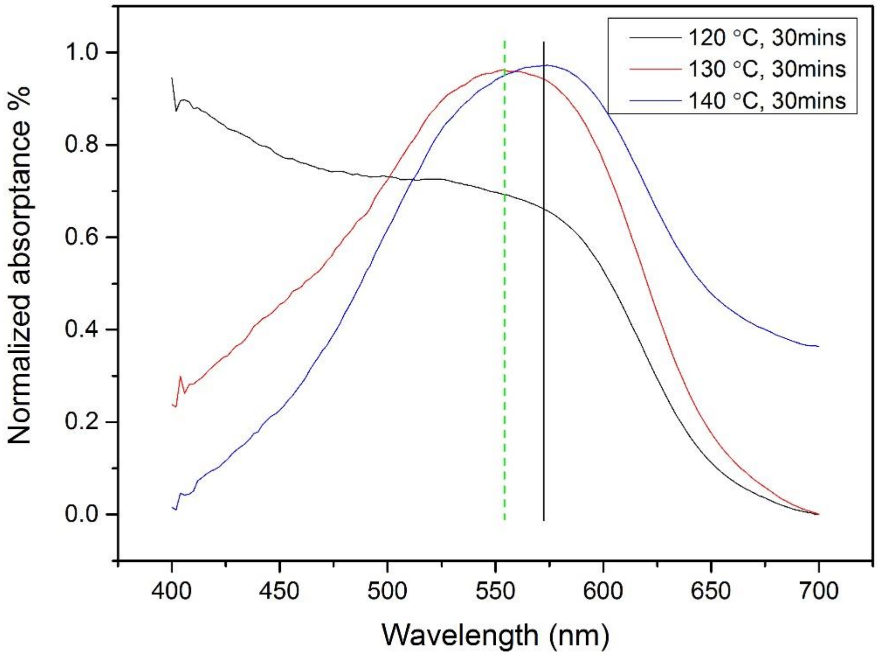

Figure 6.8. The normalized absorption spectrum of PQT-12 film annealed under a fixed time with different temperatures.

Similar analysis methods were also used with an n-type material. The N2200 film was deposited by spin-coating from Toluene solution, the concentration is the same as for the PQT-12 solution. Under an identical procedure, we have obtained the AFM image of N2200 thin film both dried at 80°C in a glove box for 30 min and annealing at 110°C for 4 hours. Figure 6.9 have illustrated these images.

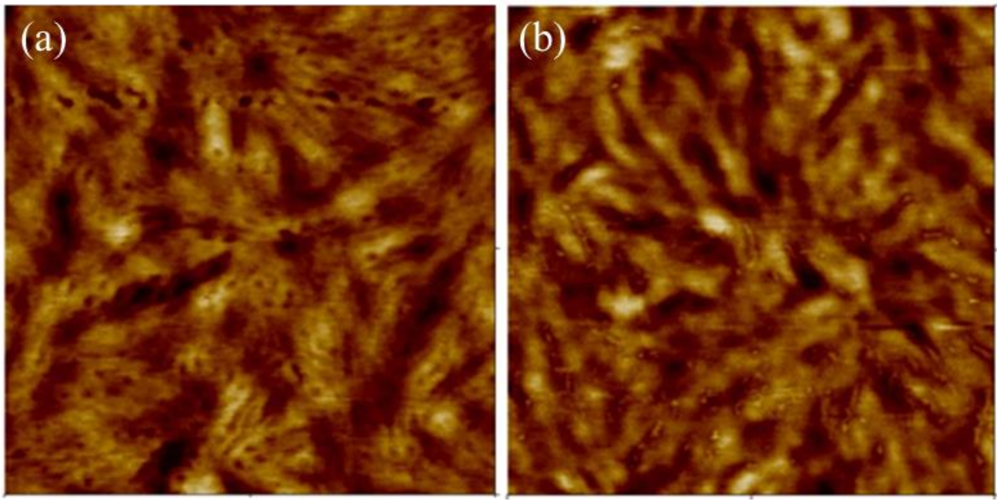

Figure 6.9. The high-resolution of N2200 AFM images
(a) Dry at 80 °C for 30 min (b) annealing in glove box at 110 °C for 4h

The image in Figure 6.9 (a) demonstrates that the film was already crystallized after drying at 80 °C for 30 minutes in a glove box. By comparison of these two images, we found that the film surface textures are quite similar. In order to investigate and understand the molecules crystallization degree in each hour, we prepared four N2200 thin film samples and post-annealed them at 110°C for 1 hour, 2 hours, 3 hours and 4 hours. The spectrum absorption measurement result has been displayed in Figure 6.10 below.

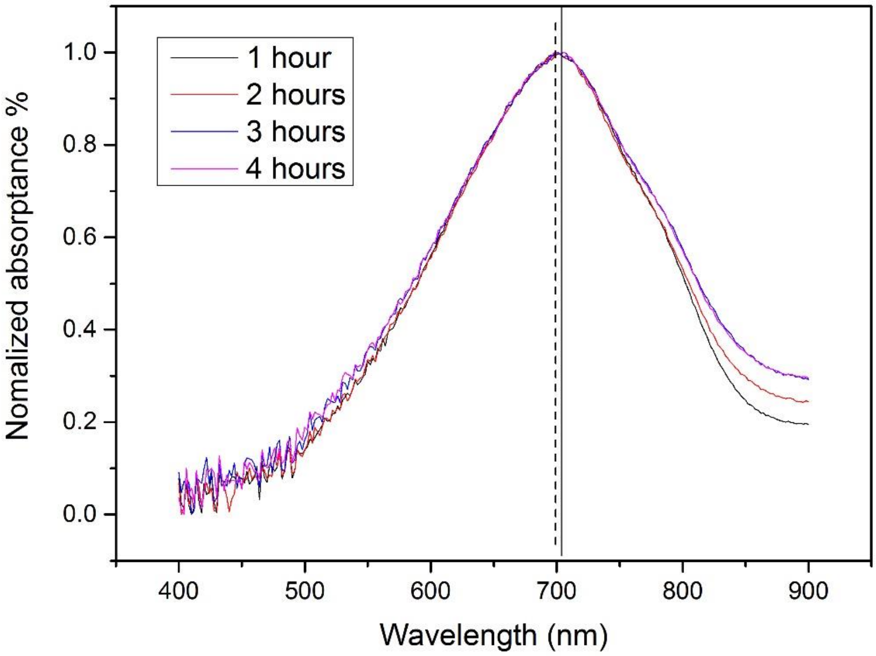

Figure 6.10. The normalized absorption spectrum of N2200 film annealed at a fixed temperature for different times.

The absorption peak is stable almost at 700 nm for these four samples which confirms that during an hour of annealing the film has been crystallized. That is because the Toluene' boiling point is 111°C, the solvent has been totally evaporated during the first period of annealing time. The following annealing may only reduce the grain boundary mismatch and crystal defects.

6.5 Summary

In this chapter, a comparison of tetrabenzoporphyrin crystalline film growth on both bare glass and PI substrates has been investigated. The result was that the material crystallization from its precursor shows obvious preferential crystal orientation on the PI substrate. In addition, the electrical conductivity also dramatically increased compared to crystallization on a bare glass substrate. This preferential orientation caused by the PI surface molecules provides a favourable nucleation template and required lower activation energy for NTBP crystal growth. This experiment has proved that the material substrate can affect the organic semiconductor crystallization. The annealing temperature influences on both n-type and p-type conjugated polymer semiconductor crystallization have also been evaluated. Through linear spectrum absorption measurement, it can be confirmed that the degree of PQT-12 crystallization was dramatically affected by temperature. Compared to PQT-12, the N2200 film crystallization was formed after drying. Future annealing only reduces the defects of the film.

Reference

1 Gorodetsky, A. A., Cox, M., Tremblay, N. J., Kymissis, I. & Nuckolls, C. Solar cells from a solution processable pentacene with improved air stability. *Chemistry of Materials* **21**, 4090-4092, (2009).

2 Umeda, T., Kumaki, D. & Tokito, S. High air stability of threshold voltage on gate bias stress in pentacene TFTs with a hydroxyl-free and amorphous fluoropolymer as gate insulators. *Organic Electronics* **9**, 545-549, (2008).

3 Carvalho, C. M. B., Brocksom, T. J. & de Oliveira, K. T. Tetrabenzoporphyrins: synthetic developments and applications. *Chemical Society Reviews* **42**, 3302-3317, (2013).

4 Craciun, M. F. *et al.* Electronic Transport through Electron-Doped Metal Phthalocyanine Materials. *Advanced Materials* **18**, 320-324, (2006).

5 Klauk, H. *et al.* Flexible organic complementary circuits. *IEEE Transactions on electron devices* **52**, 618-622, (2005).

6 Shea, P. B. *et al.* Solution-processed nickel tetrabenzoporphyrin thin-film transistors. *Journal of applied physics* **100**, 034502, (2006).

7 Ito, S., Ochi, N. & Murashima, T. A new synthesis of benzoporphyrins using 4, 7-dihydro-4, 7-ethano-2h-isoindole as an isoindole equivalent. *Heterocycles* **52**, 399-411, (2000).

8 Wolf, P., Gallet, F., Balibar, S., Rolley, E. & Nozieres, P. Crystal growth and crystal curvature near roughening transitions in hcp 4He. *Journal de Physique* **46**, 1987-2007, (1985).

9 Jou, J.-H. & Huang, P.-T. X-ray diffraction study of polyimide blends compatibility. *Polymer journal* **22**, 909-918, (1990).

10 Okuyama, K., Sakaitani, H. & Arikawa, H. X-ray structure analysis of a thermoplastic polyimide. *Macromolecules* **25**, 7261-7267, (1992).

11 Shea, P. B., Kanicki, J. & Ono, N. Field-effect mobility of polycrystalline tetrabenzoporphyrin thin-film transistors. *Journal of applied physics* **98**, 014503, (2005).

Chapter 7

Conclusion and future work

7.1 Introduction

So far, all the experiments have been presented in previous chapters. Developing a novel fabrication technique to achieve organic polymer semiconductor self-assembly under a confined structure is the highlight and the most important achievement in my study. In this chapter, I will review and summarize all of the experiments undertaken and provide overall conclusions from my studies. In addition, I can be noted that organic semiconductor materials are not limited to application in transistors; they also can be applied in multiple fields of electronics, such as biosensors. In my future work I hope to go on to explore these potentials.

7.2 Conclusion

Scientists general consider that the “coffee stain” effect should be avoided in fabrication processes, especially in inkjet printing and device fabrication. But now, I have developed it as a patterning method, demonstrating that it is possible to use it in organic electronic device fabrication. In a series of experiments, various solution-processable organic materials, both p-type and n-type, have been successfully patterned to a wire array geometry. Furthermore, the wire dimension can be manipulated to sizes in the range of a few micro- to a few nano-meters by only adjusting the solution concentration if the proper size of template is chosen. The minimum size of wire that we have patterned was a 250 nm polystyrene line (see the Figure 4.25). We have shown that “groove pinning” is the central mechanism for fine line patterning and it was also revealed that the capillary flow-induced edge deposition in the liquid bridge dominates the solute transportation and deposition to the contact line. In the grid structure formation, we have found that on the secondary patterning process, if one of the sidewalls did not firmly pin on the substrate, the solute in the groove was dragged toward to the neighbouring sidewall and finally deposited there. In this way, the fine wire array cannot be obtained. In addition, an interesting phenomenon that there are several nano-sized sub-stripes (about 50 nm in size) inside a single wire has been observed in the “space-applied” patterning result. We have determined that the reason for this is that during the secondary patterning process, a tiny amount of solution was trapped between the sidewall and primary line and the pinning-depinning event continued occurring until the solvent totally evaporated.

To observe how the solution moves in the groove, a series of wire array patterning experiments under the different temperatures have been carried out. Depending on the colour of the solution, both transmissive and reflective modes have been used for the in-situ microscopic observation. Through data recording and calculation, we have confirmed that the solution drying process under the groove was controlled by the energy that a solvent molecule required to escape from the liquid surface rather than by diffusion. Compared to the traditional device manufacture method, the PDMS template patterning technique can make solution-processable organic semiconductor via self-assembly under a confined structure to form a high-resolution wire array. In this way, we can fabricate tens of OFETs at one time on a substrate, avoiding the photolithography procedure to produce the transistor channel. This further reduces the cost of device fabrication. For insoluble materials, such as PEDOT:PSS, a patterning transfer combined with plasma etching method has been employed for the wire array fabrication. The size of PEDOT:PSS wire was determined by the primary wire dimension that patterned on the PEDOT:PSS thin film. Finally, for polymer electronic devices, both organic field effect transistors (OFET) and organic electro-chemical transistor (OECT) have been fabricated. Through measurement, all of the devices have been shown to be working very well. The n-type transistor on/off ratio was about 10^4 with the electron mobility of about $1.75 \times 10^{-2} \mathrm{cm}^2/\mathrm{Vs}$. The PQT-12 based transistor on /off ratio was about 10^3 and the hole mobility was to be found about $1.75 \times 10^{-3} \mathrm{cm}^2/\mathrm{Vs}$. Furthermore, for the F8T2-base transistor, the on/off ratio reached at about 10^5 , which was a very good result compared to others. However, the point of its current output was shifted from 0 volts to about -7.5 volts and the hole mobility was only about $6.9 \times 10^{-4} \mathrm{cm}^2/\mathrm{Vs}$, this was thought to be because the organic material crystallization growth on different substrates has different orientations, resulting in difficulty with the charge carrier injection. Therefore, experiments were undertaken to investigate the crystallization mechanism of the organic material on different substrates. The results of the crystallization experiments revealed that the characteristics of the substrate surface have a huge impact on a small molecule's preferential orientation on crystallization since the activation energy requirement on each substrate was different. Besides, the obtained preferential orientation dramatically increases the electrical conductivity of the film in comparison with that on a glass substrate, which does not show any preferential orientation. The preferential orientation of NTBP on the PI substrate is believed to be caused by a local order of the PI surface-molecules, which can provide a favourable nucleation template for the growth of NTBP crystals.

The influence of temperature on the crystallization of organic conjugated polymer semiconductors has been studied as well. From the results we conclude that post annealing the material under different temperatures leads to different performance properties. If the temperature cannot reach the material crystallization point, then even post baking for more time, the result of crystallization will not be ideal. In addition, the choice of solvent is another point to be considered. It was found that high boiling point solvents, which evaporate relatively slowly, are favourable for forming ordered structures and obtaining high performance devices.

7.3 Future work

The transistor is a fundamental component in electronics and has a very wide range of applications. One of the important applications is in logic circuits. Depending on the various combinations, transistors can be used to make up three devices, they are: an inverter, a negative-and gate and a nor gate. All of these gate circuits can then be used to build up more complicated logic circuits. Taking an inverter as an example, it has two types: One is made up from two n-type transistors, and the other is called (Complementary Metal–Oxide–Semiconductor) COMS, which is made from one n-type and one p-type transistor. The manufacturing technology of silicon-based complementary circuits is very mature, but for circuits which are built from organic transistors it is just the beginning. Therefore, one of the aims of future work is to develop the current technique to patterning both n- and p-type organic semiconductor to fabricate gate circuits. If we can find a method to realize material phase separation according to the solvent's hydrophilic and hydrophobic characteristics, maybe this idea can be achieved. Another future target is continuing my work in Chapter 5. As I mentioned before, the PEDOT:PSS based electro-chemical transistor has low drive voltage and high sensitivity characteristics; therefore it maybe use it to design a biotranducer to detect bio-signal transmission. The cell can be cultured in those holes where I have fabricated by the optical lithography technique on the PEDOT:PSS wires. The biological agent can then tune the condition of the ion channel and a corresponding signal variation can be detected. This could have potential application in the cancer cell research.